Spatiotemporal dynamics of stress factors in wheat analysed by multisensoral remote sensing and geo-statistics

Dissertation

zur Erlangung des Doktorgrades

der Mathematisch-Naturwissenschaftlichen Fakultät

der Rheinischen Friedrich-Wilhelms-Universität Bonn

vorgelegt von

Dipl. Geogr. Jonas Franke

aus Saarbrücken

Bonn, August 2007

1. Gutachter: Prof. Dr. Gunter Menz
2. Gutachter: Prof. Dr. Sebastian Schmidtlein
3. Gutachter: Prof. Dr. Walter Kühbauch
4. Gutachter: PD Dr. E.-C. Oerke

Tag der mündlichen Prüfung:
26.09.2007

Diese Dissertation ist auf dem Hochschulschriftenserver der ULB Bonn
http://hss.ulb.uni-bonn.de/diss_online elektronisch publiziert
Erscheinungsjahr: 2007

Contents

Chapter 3

Geo-statistical analysis of the spatiotemporal dynamics of powdery mildew and leaf rust in wheat

Chapter 4

Multi- and hyperspectral imaging of leaf rust infected wheat plants

Chapter 5

Multitemporal wheat disease detection by multispectral remote sensing

Chapter 6

Identification of site-specific crop growth anomalies using simulated endmembers for spectral mixture analyses

Chapter 7

The potential of airborne hyperspectral and multispectral remote sensing data for the identification of powdery mildew in wheat

Conclusion

Appendix

List of Figures

List of Tables

List of Acronyms

BBCH	Biologische Bundesanstalt, Bundessortenamt und Chemische Industrie. BBCH is a decimal code for the growth stages of cereals
CoB	Count-Based endmember selection
CoBI	Count-Based Index
CWSI	Crop Water Stress Index
EAR	Endmember Average RMSE
ECa	apparent Electrical Conductivity
FWHM	Full Width at Half Maximum
GCP	Ground Control Points
GIS	Geographic Information System
GPS	Global Positioning System
HyMap	Hyperspectral Mapper
LAI	Leaf Area Index
MASA	Minimum Average Spectral Angle
MESMA	Multiple Endmember Spectral Mixture Analysis
MF	Matched Fraction
MNF	Minimum Noise Fraction
MTMF	Mixture Tuned Matched Filtering
NDVI	Normalized Difference Vegetation Index
NIR	Near-Infrared
PCA	Principle Component Analysis
PPI	Pixel Purity Index
PRI	Photochemical Reflectance Index
RMSE	Root Mean Square Error
RSR	Relative Spectral Response
SADIE	Spatial Analysis by Distance IndicEs
SMA	Spectral Mixture Analysis
SWIR	Short Wavelength Infrared
TIR	Thermal Infrared
VIS	Visible spectrum
WDI	Water Deficit Index

Acknowledgments

This thesis originated at the Center for Remote Sensing of Land Surfaces (ZFL) and at the Department of Geography, more precisely in the Remote Sensing Research Group (RSRG) of the Rheinischen Friedrich-Wilhelms-University of Bonn. All studies were carried out under sponsorship of the Research Training Group 722 ‘Information Techniques for Precision Crop Protection’, which is funded by the German Research Foundation (DFG).

I would like to thank and recognize those that have helped me through this academic journey. Special thanks go to my doctoral thesis supervisor Professor Dr. Gunter Menz, his guidance and encouragement in respect of scientific support and my professional development was instrumental to the success of this research.
Professor Dr. Walter Kühbauch I would like to thank for providing me the perception of an agronomist. I am glad and appreciate that Prof. Dr. Sebastian Schmidtlein joins the dissertation committee. I thank PD Dr. Erich-Christian Oerke for providing support in planning field and laboratory experiments and in any concerns of phytopathological questions as well as for an excellent management of the DFG- Research Training Group 722.

The success of this thesis is also closely associated with great teamwork within the working groups of the ZFL and RSRG. Special thanks therefore go in equal measure to all members of both working groups, for the excellent cooperation, spontaneous support in the solution of problems and the superior working atmosphere. Particularly with regard to the coordination of the Center for Remote Sensing of Land Surfaces (ZFL), I thank Dr. Matthias Braun and Ellen Götz for their dedication.

Thanks are also due to following people that have substantially contributed to this thesis: Dr. Uwe Rascher from the Institute of Chemistry and Dynamics of the Geosphere of the Phytosphere Research Center Jülich for cooperation and providing a sophisticated hyperspectral imaging sensor; Steffen Gebhardt for checking through the manuscript and many invaluable discussions concerning geo-data handling and processing as well as the attitude to work; the manager of the experimental farm of the University of Bonn ‘Klein-Altendorf’ Markus Huober for the realization of the field

experiments; Professor Dr. Hans-Peter Helfrich at the Mathematical Seminar of the University of Bonn for his support in statistical concerns; Torsten Welle for many fruitful discussions about remote sensing and the way of life; Dr. Jan Jacobi for the assistance regarding many ‘Precision Agriculture’- questions; Dr. Dar Roberts at the Geography Department of the University of California, Santa Barbara (UCSB) that he offered me to spend an awesome and very productive time in his working group; Kerry Halligan from the UCSB for a great deal of discussions regarding hyperspectral data processing; Simone Gigli, Daniel Morris and Colleen Hall for checking through the manuscript and last but not least my colleagues and friends in the DFG-Research Training Group 722.

Even in 1995, when we just graduated from school, my friend Christian Hammers put during a surf trip the idea in my head to pursue a PhD in Geography, thank you for that inspiration.

Abstract

Plant stresses, in particular fungal diseases, basically show a high variability in space and time with respect to their impact on the host. Recent ‘Precision Agriculture’ techniques allow for a spatially and temporally adjusted pest control that might reduce the amount of cost-intensive and ecologically harmful agrochemicals. Conventional stress detection techniques such as random monitoring do not meet demands of such optimally placed management actions. The prerequisite is a profound knowledge about the controlled phenomena as well as their accurate sensor-based detection. Therefore, the present study focused on spatiotemporal dynamics of stress factors in wheat, Europe’s main crop. Primarily, the spatiotemporal characteristics of the fungal diseases, powdery mildew (*Blumeria graminis*) and leaf rust (*Puccinia recondita*), were analysed by remote sensing techniques and geo-statistics on leaf and field scale.

Basically, there are two different approaches to sensor-based detection of crop stresses: near-range sensors and airborne-/satellite-borne sensors. In order to assess the potential of both approaches, various experiments in field and laboratory were carried out with the use of multiple sensors operated at different scales. Besides the spatial dimension of crop stresses, all studies focussed on the temporal dimension of these phenomena, since this is the key question for an operational use of these techniques. In addition, a comparison between multispectral and hyperspectral data gave an indication of their suitability for this purpose.

The results exhibit very high spatiotemporal dynamics for both fungal diseases. However, powdery mildew and leaf rust showed different characteristics, with leaf rust showing a more systematic temporal progress. The physiological behaviours of the phenomena, which are strongly influenced by various environmental factors, define the optimal disease detection date as well as the temporal resolution required for sensor-based disease detection. Due to the high spatiotemporal dynamics of the investigated diseases, a general recommendation of optimal detection periods can not be given, but critical periods are highlighted for each pathogen.

The results indicate that multispectral remote sensing data with high spatial resolution shows a high potential for quantifying crop vigour by using spectral mixture analyses. Simulated endmembers for the identification of stressed wheat areas were utilized, whereby promising results could be achieved. However, due to the low spectral resolution of these data, a discrimination of stress factors or early disease detection is not possible. Hyperspectral data was therefore used to point out the potential of early detection of crop diseases, which is a crucial and restrictive factor for Precision Agriculture applications. In a laboratory experiment, leaf rust infections could be detected by hyperspectral data five days after inoculation. In a field experiment with respect to early stress detection, it could be demonstrated that hyperspectral data outperformed multispectral data. High accuracy for the detection of powdery mildew infections in the field was thereby achieved.

Due to the fact that typical spatiotemporal characteristics for each pathogen were found, there is a high potential for decision support systems, considering all variables that affect the disease progress. Besides the further analysis of hyperspectral data for disease detection, the development of a decision support system is the subject of the upcoming last period of the Research Training Group 722.

Chapter 1

Introduction

1.1 Precision Agriculture

Crop production undergoes a change since the early 1980's, when technological progress entered the agricultural management. The implementation of new technologies such as terrestrial, airborne and spaceborne sensor systems, Geographic Information Systems (GIS), and the Global Positioning System (GPS) allow a more precise cultivation of agriculturally-used area (*Kühbauch & Hawlitschka 2003, McBratney et al. 2005, Pinter Jr. et al. 2003*). Recent trends in agriculture thus show a fundamental transition to a more sustainable management (*Bongiovanni & Lowenberg-Deboer 2004*). Due to political demands on sustainable crop production, these trends were enforced by various directives. Apart from 'Agenda 2010' (*United Nations Conference on Environment and Development* (UNCED), in 1992) which stipulates sustainable farming, the 'White Book on Food Safety', published by the European Commission in 1999, aims for a regulation of maximum limits for residues of pesticides and contaminants on food. Pesticides, in particular, have a harmful impact on the environment as they not only harm living target organisms, but often contaminate soil, water and food resources. '*One group of chemicals that requires particular attention is pesticides. (...) They can affect human health via their contamination of groundwater, soil, food and even the air. Gaps in the current data on the issue make it difficult to be precise about the scale and trends of the problem but there is sufficient evidence to suggest it is serious and growing.'* (*European Commission 2002*).

In order to fulfil the requirements of a sustainable agriculture, a modernization of crop production is essential. A basic prerequisite is thereby the substitution of the traditional uniform land management for a site-specific management, i.e. Precision Agriculture, also referred to as 'Precision Farming'.

Even though existing definitions of Precision Agriculture are inconsistent (*McBratney et al. 2005*), they generally describe that management actions are adjusted to within-field heterogeneities of parameters that are relevant for crop growth, such as topography, climate, soil, availability of nutrients and water, stressors or man-made impacts. Precision Agriculture uses technologies that provide detailed, spatial information in a high resolution about fields and crop conditions and constitute an information-based approach of crop production. By using modern technologies, cultivation can be adjusted to field varieties, and agrochemicals can be applied in a site-specific way, targeted to where they are needed. This can result in a more sustainable management of agriculture due to an increase of yield and a reduction of cost-intensive agrochemicals while reducing the impact on the environment (*Bongiovanni & Lowenberg-Deboer 2004*).

1.2 Impact of stress factors on crops

Stress factors on crops are multifarious. Unfavourable soil conditions, water availability, nutrient deficiency, weeds and pests are the main factors causing crop stress (*Pinter Jr. et al. 2003*). These biotic and abiotic stressors cause changes in plant physiology and thus affect crop growth. As a result, depending on the types and impacts of stresses, the productivity of crop areas may be strongly reduced (*Machado et al. 2002, Thomas et al. 1989*). Soil conditions are comparatively stable (slow-variable), whereas pests are highly dynamic in spatial and temporal dimension (fast-variable). In addition, various types of pests have diverse spatiotemporal characteristics and thus a high variability of impacts on the host. Pests comprise fungi, virus, bacteria, insects and nematodes. The fact that pests show very heterogenic characteristics in space and time requires a detailed understanding of stress factors, which are the main challenges for effective stress management.

Fungal pathogens are the most frequently controlled pests in Germany and the European Union (*European Commission 2002*). This is mainly due to the fact that pathogens are rather common in cereals which constitute the main cultivated plants in the European Union (36.401.000 hectares out of 130.443.000 hectares utilized agricultural area in 2000 (*European Commission 2002*)), resulting in a large amount of fungicides being applied.

Blumeria graminis – causing powdery mildew – and *Puccinia recondita* – causing leaf rust – are among the most common fungal pathogens producing characteristic symptoms on cereal leaves in Central Europe. Both diseases have polycyclic characteristics, i.e. pathogens repeatedly infect plants during the growing season (*Mount & Slesinski 1971, Braun 1987, Cummins & Hiratsuka 2003*). These fungal pathogens can cause defoliation of plants or even the death of the entire host plant, resulting in considerable yield losses in quantity and quality (*Moshou et al. 2006, Moschini & Pérez 1999, Hunger & Jackson 2004, Glawe & Grove 2006*). Table 1.1 shows the approximate yield loss caused by leaf rust in relation to severity of rust on the flag leaf at various growth stages. In particular leaf rust infections at early growth stages have the highest impact on the yield.

Table 1.1: APPROXIMATE YIELD LOSS (%) in relation to severity of rust on the flag leaf at various growth stages

Leaf Rust Severity on Flag Leaf	*10%*	*25%*	*40%*	*65%*	*100%*
Growth Stage			Loss (%)		
Flowering	10	15	20	30	35
Milk	2	5	8	14	20
Soft Dough	1	3	4	7	10
Hard Dough	1	1	1	3	5

Adapted from: *Hunger & Jackson (2004)*

Even though, airborne pathogens causing powdery mildew and leaf rust are both obligate biotrophs that require a living plant tissue for growth and reproduction, they have different characteristics and life cycles as shown in figures 1.1 and 1.2 (*Braun 1987, Wright et al. 2000*).

Blumeria graminis belongs to the Ascomycetes in the order Erysiphales that initially affect the plants leaf surface by producing mycelia (vegetative structure) and conidia (asexual spores). Their white and dusty appearance is responsible for the name of the disease powdery mildew (figure 1.1). Under optimal environmental conditions, *Blumeria graminis* starts producing a primary germ tube about 0.5 to 3 hours after inoculation of the host and appressorial germ tubes (microscopic structures) about 12 to 16 hours after inoculation that enables the mycelia to stick to plant surfaces (*Mount*

& Slesinski 1971, Nielsen et al. 2000, Wright et al. 2000, Carver et al. 2001, Wright et al. 2002). Special outgrowth called 'haustoria' then penetrates the cells of the host (15 to 24 hours after inoculation) and absorbs nutrients that allow the conidia to develop (*Carver et al. 2001*). After 2-3 days, nutrients supplied by the growing primary haustorium become insufficient to support the young colony, and a second generation of appressoria is initiated (*Carver et al. 2001*). 4-5 days after inoculation, the first conidiophores develop and sporulation starts, when spores are transportable to other hosts (*Braun 1987, Carver et al. 2001*). Optimal environmental conditions for the development of powdery mildew are temperatures of 15°C to 20°C with a relative humidity >95% for the infection process (*Kluge et al. 1999*). The incubation period of this disease is about three to five days.

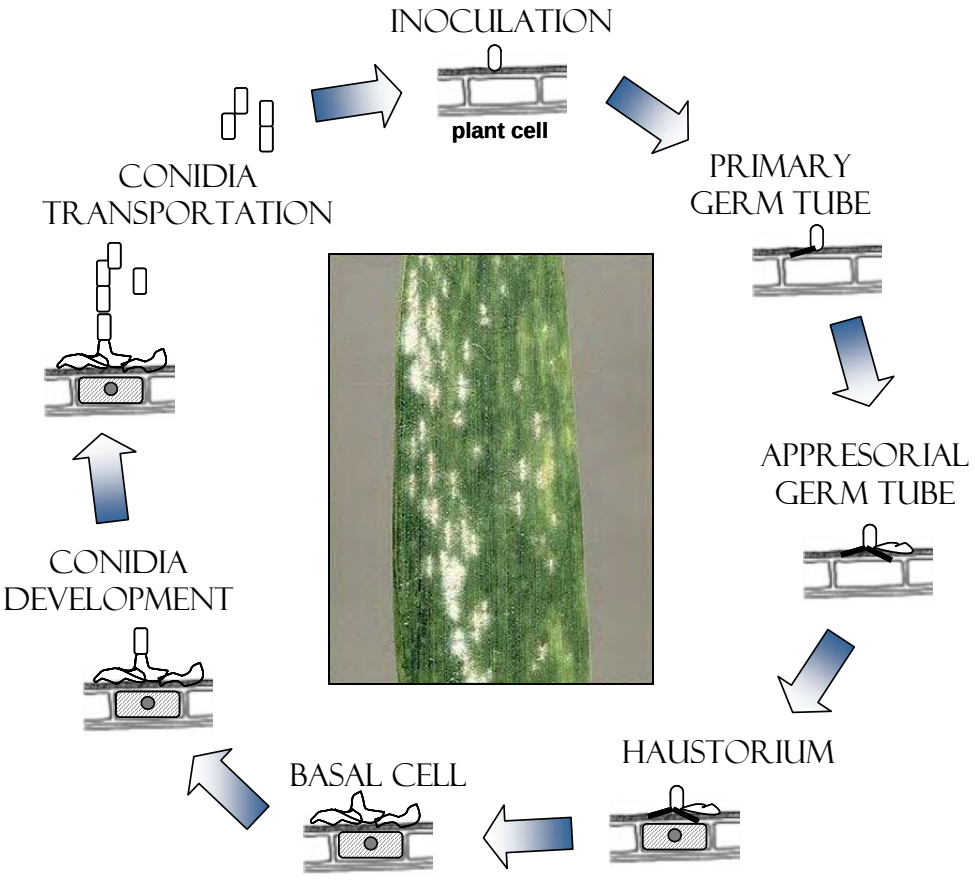

Figure 1.1: LIFE CYCLE OF *Blumeria graminis*

Figure based on: *Braun (1987), Carver et al. 2001* and *anonym author of Risø National Laboratory (2007)*

Due to its worldwide distribution, leaf rust is one of the most important diseases in cereals. Pathogens are able to move long distances and develop rapidly under optimal environmental conditions (*Marsalis & Goldberg 2006*). Symptoms are small round or oval, orange spots on the upper surface of infected leaves that have a rusty appearance. Pustules are highly productive with about 1000 new spores per day, each of which is capable of infecting a plant (*Lipps 2006, Watkins 2005*). Leaf rust has a more complex life cycle than powdery mildew (figure 1.2).

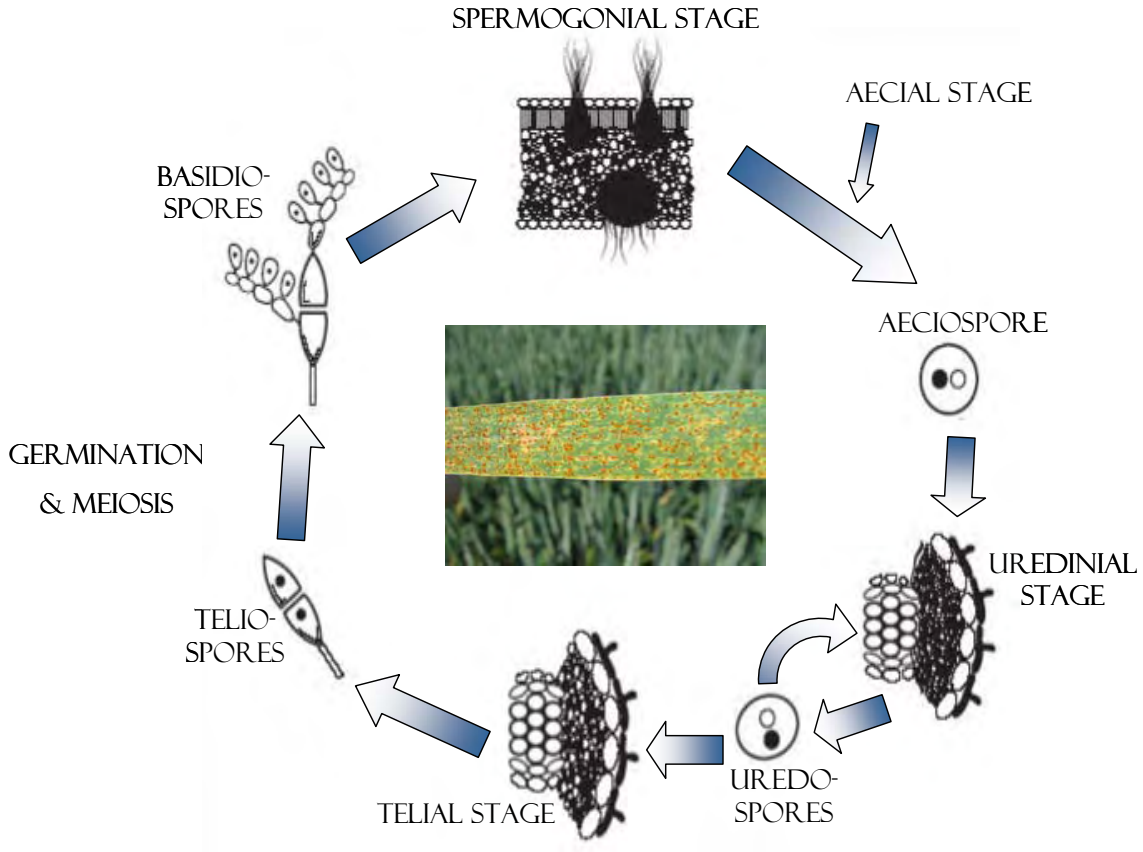

Figure 1.2: LIFE CYCLE OF *Puccinia recondita*

Figure based on: *Marsalis & Goldberg (2006)*, *Watkins (2005)*

Basic spore states of *Puccinia recondita* can be categorized in five spore-producing structures: spermogonium, aecium, uredinium, telium and basidium (*Cummins & Hiratsuka 2003*). Spermogonia are produced that results from infection by basidiospores. Spermogonia as well as aecia, which preceded or accompanied spermogonia, are produced on the same haploid thallus. Then unicellular aeciospores develop, which produce mycelium upon germination that produces either uredinia or telia, but not aecia again. Uredinia is the state that is repeated in the rust

life cycle. Urediniaspores produce mycelium when they germinate that gives rise to telia and teliospores. Teliospores are able to survive unfavourable environmental conditions such as extreme temperatures. Teliospores produce basidia and basidiospores upon germination, which allow for another initialisation of the life cycle (*Cummins & Hiratsuka 2003*). Under optimal environmental conditions, heavy rusting occurs that causes a loss of infected leaves that reduces the grain filling period and results in smaller kernel size (*Lipps 2006, Watkins 2005*). Dew, light rain, or high relative humidity of 100% for at least four hours and temperatures of 13°C to 23°C are ideal for rust development (*Maclean 1982, Kluge et al. 1999*).

An important fact for the prediction, diagnosis and control of powdery mildew and leaf rust is that they usually occur at different growth stages due to their different demands on environmental conditions: powdery mildew usually occurs earlier in the growing season than leaf rust. However, they can also exist at the same time, resulting in mixed infections.

Plant diseases are complex multi-factorial and multi-dimensional phenomena. Their spatial and temporal development is influenced by various biotic and abiotic factors (*Moschini & Pérez 1999*). The interaction between host, micro-organism and environment is a complex system which is influenced by factors like soil characteristics, topography, plant density, host resistance, host growth stage, inoculums level, cultural practice, air temperature, humidity etc. (*Mount & Slesinski 1971, Roelfs 1972, Nelson & Campbell 1993, Tubajika et al. 2004, Moschini & Pérez 1999*). Hence, detection, modelling or control of fungal infections in crops is a challenge that requires an understanding of each impact factor and their inter-relationships.

1.3 Remote sensing for stress detection

According to the characteristics of plant diseases, a site-specific crop management requires a high spatial and temporal information density with regard to the status of any crop growth-relevant parameter. Traditional field-sampling methods based on visual inspections are labour-, cost- and time-intensive and cannot meet requirements of Precision Agriculture at all. Innovative sensor techniques, GIS, and data processing methods can provide detailed information about field and crop

conditions with a high spatial resolution. Satellite-, airborne- or near-range remote sensing have the potential to identify field heterogeneities in a non-invasive way (*Blakeman et al. 2000, Bravo et al. 2004, Kühbauch & Hawlitschka 2003*). For the detection and mapping of stress factors in crops, sensor-based methods are of increasing importance, particularly for the detection of spatiotemporally dynamic stress phenomena like plant diseases. A prerequisite is therefore a profound knowledge about spectral characteristics of vegetated surfaces and remote sensing approaches for vegetation monitoring as well as basic remote sensing and digital image analysis techniques. In this thesis, no introduction to these topics is given, because many references give excellent overviews about remote sensing of vegetation and analysis techniques, e.g. *Jensen (2000), Löffler (1994)*.

In general, there are two different sensing-based approaches for a detection of crop stresses: far-range satellite-/airborne sensor systems and near-range sensors that acquire data in a scope of application close to the target. *West et al. (2003)* provided a detailed overview of the sensor-based detection of stress. First, each sensor system covers a different geographic scale, i.e. satellite imagery covers a larger area than near-target sensors. Second, each system has a different resolution scale, i.e. the smallest identifiable object in the images is limited by the spatial resolution/pixel size of the sensor system (*Cao and Lam 1997*). Near-range systems thus operate on the highest resolution scale and the lowest geographic scale, whereas satellite imagery shows reverse characteristics. Airborne sensor systems operate on intermediate scales (figure 1.3).

However, the suitability of each sensor system for the detection of plant stresses depends primarily on the operational scale of the monitored phenomenon (the scale in which the stress operates) and the temporal scale/resolution of the sensor. Hence, monitoring of complex biochemical systems such as plant diseases is limited by the geographic, resolution and temporal scale of a technical sensor system. For instance, *Voss (2005)* demonstrated the limitations of the resolution scale for a detection of crop stresses. Detailed analyses of the operational and temporal scale of plant diseases (spatiotemporal dynamics) and the potential of each sensor approach for the detection and monitoring of these phenomena are required respectively. Knowledge about the impact of diseases on plants obtained by sensor systems at

near-range scale can also be valuable for up-scaling processes, i.e. transferability to larger scale systems such as satellite remote sensing. An understanding of stress-dependent causes to the reflection behaviour of plant leaves or entire canopies monitored by near-range sensors helps to interpret remote sensing data with lower spatial resolution.

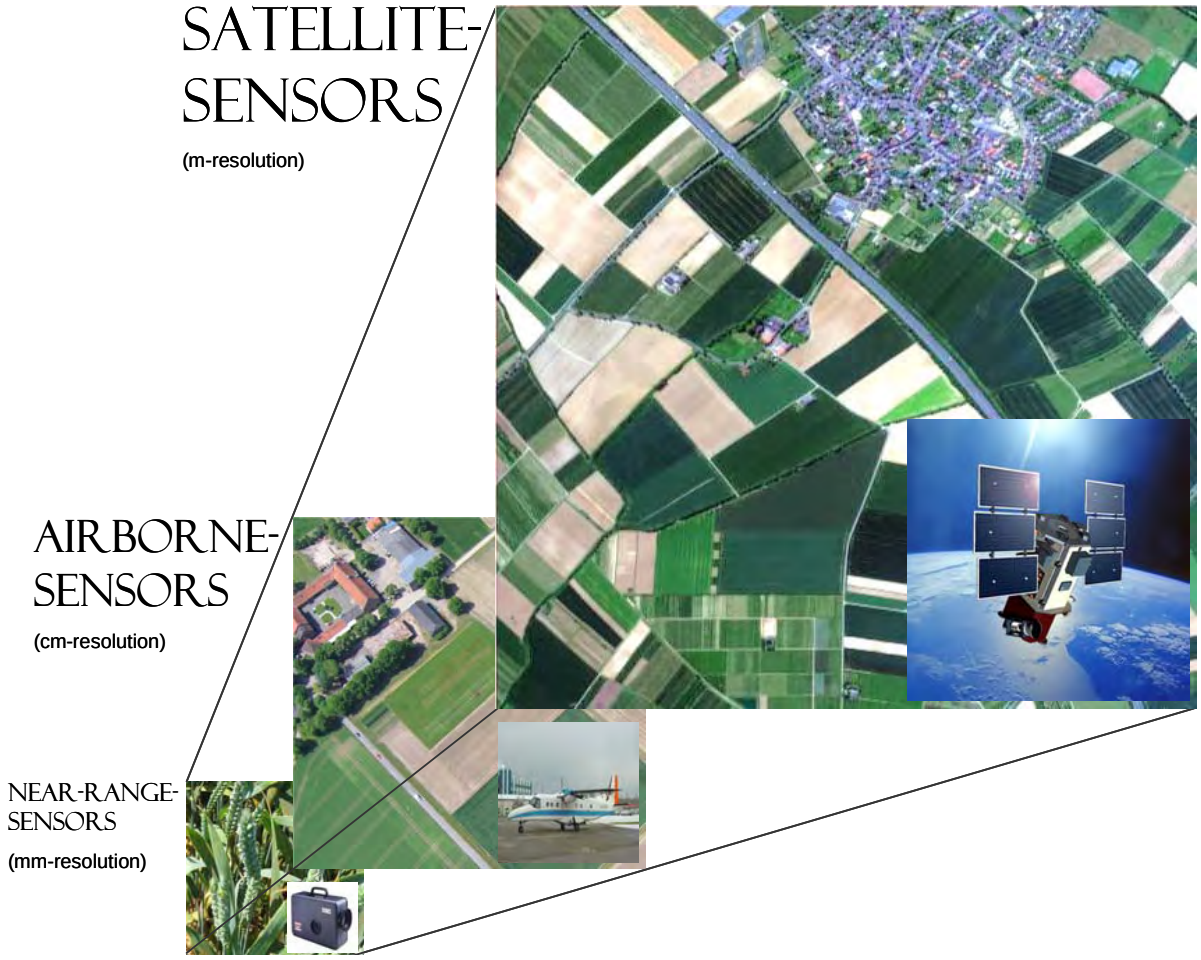

Figure 1.3: MULTISCALE SENSOR approach

Each of the above mentioned stress factors were already analysed by using various sensors, with some of the studies revealing the high potential for stress detection with remote sensing systems.

Dalal & Henry (1986), for example, derived different soil characteristics using the spectral reflectance of soil surfaces which was measured by a spectroradiometer in field. The spatial variability of soil and the caused impact of water stress on crops

was analysed by *Smith et al. (1989)*, who remotely sensed the thermal emission of stands. Furthermore, *Mathieu et al. (2003)* estimated the moisture and organic content of cultivated soils on the basis of radar remote sensing imagery. The influence of various soil types on spectral properties of cereals was estimated by *Verma et al. (2002)* with a multispectral vegetation index.

The impact of water stress was described by *Jackson et al. (1981)* by thermal sensor measurements. Water stress causes a reduced evapotranspiration and thus an increased temperature of plants (*Carter 1991*). A data fusion method was developed using vegetation indices and measurements of plant temperature (Crop Water Stress Index (CWSI)) to estimate evapotranspiration. In addition, *Moran et al. (1994)* presented the Water Deficit Index (WDI) that reduced the impact of soil temperature on the CWSI. Recent studies focused on the differentiation of water stress and nutrient deficiency (*Casa & Jones 2003, Estep et al. 2004*).

Nutrient deficiency and weed are the most frequently remotely sensed stress factors in crops. Most of the studies identify nutrient deficiency stressed plants by analysing reflectance changes in the visible spectrum caused by changed chlorophyll contents (*Blackmer et al. 1995, Fillela et al. 1995, Hansen & Schjoerring 2003*). The potential of the Photochemical Reflectance Index (PRI) for the detection of nutrient deficiency was analysed by *Gamon et al. (1997)*.

The impact of weeds on crop growth and spatial distribution was intensely assessed by remote sensing. In general, there are two approaches to control weed infestations by using sensor systems: first, weed mapping (satellite-borne or near-range sensors), which is carried out prior to herbicide applications (*Gebhardt et al. 2006, Gerhards and Oebel 2006*), and second, online-/real-time-approaches (near-range sensors). Several studies revealed the potential of remote sensing particularly for weeds that appear in patches at initial crop growth stages (*Benlloch & Rodas 1998*). Some online-/real-time-systems with mounted sensors already exist that detect weeds in front of a tractor, thus allowing for a precise herbicide application in the rear (*Ahrens 1994, Tian et al. 1999, Blasco et al. 1998*).

Even though airborne-imagery was first used as early as 1929 to detect diseases in crops (*Taubenhous et al.1929*), there are not many remote sensing studies that take this stress factor into account. Near-range sensors, on the other hand, are more widely applied. *Lorenzen & Jensen (1989)* differentiated between healthy and powdery mildew infected barley leaves by using a spectroradiometer. They observed an increased reflectance of infected leaves in the chlorophyll-absorbing region of the spectrum. *Larsolle & Hamid Muhammed (2007)* came to similar conclusions. They observed a flattened peak in the green and an increased reflectance in the red along with a decreased reflectance in the near-infrared region of the spectrum. *Moshou et al. (2004, 2006)* differentiated healthy, nutrient stressed and yellow rust (stripe rust) infected wheat stands by using a spectrograph with a classification accuracy of about 95%. They developed disease detection algorithms, based on band filtering, data normalisation and neural networks. An on-site system for the discrimination of yellow rust infected wheat stands by various regression analyses of vegetation indices was developed by *Huang et al. (2004)*. *West et al. (2003)* created a hypothetical optimal disease detection system. In these studies, various sensor systems have been used in a scope of application close to the target.

There is also a high potential for disease mapping with satellite-/airborne remote sensing data. In *1974*, for example, *Kanemasu et al.* detected diseases in wheat prior to the harvest by ratios of ERTS-1 bands. *Apan et al. (2004)* discriminated sugarcane crops which were severely infected by orange rust diseases from non-infected crops by using several hyperspectral indices. By applying a linear spectral unmixing method for multispectral and hyperspectral airborne data, *Du et al. (2004)* successfully detected citrus pest stress. *Jacobi & Kühbauch (2005)* distinguished between infected and non-infected wheat plots using the Normalized Difference Vegetation Index (NDVI). Meanwhile, soybean anomalies caused by iron chlorosis were found by *Shaw & Kelley (2005)* via supervised classification analysis of multispectral aerial images.

Further work is nevertheless needed for a better understanding of the spatiotemporal characteristics of plant diseases, to develop detection tools that are applicable for multitemporal analyses and the temporal dimension of crop diseases and their sensor-based identification has to be analyzed in greater detail. In addition, a comparison between the potential of near-range sensor approaches and remote sensing has still to be done.

1.4 Importance of the temporal dimension of crop diseases

Besides the spatial dimension, Precision Agriculture also has a temporal dimension, as plant stresses – in particular plant diseases – develop dynamically in both dimensions. Management actions are precisely adjustable in space and time, depending on the location where in-field heterogeneities occur and the date on which management actions are feasible and most effective. The number of agrochemical applications may thus be reduced and their timing improved. With regard to fungicide applications, the identification of temporal similarities and differences between different plant diseases is important for a determination of the course of epidemics. It can help to predict yield losses (*Xu & Ridout 1998, Pethybridge et al. 2005*) and allow for a pathogen-specific fungicide application.

In addition, the temporal dimension of stressors is of high importance for a sensor-based detection of plant diseases as fungicide applications are limited to crop growth stages *(West et al. 2003)*, the detection-date of crop infections is a crucial and restrictive factor. The use of sensor-techniques is still cost-intensive and a more profound knowledge about the optimal time of detection (growth stage) and required temporal resolution of sensor data is needed. In *1986*, Jackson et al. emphasized that timeliness, frequency of coverage, and spatial resolution of satellite-based sensors are the major constraints for a utilization of these data for farm management applications. Timeliness implies the time between data acquisition and data provision for the farmer, whereas frequency of coverage describes the temporal resolution of a sensor system (repetition rate) that is additionally affected by cloud cover. In the meantime, satellite sensor data are available with substantially improved spatial resolution in such a way as to enable them to get used for Precision Agriculture. A remaining limitation is thus the temporal character of the data, which can be overcome by future sensor systems with improved temporal resolution (e.g. RapidEye). Declining timeliness and/or decreasing frequency of coverage reduce usefulness of data for farmers.

Multitemporal studies of the spatiotemporal dynamics of crop diseases may provide information about these required parameters to avoid temporal over- or under-sampling. While over-sampling via sensor data would cause higher costs due to additional data acquisition and processing, under-sampling may results in a reproduction of a pseudo-phenomenon (figure 1.4). This case is called ‘aliasing’ and

is a common problem in signal processing (e.g. audio and video) (*Flaten & Parendo 2001*). However, aliasing and in particular temporal aliasing is transferable into other disciplines. Temporal aliasing may happen whenever a phenomenon is sampled with a frequency (f_s sample frequency) lower than the maximal frequency of the phenomenon (f_p phenomenon frequency). Extreme alias occur when the phenomenon has a sine curve. An example frequency of a phenomenon, as given in figure 1.4 (blue line), that is sampled with the frequency f_s (sample dates are indicated by vertical lines) results in an alias (red line) that models the actual phenomenon incorrectly. Hence, in cases of phenomena like sensor-detected plant diseases, infection peaks could be missed and epidemics not accurately reproduced. To avoid temporal aliasing caused by under-sampling or inappropriate sensor-sample dates, a better understanding of the temporal dimension of plant diseases is essential.

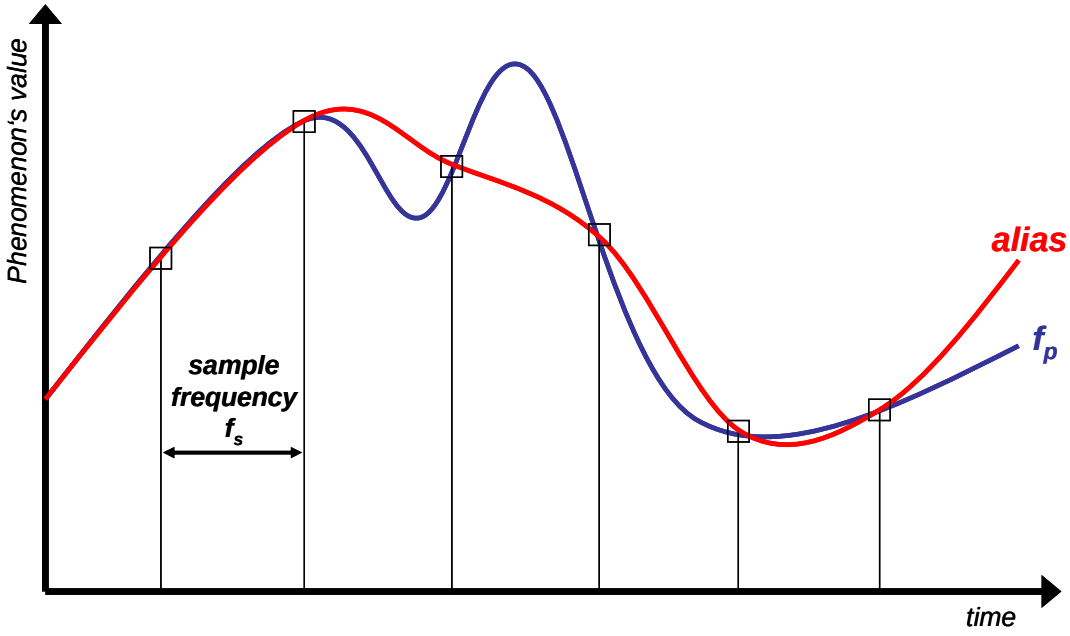

Figure 1.4: TEMPORAL ALIASING ($f_s < f_p$)

1.5 Objectives of the thesis and framework for analyses

Due to the varying impact of stresses, particularly Powdery mildew and leaf rust, on main crops in Central Europe, it is important to ecological and economical analyse these phenomena in greater detail. Understanding of their spatial and temporal characteristics as well as the potential of sensor-based detection methods of these

stressors may help to implement a precise stress control system in agricultural practices in the future. Due to their agricultural importance, this study primarily focuses on the detection of powdery mildew and leaf rust in wheat. It was accomplished in the second period of the Research Training Group 722 'Information Techniques for Precision Plant Protection' from 2004 until 2007, which is funded by the German Research Foundation (DFG).

During the first period (2001-2004), the remote sensing projects focussed on the detection of plant heterogeneities by using multispectral vegetation indices (*Jacobi 2005*), and the effect of spatial resolution (resolution scale) of satellite remote sensing data on the accuracy of crop stress classification (*Voss 2005*). The main objective during the first period was the determination of the minimal spatial resolution required for the discrimination of crop stresses. Recent studies of the second period, as described here, analysed the temporal dimension of crop stress detection, while the upcoming third period (2007-2010) will aim at assessing an optimal spectral resolution of remote sensing data for Precision Agriculture applications. Figure 1.5 shows the coordinated focuses within the remote sensing projects of the Research Training Group 722.

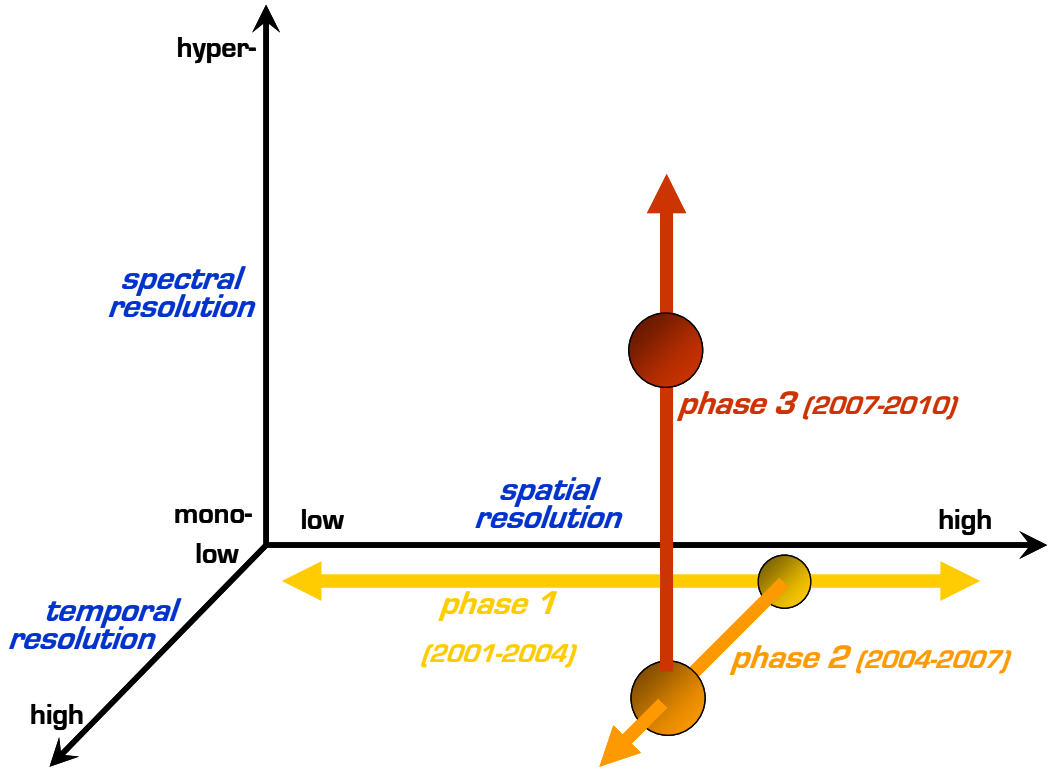

Figure 1.5: COORDINATED PERIODS of the remote sensing projects of the DFG-Research Training Group 722

In order to shed light on the temporal dimension of leaf rust and powdery mildew, this thesis mainly focuses on an analysis of the spatiotemporal dynamics of these phenomena, as well as a multitemporal sensor-based detection approach.

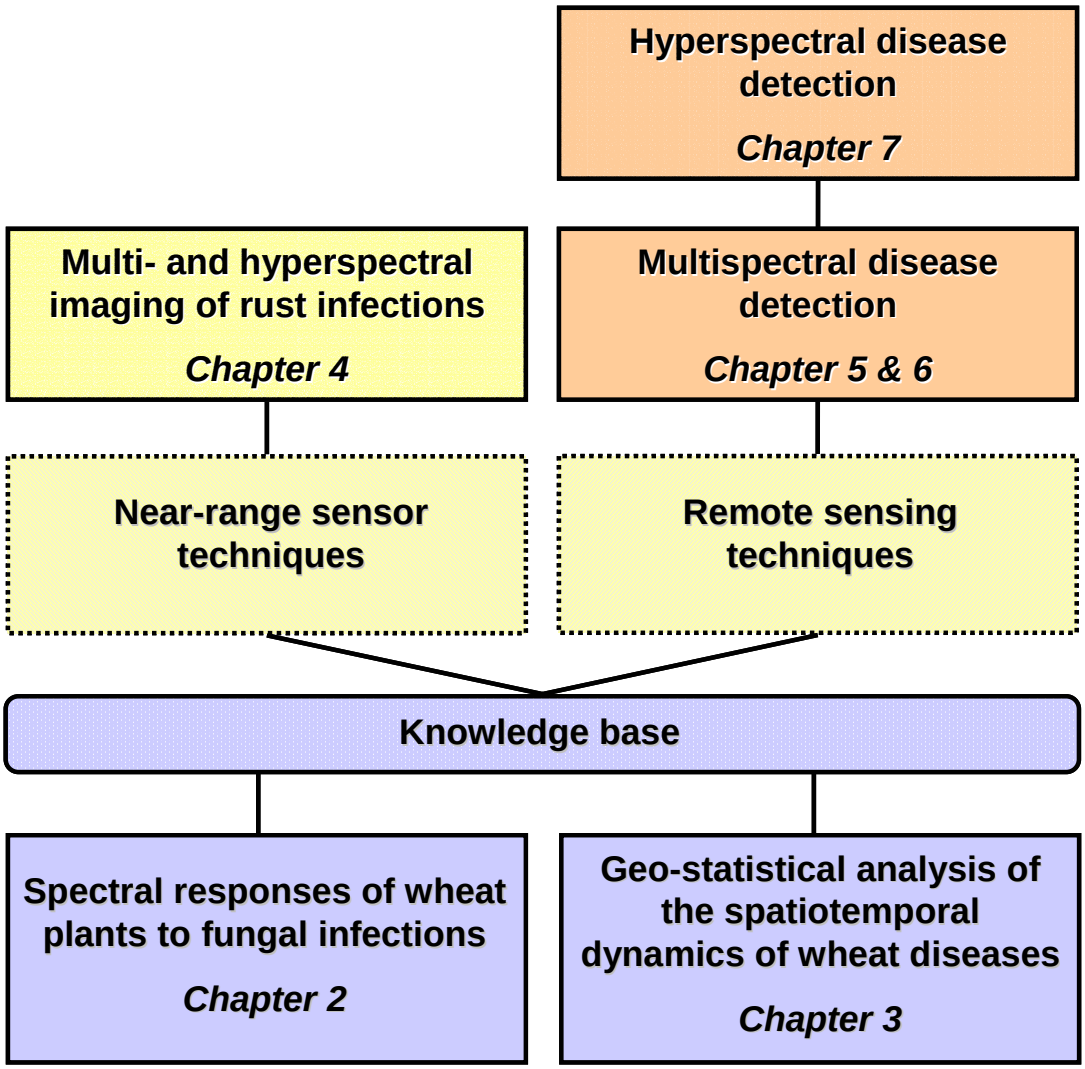

Figure 1.6: STRUCTURE OF THE THESIS with studies presented in chapters 2-7

In a number of analyses and experiments carried out in field and in laboratory, various multiscale sensors for the detection of plant diseases were tested. Figure 1.6 shows the structure of the thesis with the analyses and experiments that were carried out. Chapter 2 and 3 conduce to build an important knowledge base for a detailed understanding of the spatiotemporal as well as spectral characteristics of the phenomenon plant disease. In chapter 4, a comparison was drawn between a multispectral and a hyperspectral near-range imaging system, in order to show the potential of the sensors for disease detection. Chapter 5 and 6 focus on multispectral

remote sensing techniques for disease detection, whereas in chapter 7 airborne hyperspectral data was used for the same purpose. These studies are all briefly described in the following.

In chapter 2, typical spectral changes of wheat leaves and canopies, caused by stress impact as described in the literature, were compared to measurements taken in laboratory and field. Hyperspectral imaging data and spectroradiometer measurements of leaf rust and powdery mildew infected wheat plants were the basis for this study. A spectral mixture analysis (SMA) was applied to spectroradiometer measurements in order to derive pure endmembers, which gives information about the spectral characteristics of severely infected wheat.

The spatiotemporal dynamics of leaf rust and powdery mildew in wheat were analysed in a field experiment (chapter 3) in order to gain a deeper understanding of the phenomena and define typical species-dependent characteristics of disease spread. Disease severity data as well as other relevant plant parameters were collected multitemporally. Spatial dynamics of both diseases were assessed by cluster analysis (SADIE, Spatial Analysis by Distance Indices) while temporal characteristics (epidemic trend) were assessed by using statistical parameters. Thereby, a feature selection procedure determined statistical parameters that are relevant for a categorization of disease trends into four classes which are characterized by different temporal dynamics. In addition, critical periods for each disease were defined to accurately control the epidemics.

A laboratory experiment helped to determine the potential of two different near-range sensor systems for multitemporal monitoring of leaf rust infected wheat crops with regard to an early detection of infected stands, which is described in chapter 4. A comparison between a hyperspectral (120 spectral bands) and a multispectral (3 spectral bands) imaging system showed the benefits and limitations of each approach.

The potential of multispectral remote sensing for a multitemporal analysis of crop diseases was analyzed in a field experiment aiming at early detection of crop infections (chapter 5). A 6-ha field plot of winter wheat, containing all possible

infective stages of the leaf rust and powdery mildew pathogens, was monitored with three satellite images with high spatial resolution in order to assess the spatiotemporal analysis of the infection dynamics with remote sensing. An image classification method using spectral mixture analysis (SMA) results and a vegetation index was applied to classify the data into areas showing different levels of disease severity.

In chapter 6, simulated endmembers were used for a SMA of spatially high-resolution multispectral data in order to detect unspecific crop stresses without the use of any ground truth. In order to assess typical reflection changes of crop canopies caused by stress impact, four different fields showing apparent characteristics were investigated. With the resulting information, simulated endmembers were then generated and used for a SMA. The developed method is a simple and beneficial tool to identify areas of reduced crop vigour or to quantify site-specific stress impact without having knowledge about field conditions.

The last chapter (chapter 7) provides an outlook for the third period of the Research Training Group 722 and addressed both the potential of, and differences between, hyperspectral and multispectral remote sensing data for early detection of powdery mildew in wheat. Optimal endmembers were selected from the images using an endmember selection procedure and endmembers were modelled representing pure characteristics. Disease severity as observed in field was compared to the fraction images of the SMA by regression analyses.

The integration of this thesis in geosciences and Geography results from the key questions that are traditionally closely related to these sciences, such as: how is a phenomenon distributed in space; how can its pattern be detected; how operate phenomena in the environment and how are different phenomena spatially related? Neither remote sensing, nor Geographic Information Systems (GIS) are discrete sciences, but rather modern tools used by various sciences in order to find solutions for these questions (*Löffler 1994*). One of the first Geographers that ever used airborne images for studies of the landscape ecology was Carl Troll in the 1930's (*Troll 1966*). In the present thesis, these tools were used to analyse the spatiotemporal characteristics of the phenomenon plant disease based on

geographical methodology and approaches, but it is also related to agricultural topics. Precision Agriculture can be seen as a science located in the intersection of geosciences and agricultural sciences, where the methodologies from geosciences are often applied to monitor agricultural phenomena. Thus, topics of Precision Agriculture cause novel subjects and fields of research in Geography closely related to remote sensing and GIS (*Voss 2005*). *Jürgens (2000)*, for instance, published an article in a geographic journal that deals with remote sensing approaches in Precision Agriculture. In addition, at the Department of Geography of the University of Regensburg in Germany a project was realized in 2001, in order to evaluate the acceptance of Precision Agriculture (*Voss 2005*).

Experimental designs, sensors and data

1.6 Study area and experimental designs of the field studies

The study areas are located near the cities of Bonn and Cologne in North Rhine-Westphalia in Germany (figure 1.7).

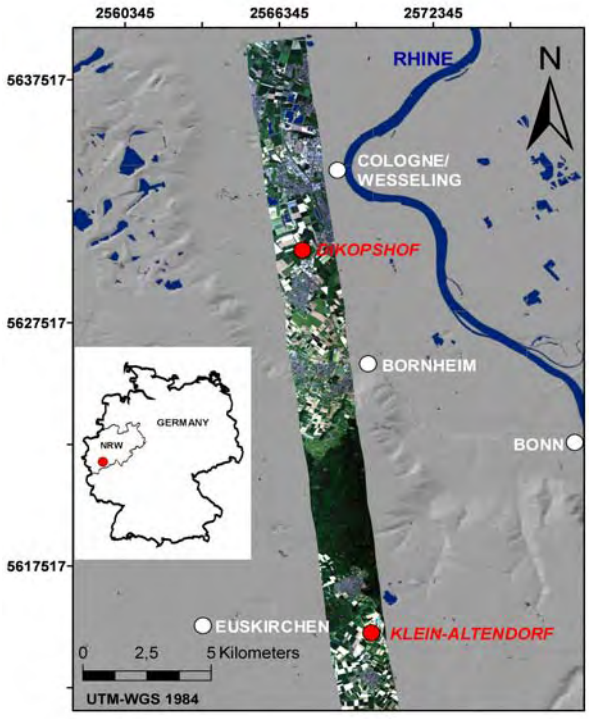

Figure 1.7: Location of the STUDY AREA. Map showing the relief with the river Rhine and lakes, a true-colour HyMap scene indicating the landscape structure of the study area

Typical agricultural units of this region vary between four and nine hectares field size with the main crops being wheat, sugar beet, barley and maize. The main test site is located at 50°37'N, 6°59'E at an altitude of 175 m ASL and is part of the experimental farm ‘Klein-Altendorf’ of the University of Bonn. The annual mean temperature of this area is 9.2°C with about 600 mm rainfall and 1534 sun hours per year. The field plot to be investigated has a size of six hectares and was chosen because of its flat topography in order to avoid complications by interpretation of remote sensing data.

A second test site is located at the experimental farm ‘Dikopshof’ of the University of Bonn at 50°48’N, 6°57’E with an altitude of 62 m ASL. Climatic conditions and agricultural characteristics very similar to those of the test site ‘Klein-Altendorf’.

In 2005, an experimental field plot was designed at the experimental farm ‘Klein-Altendorf’ for a detailed analysis of the spatiotemporal dynamics of leaf rust and powdery mildew (figure 1.8).

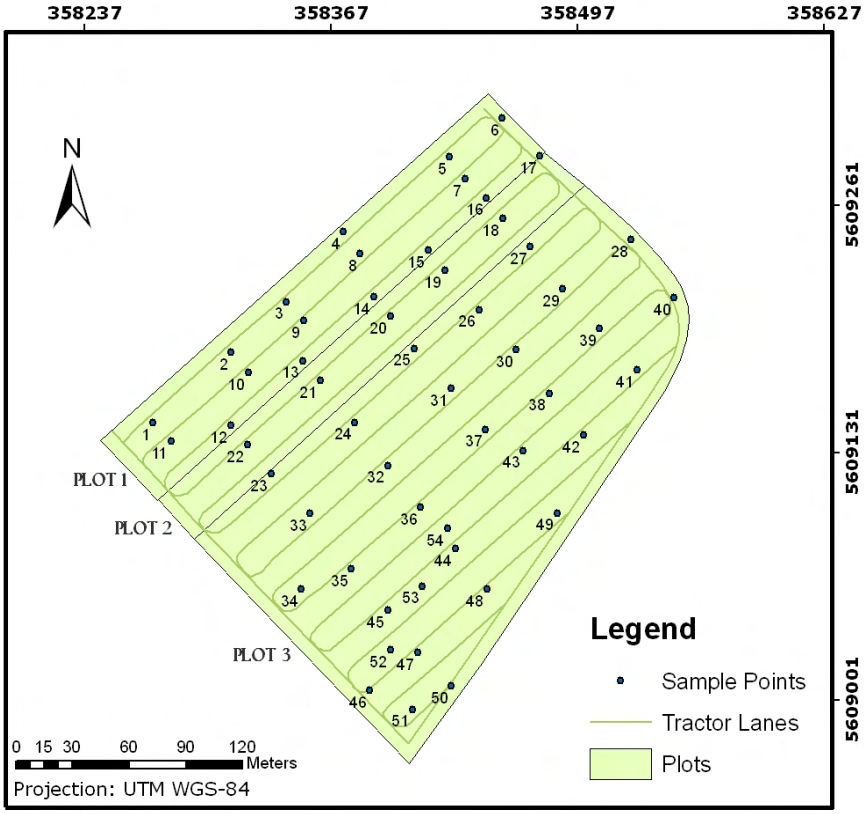

Figure 1.8: EXPERIMENTAL DESIGN of the investigated field plot in Klein-Altendorf in 2005

The winter wheat cultivar ‘Chancellor’ that is vulnerable to these pathogens was sown in November 2004. The field plot was divided into three sub-areas: While plot 1 had a width of 45 m (3 tractor lanes with a management width of 15 m), plot 2 had a width of 30 m and plot 3 showed a width of at least 120 m. To reduce the presence of undesirable stress factors such as nitrogen deficiency or weed infestation, all plots were treated uniformly with fertilizers and herbicides.

The three sub-plots received different fungicide applications to ensure a variety of disease severity. In order to ensure that at least one area remained disease-free, plot 1 was treated with fungicides twice (11 May 2005 at BBCH 34 and 09 June 2005 at BBCH 57) (the BBCH-scale is a system for a uniform coding of phenologically growth stages developed by *Zadocks et al. 1974*). A mixture of the fungicides – Opus Top (BASF, Ludwigshafen, Germany) at a dose rate of 0.8 l ha^{-1} and Flexity (BASF, Ludwigshafen, Germany) at a dose rate of 0.4 l ha^{-1} – was applied on the first application date. For the second application of plot 1, the fungicide Juwel Top (BASF, Ludwigshafen, Germany) was used at a dose rate of 1.0 l ha^{-1}. Plot 2 was only treated once, with the same fungicides and rates as plot 1 (11 May 2005 at BBCH 34), to cause a reduced or delayed infection. This analysis focuses on plot 3, the largest plot with no fungicides applied so that the fungal infections could spread naturally. Without any artificial inoculation of pathogens, powdery mildew and leaf rust appeared in the field.

1.7 Data and sensors

On 10 dates between 21 April 2005 (BBCH 30) and 23 June 2005 (BBCH 73), ground truth data were collected at 50 sample points in field. These were defined in a GIS prior to the vegetation period. In addition, another four sample points (points 51-54) representing areas with obvious crop infections were defined during field inspections (stratified sampling) and were used for remote sensing analyses only. At each sample point, particularly, severity (percentage of infected leaf area) of pathogens, growth stage, growth height and DGPS readings were collected. In order to accurately define the percentage of vegetation cover, digital images (nadir taken) covering an area of about one m^2 were acquired at each sample point by a Canon PowerShot A95 with a resolution of 5 mega pixels. Vegetation pixels in the images

were identified by a supervised image classification procedure that is described below. A combine-mounted yield-mapping system provided quantitative information about yield distribution. Soil characteristics were investigated by EM38 measurements of the apparent electrical conductivity (ECa) (Geonics Limited, Ontario, Canada), which represents a useful tool to obtain information about soil heterogeneity.

Sensor data such as spectroradiometer measurements were taken by an ASD FieldSpecPro (Analytical Spectral Devices (ASD), Boulder, Colorado, USA) over the whole vegetation period in 2005 at certain sample points. This spectroradiometer has a spectral resolution of 1.4 nm and measures in 512 bands in the spectral range of 350 to 1050 nm. In order to ensure comparability of these multitemporal measurements, all spectra were sampled around solar noon, at a maximum of possible irradiance (incoming radiation intensity per unit solid angle in Watt per steradian per square metre ($W\ sr^{-1}\ m^{-2}$)), respectively.

Remote sensing data from the spatially high-resolution multispectral QuickBird sensor were acquired for both study areas in 2002 and 2005. The sensor has four spectral bands in the visible (VIS) and near-infrared (NIR) spectrum with a spatial resolution of 2.4 m (center wavelengths: band 1: 495nm, band 2: 560nm, band 3: 660nm, band 4: 830nm). In addition, a flight campaign from the German Aerospace Center (DLR) with the airborne Hyperspectral Mapper (HyMap) sensor was carried out on 28 May 2005. The HyMap-system is a whisk-broom scanner with an ax head double mirror which acquires 126 spectral bands with a bandwidth of 16nm (in the VIS and NIR region) in the spectral range between 450 nm and 2480 nm at a nominal spatial resolution of 4.0 m.

In a laboratory experiment, a hyperspectral and a multispectral imaging system were used to monitor leaf rust infections in wheat. Hyperspectral data were acquired by the SOC-700 (Surface Optics, Corp., San Diego, CA, USA), a portable line-scanning push broom imaging system. Spatial and spectral image dimensions were 640 x 640 pixels with 120 equally distributed bands in the range of 410-910 nm. Spectral resolution was about 4 nm by a mean full width at half maximum (FWHM) of 4.55 nm. The main components of the sensor system are a pair of folding mirrors, a C-mount

lens (Schneider Xenoplan 1.9/35mm) and an imaging spectrometer (IMSpector V9). One of the mirrors is rotating to provide scanning. The lens images a column of scanned data to a slit of the spectrometer with a width of 25 microns. A ‘row’ of imaged points is spread out spectrally along the y-axis and afterwards imaged on to a 640 x 480 pixel silicon CCD array, with a 12 bit dynamic range. The data is binned by 4 in the y-dimension with the result of a 640 pixel-row of data. Each data set provides 640 scans, stored as 16 bit unsigned integer images. Recorded radiometric values are convertible to reflectance values by presence of a calibrated reflectance standard in the image. The rotating mirror of SOC-700 makes it possible to acquire a dark image prior to each measurement, which represents the instrument noise caused by the detector or electronics (*Rascher et al. 2007*).

Multispectral data were acquired using the MS3100 camera (Redlake DuncanTech, San Diego, CA, USA). The spatial dimension of images was 1392 x 1040 pixels with a spectral dimension of 3 bands in the VIS and NIR. The output was stored as 10 bit images. The MS3100 uses a beam splitting prism and three CCD sensors to acquire imagery within the 400-1100 nm spectral range. Different band configurations could be chosen with a total spectral coverage of 5 bands. Due to three available CCD-sensors, the system acquires only three bands at once. For this analysis, the ‘CIR’-configuration with green, red and near-infrared band was chosen. Center wavelength of the green band was 550 nm with a FWHM of 40 nm, 660 nm for the red band (FWHM 40 nm) and 800 nm for the near-infrared band (FWHM 65 nm).

Figure 1.9 provides an overview of the spatial, spectral and temporal resolution of all sensors used in this analysis. Only very high spatial resolution data was used with the coarsest resolution of 4 m of the HyMap data. The range of spectral resolution of the sensors varied between 3 and 512 spectral bands. The x-, y- and z-values are given in brackets for each sensor.

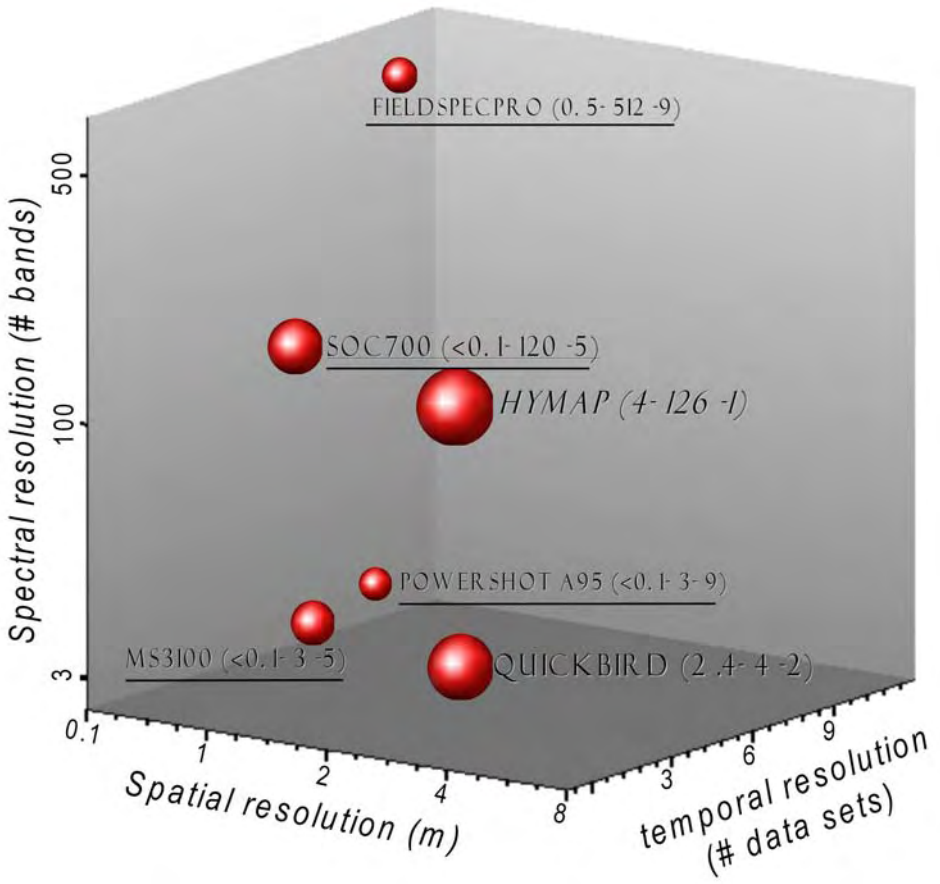

Figure 1.9: Spatial, spectral and temporal RESOLUTIONS OF THE USED SENSOR SYSTEMS. Near-range sensors are indicated by an underline.

Chapter 2

Spectral responses of wheat plants to fungal infections

2.1 Introduction

This chapter aims for building a knowledge-base for a detailed understanding of the spectral characteristics of the phenomenon plant disease. A detection of crop stresses is only possible by detecting symptoms caused by a stressor. The most challenging part is to distinguish different stress factors by the spectral characteristics of their symptoms, because most stresses cause very similar spectral changes (*Bauer 1985*). A detection of fungal infections in wheat requires profound knowledge about changes of reflection behaviour of single leaves or entire canopies affected by pathogens. A comprehensive review regarding typical spectral properties of healthy vegetation canopies and leaves was provided by *Bauer (1985)*.

Basically, there are typical changes in reflection behaviour of plants caused by diseases. In general, pathogens cause a reduction of plant chlorophyll content due to necrotic or chlorotic lesions that affect the reflection in the VIS and red-edge region of the spectrum (550 nm; 650-720 nm), due to necrotic or chlorotic lesions. Browning effects by senescence of infected spots influence the VIS and NIR (680-800 nm) as well as the short wavelengths infrared (SWIR) (1400-1600 nm and 1900-2100 nm) due to dryness. Regarding the canopy structure, pathogen infection changes the canopy density and leaf area, which can be observed in the NIR and cause an increased transpiration rate in thermal infrared (TIR) spectrum (8000-14000 nm) (*Malthus and Madeira 1993, West et al. 2003*). In addition, some pathogen species show a characteristic compound of pigments at higher infection stages. Due to these characteristics, there is a high potential for sensor-based detection of infected crops. *Lorenzen & Jensen (1989)* analysed healthy and powdery mildew infected barley leaves using a spectroradiometer and observed an increased reflectance of infected leaves in the 498 and 664 nm chlorophyll-absorbing region of the spectrum. *Larsolle & Hamid Muhammed (2007)* came to similar conclusions. They observed a flattened

peak in the green, an increased reflectance in the red together with a decreased reflectance in the near-infrared region of the spectrum. *Sasaki et al. (1998)* found similar characteristics by analysing spectral reflectance measurements of infected cucumber plants on leaf scale.

The objectives of this chapter were (i) to track the multitemporal variability of vital wheat canopy reflectance; (ii) to determine the spectral differences between different infection stages of wheat at canopy scale in order to compare it to the conclusions of previous studies; (iii) to quantify reflectance deviations caused by fungal infections at leaf scale and (iv) to derive a pure spectral signature of a 100% powdery mildew infected wheat canopy by spectral mixture model applied to spectroradiometer measurements.

2.2 Methodology

Reflectance spectra of the wheat canopy were multitemporal collected in field by an ASD FieldSpecPro spectroradiometer from 21 April 2005 (BBCH 30) to 23 June 2005 (BBCH 73). A calibrated reflectance standard (Spectralon, Labsphere, North Sutton, NH, USA) was used as reference prior to each measurement to allow for conversion to reflectance values. The sensor head was tripod mounted at a height of 1.5 m above ground. In addition, pure soil spectra were collected.

In order to indicate the multitemporal variation of healthy wheat spectra, data collected at sample point 14 (see figure 1.7) was used over the growing season. Selected field spectra were also used to demonstrate differences between the spectral characteristics of healthy, medium and severely leaf rust infected wheat canopies. Therefore, the measured spectra of the sample points 20 (healthy), 47 (20% infected leaf area) and 25 (40% infected leaf area) taken on 23 June 2005 were used exemplarily. All spectra were pre-processed; in particular a Savitzky–Golay filter was applied to smooth the data (*Savitzky & Golay 1964*). In contrast to moving average filters, the Savitzky-Golay filter tends to maintain relevant features in the spectra. Based on a polynomial regression within a certain interval (in this case 6 wavelengths) this approach calculates a filtered value at each wavelength (*Savitzky & Golay 1964*). For a more detailed analysis of the spectral differences caused by leaf rust, the percentages of differences between healthy and infected spectra were

calculated in order to indicate relevant wavelengths. In addition, wheat stands were monitored in laboratory by the hyperspectral imaging system SOC-700. Spectra indicated characteristics of single infected leaves and were compared to those of entire canopies. On the basis of these images, spectra of healthy, infected and senescent wheat leaves were obtained. The image acquisition of these data is shown figure 4.1 (chapter 4).

This chapter additionally focussed on the derivation of pure spectral signatures (endmembers) of absolute healthy and completely powdery mildew infected wheat canopies. Whereas healthy wheat stands can mostly be found in field, completely infected stands with 100% infected leaf area are rare or even nonexistent. Accessorily, most spectra collected in field – the healthy as well as the infected wheat spectra - are influenced by soil fractions, due to common vegetation covers of less than 100%. In this case, four different endmembers/components existed in the wheat field: healthy wheat, powdery mildew infected wheat, soil and shade. Most collected field spectra thus represent a mixture of these endmembers.

A spectral mixture analysis (SMA) assumes that each pixel spectrum is a linear combination of finite number of endmembers. The spectrum of an endmember ideally represents the signature of a pure component (100% of the signal). A pixel containing multiple endmembers can be mathematically described using a linear spectral mixing model (*Adams et al. 1986*). If the spectra of all pure endmembers that are contained in a pixel spectrum are known, the fraction of each endmember in a pixel can be modelled *for each wavelength* by the following equation *(Adams et al. 1986)*:

$$DN_i = \sum_{j=1}^{n} (R_{ij} * F_j) + E_i \qquad (1)$$

where,

i = band

j = number of endmembers

DN_i = reflectance value of a pixel in band i

R_{ij} = known reflectance of the endmember j in band i

F_j = pixel fraction of the endmember j

E_i = error for band i

SMAs are usually applied to remote sensing image data, in order to estimate the fraction of certain components/endmembers within each pixel (abundance). However, a spectrum measured with a spectroradiometer can be considered as one pixel and thus a spectral mixture analysis was applied to this kind of data. For the investigated wheat field and the collected spectra, the exclusive presence of the four mentioned components could be ensured, documented by digital images taken at the same locations as the spectra. On 28 May 2005, a high vegetation cover was dominant and thus only shaded soil appeared. Therefore, spectra of pure shaded soil were collected. To derive pure endmember of healthy wheat and infected wheat, spectra taken at two sample points were used. Whereas at sample point 42 – where no fungal infection occurred – a spectrum of healthy wheat was collected, at sample point 51 a spectrum of powdery mildew infected wheat with a disease severity of 40% was measured. These two sample points were chosen due to similar vegetation cover fractions of over 90%.

The soil fraction of each spectrum was determined by a supervised classification of the digital images using the ENVI 4.2 software (Research Systems Inc., Boulder, CO, USA). A maximum likelihood classifier used manually chosen regions of interests (representing soil and vegetation) to classify the images into the class soil and vegetation. The vegetation and soil fractions were calculated by image statistics respectively. In order to reduce an error caused by larger viewing angles, only the central parts of the classified images were used. Figure 2.1 shows the process of derivation of the vegetation fraction using the nadir taken digital images.

Figure 2.1: DERIVATION OF THE VEGETATION FRACTIONS at the sample points. Red indicates vegetation and green represents soil

Vegetation and soil fractions at the two sample points as well as the pure endmember of shaded soil were known parameters. Shade corresponds to brightness and different shade fractions can thus be simply adjusted by multiplying a coefficient to spectra if the shade fraction is known. However, in this case shade fraction is at both sample points very similar and occurs in healthy and in infected stands in almost the same manner and was therefore not considered in the spectral mixture analysis. Due to the fact that the presence of unknown components could be excluded, the error coefficient in equation 1, which accounts for unmodelled reflectance and represents unknown endmembers, was in this case negligible (E_i=0).

In order to derive a pure endmember of a completely (100%) powdery mildew infected wheat canopy with spectroradiometer data, equation 1 can be re-arranged. Since the pure endmember of shaded soil is known, the pure endmember of healthy wheat can be derived by unmixing the soil fraction from the spectra taken at sample point 42. This is a prerequisite for the unmixing of pure infected endmember. The following equation was applied to *each band* of the spectroradiometer data, where the coefficients represent vegetation and soil fraction of the spectra:

$$DN_{ph_i} = DN_{h_i} * 0.92 + R_{soil_i} * 0.08 \quad (2)$$

where,

DN_{phi} = reflectance of the pure endmember of healthy wheat of band i

DN_{hi} = reflectance of the spectrum of healthy wheat collected at sample point 42 of band i

R_{soili} = reflectance of the known pure endmember of shaded soil of band i

With the known disease severity observed in field at sample point 51 (40% infected leaf area), the pure endmember of completely powdery mildew infected wheat was modelled. For *each band* the following equation was applied, where the coefficients of the first term represent vegetation and soil fraction of the spectra and the coefficient in the last term represents the fraction of healthy wheat (observed 40% powdery mildew severity). This coefficient is less than 0.6 due to a soil fraction of 4%:

$$DN_{ppm_i} = (DN_{pm_i} * 0.96 + R_{soil_i} * 0.04) - (DN_{ph_i} * 0.59) \quad (3)$$

where,

DN_{ppmi} = reflectance of the pure endmember of completely powdery mildew infected wheat of band i

DN_{pmi} = reflectance of 40% powdery mildew infected wheat collected at sample point 51 of band i

2.3 Results

Canopy spectra of healthy wheat, multitemporal collected at sample point 14, showed a high variation over the growing season (figure 2.2). In particular the green region of the VIS spectrum and the NIR spectrum showed the widest differences of up to 15% reflectance.

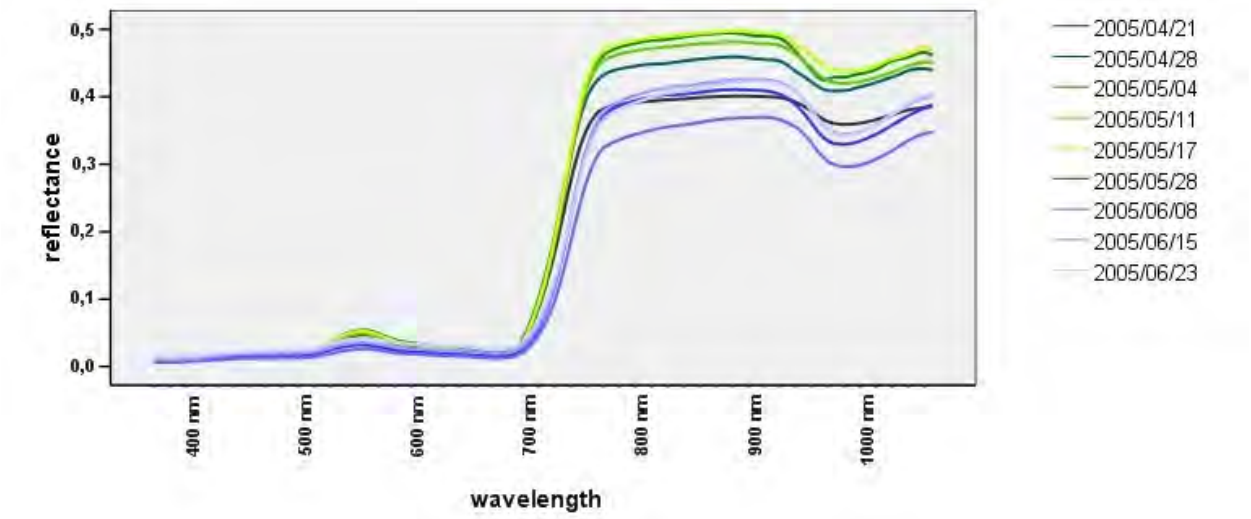

Figure 2.2: MULTITEMPORAL REFLECTANCE VARIATION OF A HEALTHY WHEAT CANOPY

This is caused by a changing chlorophyll content of the plants and by an increase of biomass/changing vegetation cover fraction and leaf area index (LAI). Whereas at the beginning of the growing season green and NIR reflectance increase due to an increase of biomass and a decrease of soil fraction (development of leaves), the reflectance in these regions decrease at higher growth stages due to maturation of

the wheat and a changing canopy structure (development of fruit). In addition, there is a slight variability due to changing factors such as sun azimuth etc. at dates when spectra were collected.

Figures 2.3a and 2.3b demonstrate the differences between healthy and leaf rust infected wheat canopies. Obviously, the NIR reflectance is more affected by the leaf rust infection as the VIS due to browning effects of infected spots that corresponds to senescence of leaves. A difference also occurred in the red-edge region, where the more healthy canopies show a steeper shape. A more detailed inspection of the changes in the VIS (figure 2.3b) shows that the difference between the peak in the green (550 nm) and the trough in the red (680 nm) decreases when plants are infected by leaf rust. That indicates a decreased chlorophyll content as chlorophyll usually reflects the green portion of incoming light and absorbs the red portion.

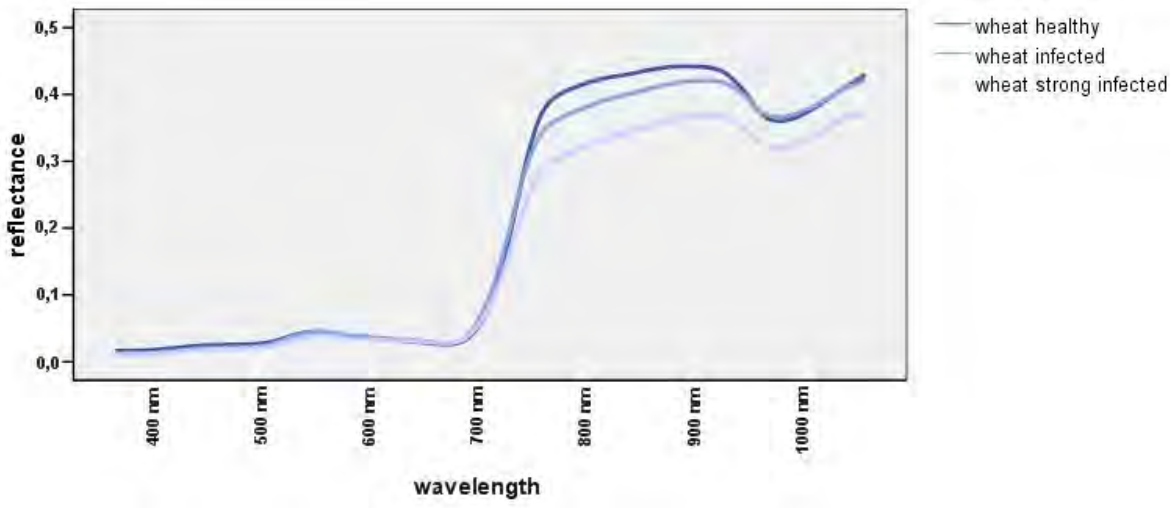

Figure 2.3a: REFLECTANCE CURVES OF HEALTHY AND LEAF RUST INFECTED WHEAT CANOPIES as measured by a spectroradiometer at sample points 20, 47 and 25 respectively, on 23 June 2005

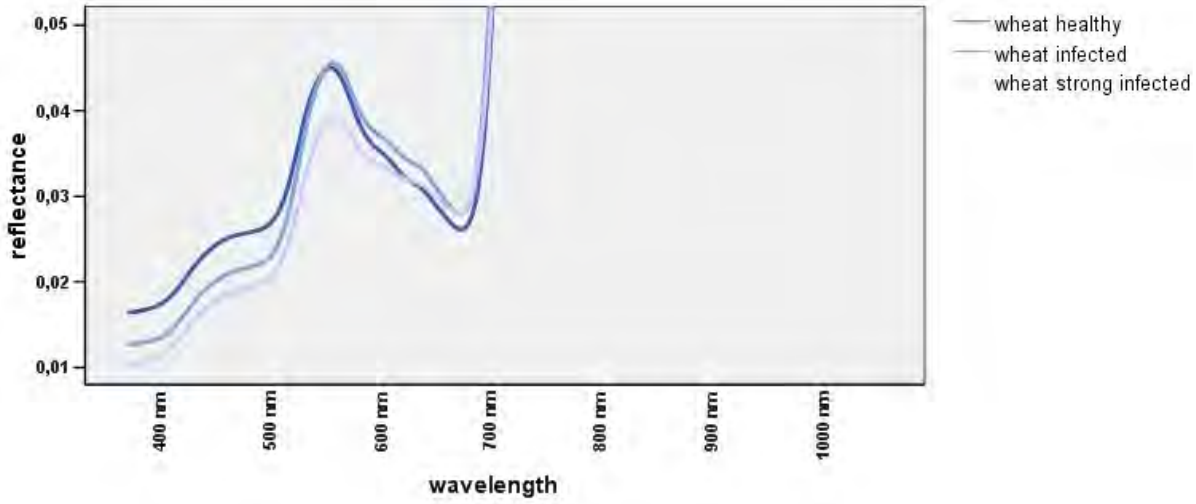

Figure 2.3b: REFLECTANCE CURVES OF HEALTHY AND LEAF RUST INFECTED WHEAT CANOPIES IN THE VIS as measured by a spectroradiometer at sample points 20, 47 and 25 respectively, on 23 June 2005

Considering the percentage differences between healthy and infected stands, greatest differences occur in the VIS, particularly in the blue region of the spectrum with up to 39% for the strong infected spectrum (figure 2.4). However, the blue region is not playing a major role for vegetation analyses and is often influenced by noise or brightness due to a weak signal. Leaf rust infections cause lower reflectance values over almost the entire range. A more systematic offset is only obvious from about 700 nm.

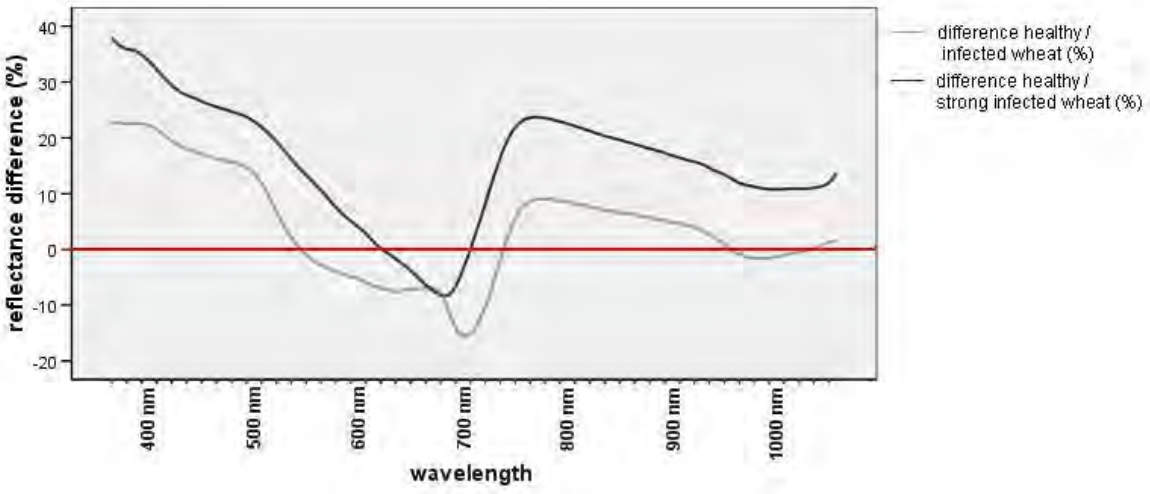

Figure 2.4: REFLECTANCE DIFFERENCES (%) between healthy and infected wheat canopies as derived from spectroradiometer measurements taken on 23 June 2005

The comparison of spectral signatures of healthy, infected and senescent wheat at leaf scale, which were acquired by the hyperspectral imaging system SOC-700, showed similar results for the red and NIR spectrum (figure 2.5). The more senescent leaves, regardless of the reason for senescence, show higher reflectance values in the red and a strong decrease of the NIR reflectance. In contrast to the spectra representing entire canopies, an increased reflection in the green region of the spectrum was found for the leaf rust infected leaf. Considering the percentage differences between healthy and infected wheat leaves (figure 2.6), similar characteristics of the curve shape occurred as for entire canopies, whereas a wider range of differences was obvious. Widest differences showed negative characteristics with values of -112% for the senescent wheat leaf and -65% for the infected wheat leaf with a trough in the red spectrum. The differences between healthy and senescent wheat leaves showed similar shapes as canopies, but with more distinct characteristics.

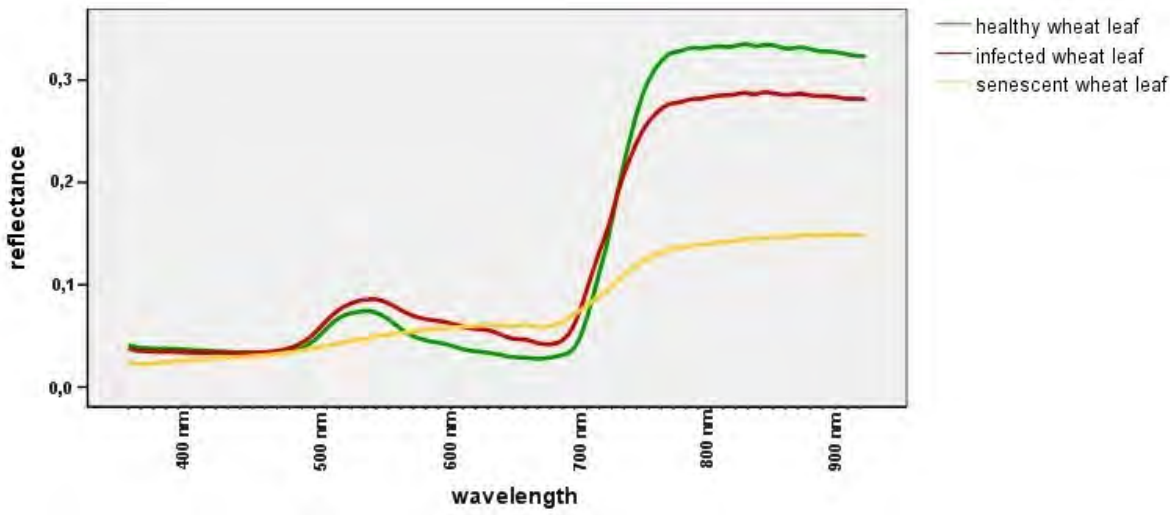

Figure 2.5: REFLECTANCE CURVES OF HEALTHY, LEAF RUST INFECTED AND SENESCENT WHEAT LEAVES, derived from SOC-700 images taken in laboratory

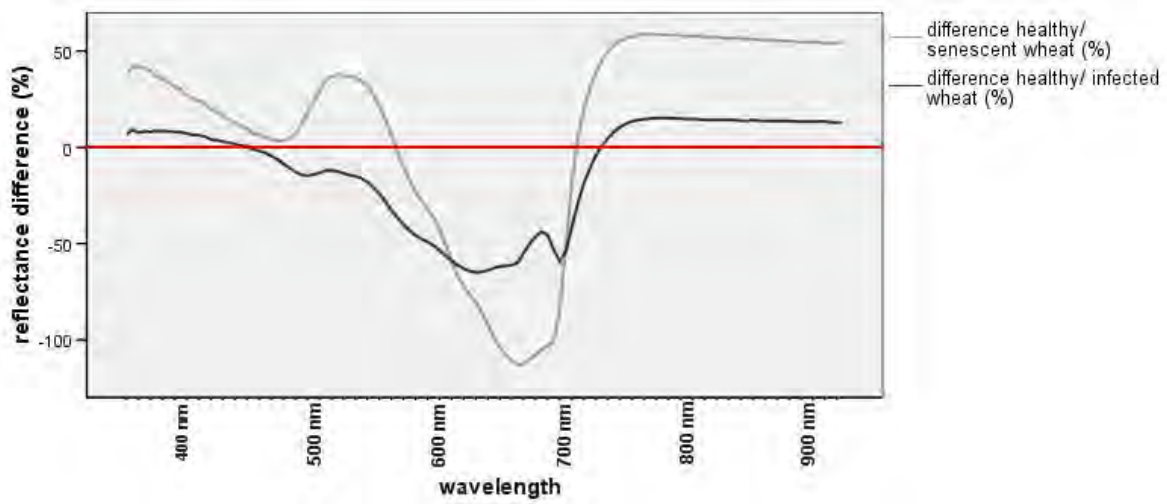

Figure 2.6: REFLECTANCE DIFFERENCES (%) between healthy, infected and senescent wheat leaves as derived from SOC-700 images taken in laboratory

Figure 2.7 displays the results of the spectral mixture model applied to the collected field-spectra in order to derive a pure endmember of completely powdery mildew infected wheat. Whereas a pure soil spectrum could be collected in field, the endmember healthy wheat was derived using equation 2. The endmember representing wheat with 40% severity of powdery mildew corresponds to the result of the first term of equation 3. The red spectrum represents pure completely powdery mildew infected wheat as a result of equation 3. This endmember has a similar shape as expected from a senescent stand, except the lower red reflectance. In all modelled endmembers a similar portion of shade is still included.

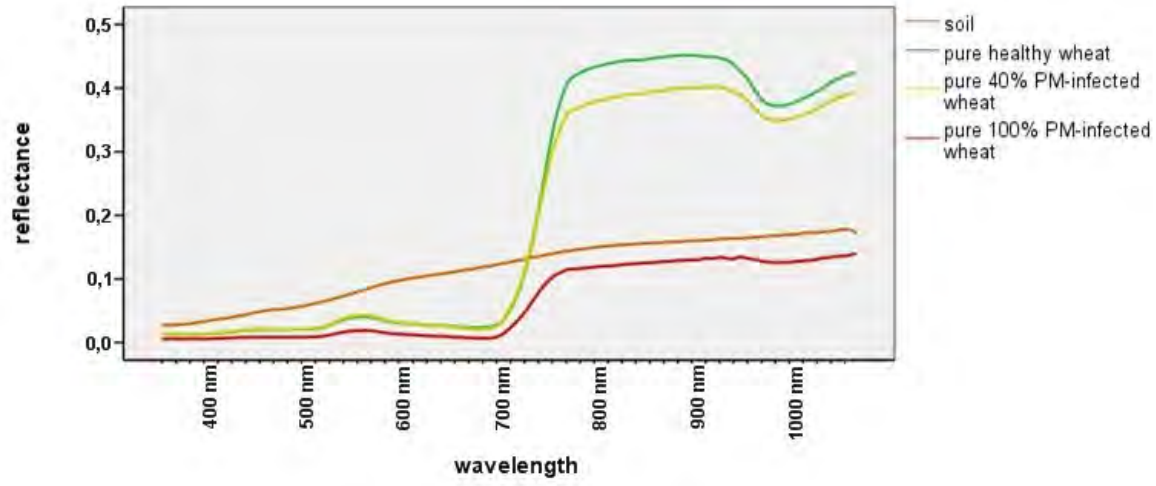

Figure 2.7: SPECTRAL SIGNATURES OF PURE ENDMEMBERS as collected with a spectroradiometer on 28 May 2005 and modelled

2.4 Discussion and conclusion

A high multitemporal variation of reflectance spectra of a healthy wheat canopy, collected over the entire growing season, was found. Plant development causes manifold changes of plant's spectral responses at certain wavelengths. Particularly changing canopy structure, biomass, LAI and soil fraction as well as maturation influences the spectra. Even though all spectra were collected at similar environmental conditions, there is a variance caused by different sun/target/sensor geometry. This might be a critical factor for each multitemporal analysis using spectral measurements, especially in cases if this variation exceeds the spectral difference caused by a factor to be observed. Hence, using multitemporal collected spectra for multitemporal analyses of crop parameters like stress effects is in some cases critical. Analysis comparing spectra taken at the same date or by a near-range imaging system - that allows for the separation of the vegetation fraction – are generally more suitable. Remote sensing data with a coarser resolution or spectroradiometer measurements covering a larger area, which causes an averaging of spatially high dynamical parameters such as canopy structure etc., are also preferable for multitemporal monitoring of crop parameters.
Spectral differences between healthy and leaf rust infected wheat canopies and leaves found in this study basically correspond to characteristics showed in previous studies that are mentioned above, e.g. *Lorenzen & Jensen (1989), Malthus and Madeira (1993), West et al. (2003)*. Only the higher reflectance values in the green region of the spectrum found for the leaf rust infected wheat at leaf scale differs from previously assessed characteristics. It could be demonstrated that a more systematic offset exists in the NIR spectrum. This might be an important fact for further analyses, modelling and possible simulations of endmembers as exemplified in chapter 6.

The exemplarily modelling of a pure healthy and a completely powdery mildew infected wheat endmember showed promising results. Only in the red spectrum of the 100% infected wheat endmember - under consideration of the effects of infections to the spectral characteristics demonstrated above - higher reflectance values were expected. Even though completely infected wheat canopies rarely occurs in natural environments – a comparison to actual measured spectra was therefore not possible – the knowledge about their spectral characteristics can play an important role for spectral mixture analyses of image data. The modelled

spectrum shows similar characteristics like a senescent wheat canopy, but with a slight red-edge. Nevertheless, modelling of pure endmembers is only an approximation. Basically, this approach of a linear spectral unmixing of field spectra might be a suitable method for a derivation of pure endmembers for a spectral mixture analysis of hyperspectral data as proved in chapter 7.

Chapter 3

Geo-statistical analysis of the spatiotemporal dynamics of powdery mildew and leaf rust in wheat

3.1 Introduction

A multitemporal remote sensing-based analysis of fungal crop diseases, such as, for instance, described in chapters 5, require a profound knowledge about the spatiotemporal characteristics of the phenomenon. This chapter therefore focus on a geo-statistical analysis of the dynamics of powdery mildew (*Blumeria graminis*) and leaf rust (*Puccinia recondita*), to aim for a knowledge-base that is helpful to interpret the results from remote sensing studies.

Fungal crop diseases often appear in patches and thus the application of pesticides on those areas where the stressors occur may be highly effective (*Oerke et al. 1994*). However, wind dispersed pathogens such as powdery mildew (*Blumeria graminis*) and leaf rust (*Puccinia recondita*) pose the greatest problem to site-specific fungicide application because the produced spores may spread over varying distances (*West & McCartney 2002*). Spraying of visible disease patches early in an epidemic would only be effective for diseases with low epidemic growth rates and thus an estimation of the area of latent infections of diseases with higher growth rates is required (*West et al. 2003*). In order to realize effective site-specific disease control and to reduce the number and improve timing of fungicide applications, a more profound knowledge about the spatial and temporal variability of each pathogen and its pattern is fundamental (*Pethybridge et al. 2005*). The identification of similarities and differences between epidemics is important for a determination of the course of epidemics and can help to predict yield losses (*Xu & Ridout 1998, Pethybridge et al. 2005*).

Pattern of plant disease epidemics are influenced by biotic and abiotic factors and reflect the interaction between host, micro-organism and environment (*Mount & Slesinski 1971*). Depending on the pathogen species, soil characteristics,

topography, plant density, host resistance, host growth stage, amount of existing spores, temperature, humidity etc. affect the spatial spread of plant diseases (*Mount & Slesinski 1971, Roelfs 1972, Nelson & Campbell 1993, Tubajika et al. 2004*). *Moschini & Pérez (1999)* analysed the influence of planting date, host resistance and weather variables to leaf rust development in multiple wheat fields and developed an empirical predictive model for general leaf rust occurrence in that region. Modelling of such complex multi-factorial and multi-dimensional systems at field scale requires detailed understanding of these interactions in a higher spatial resolution. More detailed studies that focus on the spatiotemporal dynamics of epidemics are therefore needed.

For more effective disease control the optimal timing of management actions is important. Several studies therefore focused on the first occurrence and the temporal development of plant diseases. *Pethybridge et al. (2005)* described the spatiotemporal dynamics of *Phoma ligulicola* in Tasmanian Pyrethrum fields and defined critical infection periods in order to provide information for accurate management of epidemics. *Shah et al. (2001)* determined foci of a fungal foliar and glume disease in wheat caused by *Stagonospora nodorum* and analysed their spread. They differentiated primary and secondary spread as disease management strategies could be adjusted. A multitemporal analysis of disease severity of septoria leaf spot (*Septoria lycopersici*) in tomato rows was done by *Parker et al. (1997)*. They pointed out that additional information about epidemic development is needed to ascertain the date when fungicide applications are most effective. Analytical modelling of epidemics executed by *Yang & TeBest (1992)* showed that aggregated pattern of primary infections will slow down the rate of disease development. More uniform patterns at this stage showed higher rates of disease incidence.
As mentioned in the introduction, multitemporal studies of the spatiotemporal dynamics of crop diseases may additionally provide information about optimal disease detection dates for sensor approaches. Hence, the topic that is described in chapter 1.4, i.e. the importance of the temporal dimension of crop diseases, was analysed in greater detail.

This chapter focus on the spatiotemporal dynamics of powdery mildew and leaf rust in wheat stands in order to (i) describe and discriminate the spatial spread of these

diseases, (ii) to assess their temporal dynamic/stability, (iii) to find measures that are suitable to monitor epidemics, (iv) to highlight critical infection periods that may help to find optimal disease detection/fungicide application dates and (v) to quantify yield losses they cause.

3.2 Methodology

In-field collected data of the field plot as described in chapter 1.6 were used for this analysis. In particular severity (percentage of infected leaf area) of each pathogen, growth stage, growth height and percentage of vegetation cover that were collected at 10 dates from 21 April 2005 (BBCH 30) until 23 June 2005 (BBCH 73) at 50 sample points were further analysed. For the derivation of the percentage of vegetation cover, an image classification of in-field/terrestrial taken images as described in chapter 2.2 was applied. Additionally, a combine-mounted yield-mapping-system provided quantitative information about yield distribution. Soil characteristics were investigated by EM38 measurements of the apparent electrical conductivity (ECa) (Geonics Limited, Ontario, Canada). *Neudecker et al. (2001)* noted that generally low ECa-values are typical for sandy soils (5-15 mS m^{-1}) and higher values (30-60 mS m^{-1}) represent more clayey soils with intermediate ranges typical for loamy soils. The EM38 measurements of the field plot showed only slight variability of the apparent electrical conductivity (ECa). About 92% of the measured values ranged between 20-30 mS m^{-1} indicating a soil texture of loamy silt. Hence, due to the minimization of other stress variables by adequate treatments and the indicated homogeneous soil conditions, it could be assumed that the spread of the pathogens was only marginally affected by other stress factors.

3.2.1 Analysis of the spatial dynamics of powdery mildew and leaf rust

In order to analyse the spatial pattern of the diseases, the *S*patial *A*nalysis by *D*istance *I*ndice*s* (SADIE) methodology introduced by *Perry (1995)* was applied to the in-field collected disease severity data. Particularly in plant pathology, SADIE is now being used more frequently for analysing disease patterns (*Xu & Madden, 2004*). Detailed descriptions of SADIE have been presented in previous studies (*Perry 1995, Perry 1998, Perry et al. 1999, Perry & Dixon 2002*). In addition, SADIE has been

applied successfully in the past to analyse spatial distributions of field pests like insects, diseases and weeds (*Thomas et al. 2001, Warner et al. 2003, Blackshaw & Vernon 2006, Shah et al. 2001, Pethybridge & Turechek 2003, Pethybridge et al. 2005, Winder et al. 2001*). A brief explanation of this method is given here.

A so-called transportation algorithm first determines the minimum total distance D_c that 2-dimensional spatially referenced data values c need to move in order to obtain a 'regular' arrangement, called 'distance to regularity'. This observed D_c is compared with several calculated D_c obtained by randomizations that use actually existing values. The observed D_c is compared with its distribution under the null hypothesis of randomness. The ratio of the observed and the mean D_c of the randomizations give the index of aggregation I_a that indicates the degree of spatial aggregation and allows for a comparison between different data sets. The approach thus provides an overall measure of spatial aggregation data sets with spatially referenced space. Values of $I_a>1$ thereby indicate aggregated pattern in data sets. In addition to this aggregation measurement of a complete data set, SADIE aims for the more detailed identification and measurement of clusters in spatial data and provides a cluster index v for each sample point, giving the degree of affiliation to a cluster. This cluster index based on the 'distance to regularity' method applied to each unit. The spatial arrangement and density of values in the data is analyzed by executing different randomizations. This allows an index value giving the degree of clustering at the sample location, which is independent of the original observed value. It is distinguished between two types of clusters; (i) patches (v_i) constitute neighbourhoods of relatively high values that are larger than the sample mean m and (ii) gaps (v_j) are distinguished by neighbourhoods of relatively low values that are less than m. For random arrangements of the values c, the expectation of v_i is 1 and a sample point that is part of a patch is indicated by $v_i>1$, whereas the expectation of v_j is -1 and a sample point belonging to a gap has an index value $v_j<-1$, respectively (*Perry 1995, 1998*). In epidemiology, a cluster is defined as a number of diseased plants grouped together (*Nelson 1996*).

Results of SADIE give cluster index values for each sample point and date, which were interpolated applying the kriging technique subsequently. For the interpolation, the software ArcGIS 9.0 (ESRI, Redlands, CA, USA) was used and the cluster indices were contoured (by isolines of same cluster index value) and visualized.

3.2.2 Analysis of the temporal dynamics of powdery mildew and leaf rust

An analysis of the temporal dynamic of epidemics gives information about the occurrence of diseases, their progress and possible trends. It can help to discriminate different diseases due to typical disease courses, and thus allow for a more accurate disease management. In addition to the temporal dynamic of diseases, the temporal stability of diseases is an important factor. The longer the disease impact the plant, the less their yield. The temporal disease stability thus indicates their effect on the yield as well as possible regeneration of infected plants.

Xu & Ridout (1998) emphasized that the most important parameter to describe the temporal progress of an epidemic is the growth rate of the disease. However, in order to describe the temporal dynamics more precisely, additional parameters are required that describe all characteristics of an epidemic. For multidimensional systems such as disease patterns, more than one parameter or statistics is needed to adequately represent the system (*Xu & Madden 2003*).

Following statistical parameters were calculated for the in-field collected multitemporal disease severity curves for each sample point (50) and two diseases: mean, standard deviation, coefficient of variation, root-mean-square variation, total variation, mean total variation, mean of absolute deviations from the linear regression (*Bahrenberg et al. 1999*) and a specially created parameter, the relative number of phenomenon's frequency-curve intersections of the mean, which gives information how often a disease-curve intersects the mean (equation 4 – 11).

Mean

$$\bar{x} = \frac{1}{n}\sum_{i=1}^{n} x_i \qquad (4)$$

Standard deviation

$$\sigma_x = \sqrt{\frac{1}{n}\sum_{i=1}^{n}\left(x_i - \bar{x}\right)^2} \qquad (5)$$

Coefficient of variation

$$VarK_x = \frac{\sigma_x}{\bar{x}} * 100 \quad (6)$$

Root-mean-square variation; d_{i-1} is the number of days between x_i and x_{i-1}

$$\omega_x = \sqrt{\frac{1}{n}\sum_{i=2}^{n}\left(\frac{x_i - x_{i-1}}{d_{i-1}}\right)^2} \quad (7)$$

Total variation

$$\Delta_t = \sum_{i=2}^{n}\left|x_i - x_{i-1}\right| \quad (8)$$

Mean total variation

$$\overline{\Delta_t} = \frac{1}{n}\sum_{i=2}^{n}\left|x_i - x_{i-1}\right| \quad (9)$$

Mean of absolute deviations from the linear regression $f(x) = ax + b$

$$\overline{D} = \frac{1}{n}\sum_{i=1}^{n}\left|x_i - f(x_i)\right| \quad (10)$$

Relative number of disease-curve intersections of the mean (c_{mi})

$$c_r = \frac{c_{mi}}{n-1} \quad (11)$$

A posterior assessment of the 100 severity curves and the assignment to 4 predefined categories that describe their temporal characteristics was made. The first class ‘stable’ characterizes sample points with temporally constant disease severity values. The class ‘dynamic (low)’ represents fluctuating (dynamic) severity curves with lower rates and the class ‘dynamic (high)’ represents curves showing same

characteristics with higher infection rates. Disease severity curves that show strongly increasing trends were assigned to class ‘increasing’. In order to select those statistical parameters that are relevant to classify disease severity curves into these classes, a feature selection procedure was performed using the decision tree software ‘see5’ (RuleQuest Research Pty Ltd, NSW, Australia). The decision tree learning algorithm is a commercial decision tree and rule induction engine developed by *Quinlan (1993)*. The ‘C4.5’/’C5.0’ algorithms clearly indicated which parameters are important for a classification. The input for this procedure was a training data set containing the 8 above mentioned statistical parameters for each of the 100 manually categorized multitemporal disease curves (50 for each disease).

3.2.3 Analysis of the spatiotemporal dynamics of powdery mildew and leaf rust

For spatiotemporal analyses of the disease spread, the spatial development of disease patches that were detected by SADIE was observed (size etc.). In order to investigate the spatial dynamics of the diseases only the identified patches were further analysed, since gaps are characterized by low values, i.e. healthy plant areas. By applying a threshold to the interpolated cluster indices (=1) patches were selected that correspond to areas showing high disease severity. In order to analyse their spatiotemporal dynamics, their size (area) and their centroids were calculated and monitored multitemporally.

3.3 Results

Highest yield with a mean of 8.38 t ha^{-1} was found for plot 1 that was treated by fungicides two times, whereas the one time treated plot 2 had a reduced yield with a mean of 7.07 t ha^{-1} (figure 3.1). The untreated plot 3 showed only low yield (a reduced yield of 2.2 t ha^{-1} in comparison to plot 1) caused by a strong infection of wheat crops with a mean of 6.18 t ha^{-1}. Lowest yield was observed along a 15 m wide stripe along the creek in the whole eastern part of the sample plot as well as along the south-western tip, because these areas were never treated by any agrochemicals.

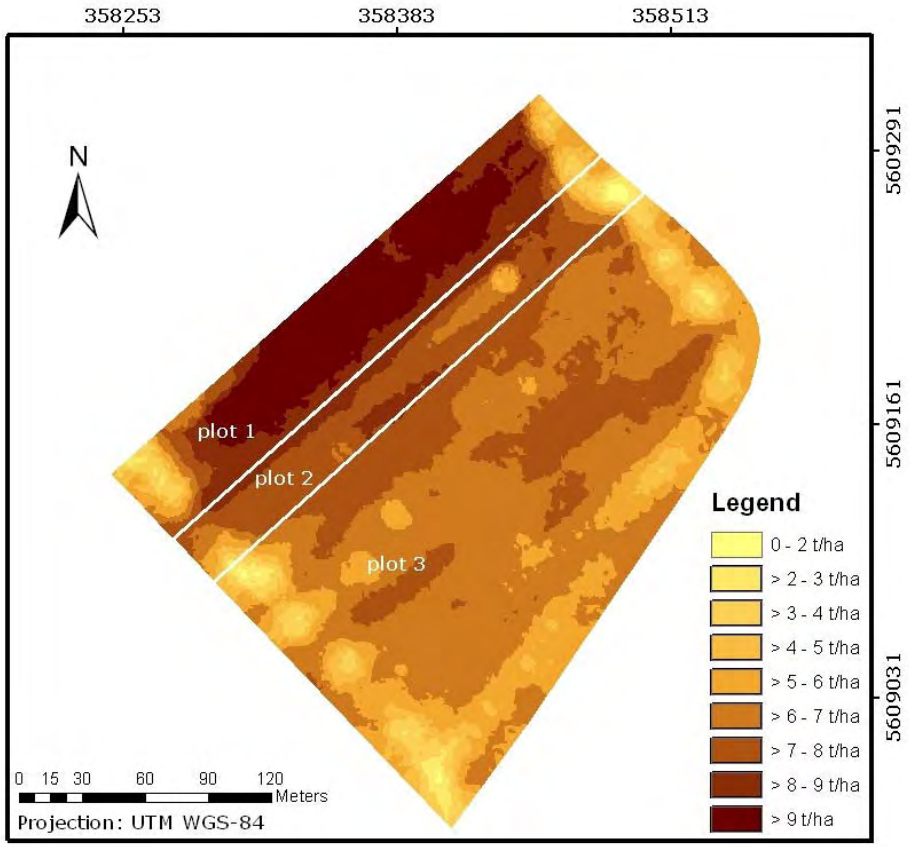

Figure 3.1: Kriging-interpolated YIELD DISTRIBUTION OF THE 3 DIFFERENTLY FUNGICIDE TREATED WINTER WHEAT PLOTS for 2005 as detected by the combine-mounted yield mapping system

Whereas growth height showed a monotonous increase (figure 3.2a), the percentage of vegetation cover, as derived from nadir taken images, showed a more fluctuating trend (figure 3.2b). At growth stage BBCH 31, when tillering was already completed, wheat started to grow (growth height increased), which caused a lower vegetation cover fraction. Vegetation cover increased by the development of more wheat leaves from BBCH 34. At higher growth stages (BBCH 41) this trend reversed, due to a strong increase of wheat leaf rust severity in plot 3 as well as maturation at higher growth stages. Particularly in the fungicide untreated plot 3, the strong leaf rust infection of the wheat already affected the canopy structure that caused significant decreasing vegetation cover fractions.

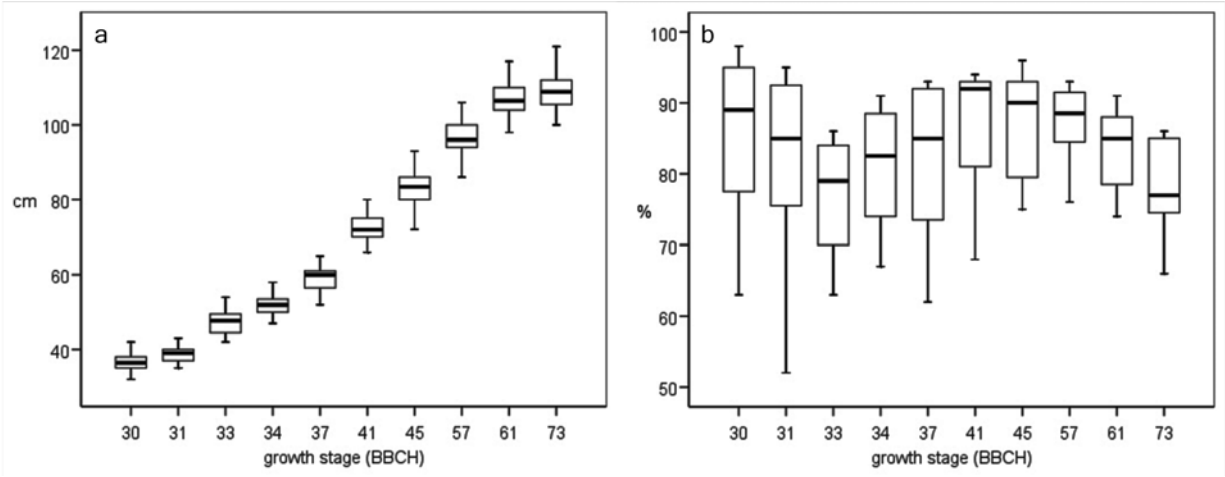

Figure 3.2a/b: Boxplots (median, quartiles and outliers) showing the DEVELOPMENT OF THE CROP CANOPY. Figure 3.2a represents growth heights (cm) measured at 50 sample points for each sampling date; figure 3.2b shows the percentage vegetation cover as derived by classification of the images taken at the same locations

3.3.1 Spatial dynamics of powdery mildew and leaf rust

SADIE results showed that both diseases occurred in patches if they show critical disease severity rates. The results for leaf rust are displayed in figure 3.3. The contours represent the cluster indices (patches >1 and gaps <-1) as detected by the SADIE algorithm, the graduated points symbolize the in-field observed disease severity and the grey-scale image gives the mean cluster index of all dates. Due to the fact that leaf rust occurred at BBCH 34, cluster indices could not be calculated for prior dates. Through growth stage BBCH 45 no leaf rust patches were identified, due to very low infection rates observed. With BBCH 45 cluster index scored values greater than 1 that are defined to be part of a patch. Two patches were identified at BBCH 57 and one clear patch was found for BBCH 61 and 73, with extreme disease severity rates up to 70%. Low mean cluster index values that were particularly found in plots 1 and 2 indicate the effectiveness of the fungicide applications. In addition, in some parts of the fungicide untreated plot 3 low mean cluster index values are obvious as well, resulting from prevailing gaps.

The spatial pattern of powdery mildew infection showed different characteristics (figure 3.4). Whereas no leaf rust infection occurred at lower growth stages, even at

BBCH 30 and 31 large powdery mildew patches were identified by SADIE in the southern part of plot 3. At BBCH 33, these patches disappeared and a small patch in the northern part occurred. No patch was found at BBCH 34 and at BBCH 37 and 41 only patches with lower cluster indices (less than 1.5) were identified. A new powdery mildew patch emerged at BBCH 45 that grew through BBCH 61 and abate until BBCH 73. In contrast to the leaf rust severity, powdery mildew rates were generally lower with a maximum of 30% infected leaf area at BBCH 31 and 57. Mean powdery mildew cluster indices reveal that even in the fungicide treated plots disease patches occurred. Similar to the leaf rust results, an area in the eastern part of untreated plot 3 was identified, characterized by low cluster index values, where disease patches never occurred.

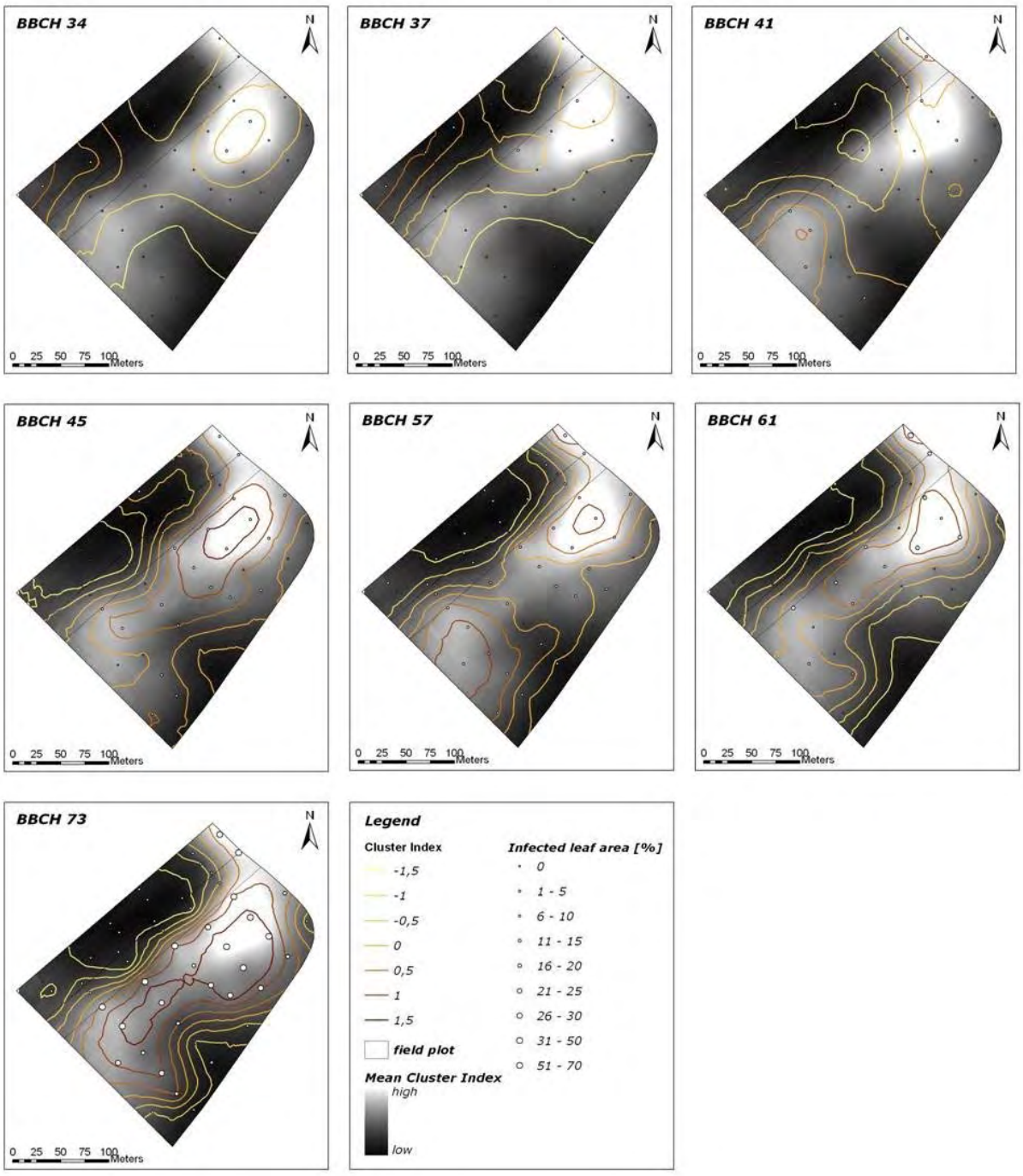

Figure 3.3: Maps display the interpolated and contoured LEAF RUST CLUSTER INDEX for each observation date that represents patches and gaps as identified by SADIE. Graduated points symbolize the in-field observed disease severity and grey-scale images give the mean cluster index of all dates

Figure 3.4 (next page): Maps display the interpolated and contoured POWDERY MILDEW CLUSTER INDEX for each observation date that represents patches and gaps as identified by SADIE. Graduated points symbolize the in-field observed disease severity and grey-scale images give the mean cluster index of all dates

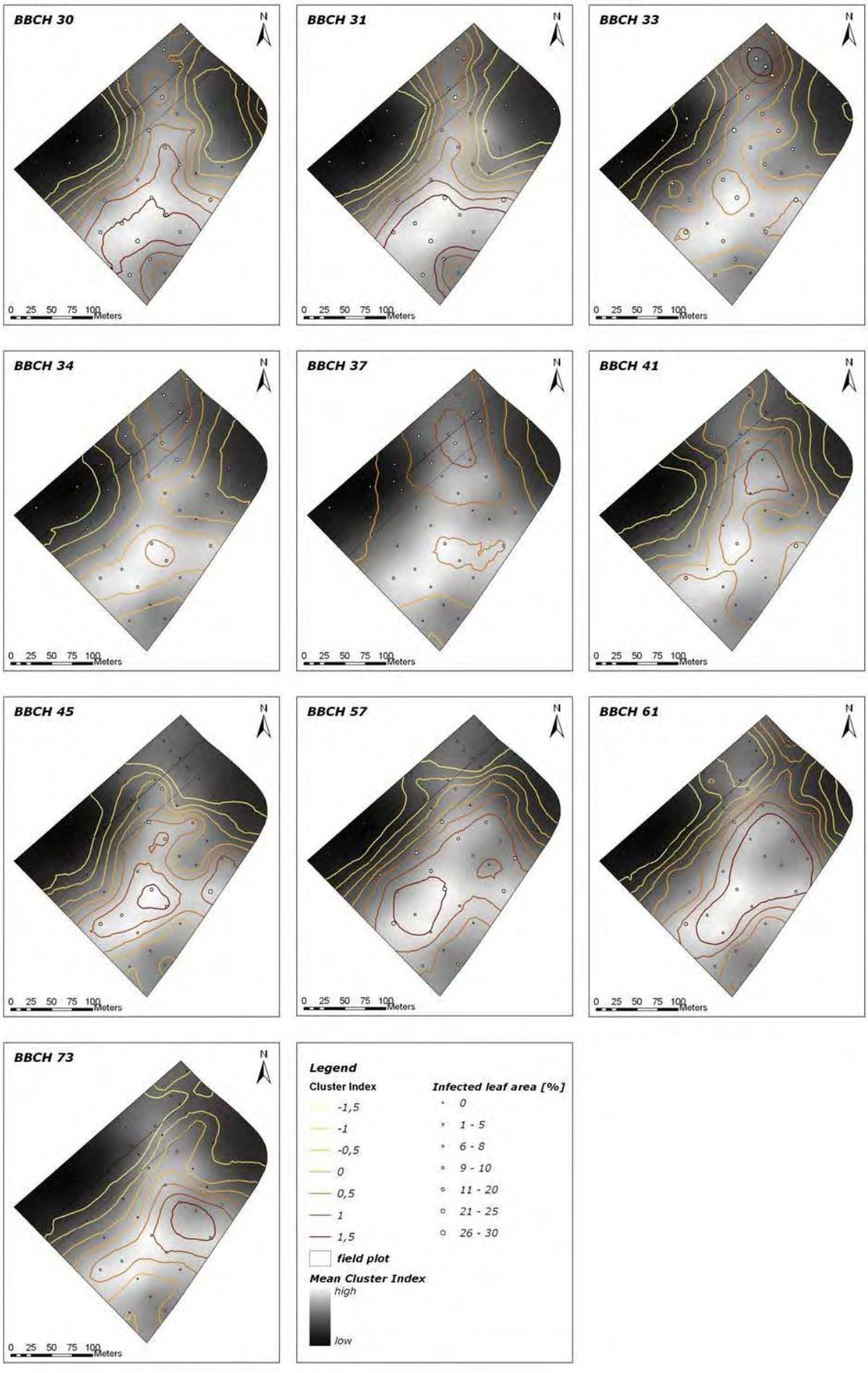
BBCH 30
BBCH 31
BBCH 33
BBCH 34
BBCH 37
BBCH 41
BBCH 45
BBCH 57
BBCH 61
BBCH 73
N
0 25 50 75 100 Meters
Legend
Cluster Index
-1,5
-1
-0,5
0
0,5
1
1,5
field plot
Mean Cluster Index
high
low
Infected leaf area [%]
0
1 - 5
6 - 8
9 - 10
11 - 20
21 - 25
26 - 30

3.3.2 Temporal dynamics of powdery mildew and leaf rust

Figures 3.5a-f display the temporal progress of leaf rust and powdery mildew epidemics from BBCH 30 until BBCH 73 for each plot. In plot 1 and 2, severe leaf rust infection could be avoided by fungicide treatments. Even in the single fungicide treated plot 2, only leaf rust infection rates less than 10% infected leaf area were observed. Leaf rust infections occurred late in the season and an exponential increase of infection rates was observed in plot 3 from BBCH 41. The infection rate increased rapidly from BBCH 61 with maximum infection rates of 70% infected leaf area. In contrast, powdery mildew occurred early in the season. Even at BBCH 30, 25% infected leaf area was observed in some parts of plot 3. In untreated plot 3, a more dynamic progress of the powdery mildew epidemic was obvious, i.e., powdery mildew severity fluctuated throughout the season.

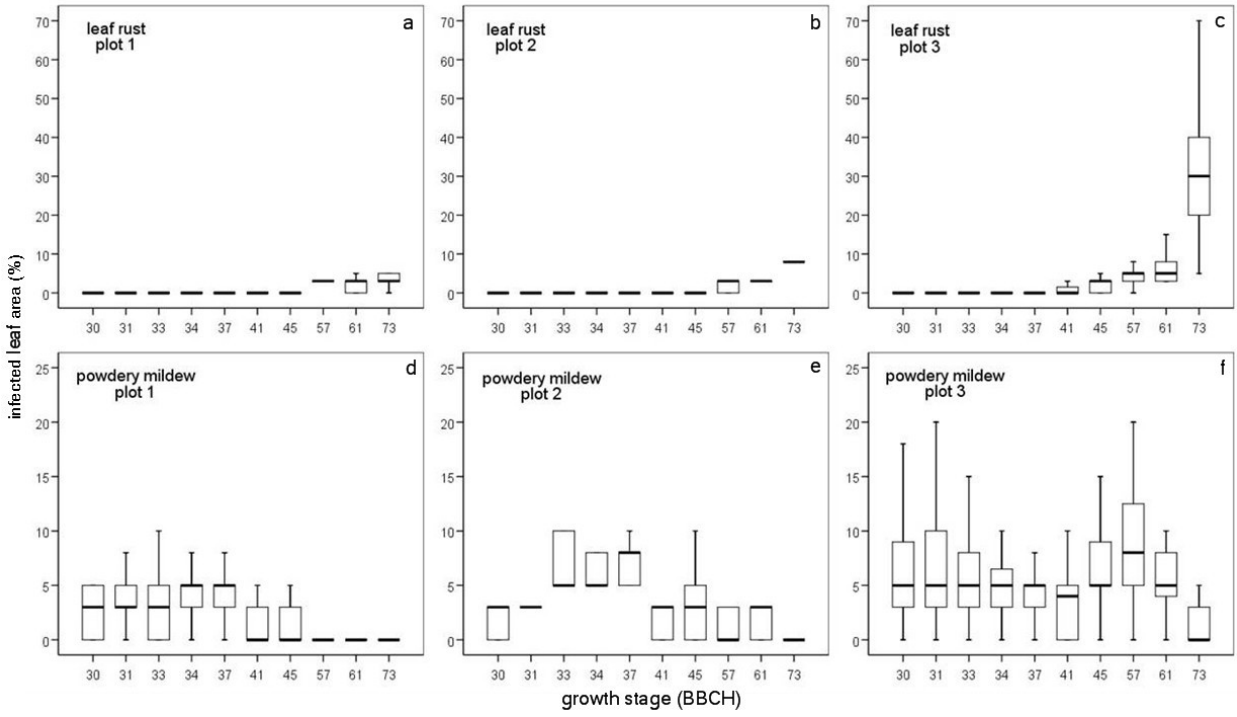

Figure 3.5a-f: Boxplots (median, quartiles and outliers) indicating the TEMPORAL DEVELOPMENT OF LEAF RUST AND POWDERY MILDEW SEVERITY in each plot

In order to assess typical trends, all disease severity curves of the 50 sample points were categorized into four classes of different temporal dynamics that are described above: ‘stable’, ‘dynamic (low)’, ‘dynamic (high)’ and ‘increasing’. For leaf rust, the temporal dynamics at 4 sample points were categorized as dynamic with low

infection rates (‘dynamic (low)’) and at 3 sample points curves were defined as dynamic with high infection rates (‘dynamic (high)’). 11 disease curves were categorized as ‘stable’, whereas 32 of 50 leaf rust severity curves showed an ‘increasing’ trend. For powdery mildew, the temporal dynamic at 23 sample points were categorized as ‘dynamic (low)’ and 10 were categorized as ‘dynamic (high)’, whereas 9 were localized in plot 3. The temporal disease dynamics at 17 sample points were categorized as ‘stable’, no ‘increasing’ curves were found for powdery mildew. Thus the temporal progress of powdery mildew followed generally a more dynamic trend than the epidemics of leaf rust.

In order to determine only relevant description parameters for a classification of temporal disease curves in these four classes, 8 statistical parameters (equations 4-11) were calculated for each multitemporal disease curve, which were the input for the applied feature selection with the software ‘see5’. The result showed that only the following 5 of the 8 statistical parameters were relevant to discriminate 4 classes of temporal disease dynamics (sorted by their importance):

1. Relative number of disease-curve intersections of the mean
2. Total variation
3. Mean of absolute deviations from the linear regression
4. Standard deviation
5. Coefficient of variation

The mean, mean total variation and root-mean-square variation could not be identified as relevant parameters for this classification. By the use of the selected statistical parameters, a detailed description and classification of multitemporal disease severity data is possible.

3.3.3 Spatiotemporal dynamics of powdery mildew and leaf rust

Similar to the temporal development of powdery mildew and leaf rust severity as shown in figures 3.5a-f, the trend of the percentage number of infections at sample points in fungicide untreated plot 3 developed (figure 3.6). Whereas powdery mildew infections were found at 85% of all sample points for BBCH 30, no leaf rust infections were found until BBCH 34. Leaf rust infections spatially spread continuously while the

number of locations with powdery mildew infections varied and declined from BBCH 57. The opposite directions of these trends at higher growth stages – and in this case particularly higher leaf rust infection rates – indicate possible interdependencies.

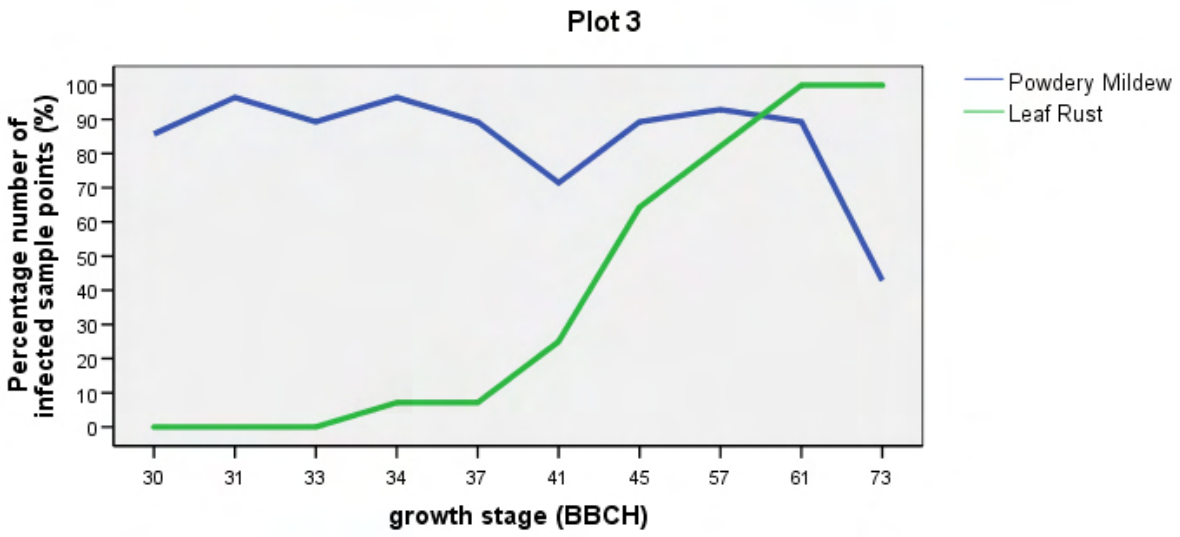

Figure 3.6: PERCENTAGE NUMBER OF INFECTIONS found at sample points in fungicide untreated plot 3

Disease patches as identified by SADIE (cluster indices >1) were further analysed in order to ascertain spatiotemporal trends for each pathogen. Therefore, the number of patches, the total patch size in hectares, the maximal cluster index and the patch centroids were determined. Figure 3.7 and 3.8 show the courses of leaf rust and powdery mildew patch characteristics. The maximal number of leaf rust patches occurred at BBCH 57, maximal number of powdery mildew patches occurred at BBCH 45. Similar to the temporal characteristics of powdery mildew epidemic, the dynamics of the spatial dimension of this disease is higher than those of leaf rust. Powdery mildew patches occurred earlier in the season, which collapsed and rebuild over the season. Nevertheless, some powdery mildew infections were observed at BBCH 34, but they did not appear in patches. The courses of the total patch size and maximal cluster index were similar in both cases with two peaks for powdery mildew at BBCH 31 and 61. The mean total patch size of both diseases was similar, by slight higher values for powdery mildew.

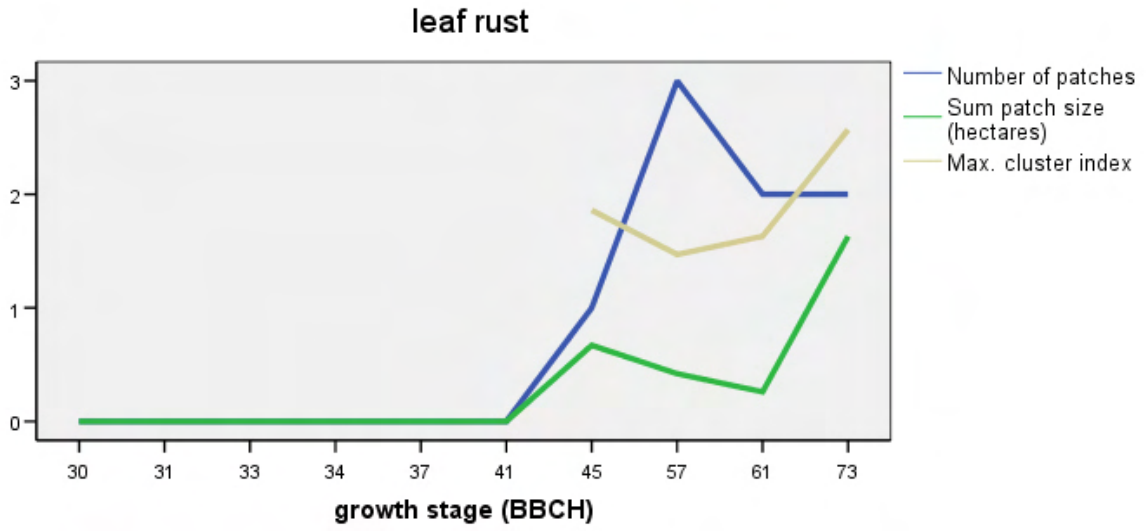

Figure 3.7: Courses of DISEASE PATCH CHARACTERISTICS FOR LEAF RUST

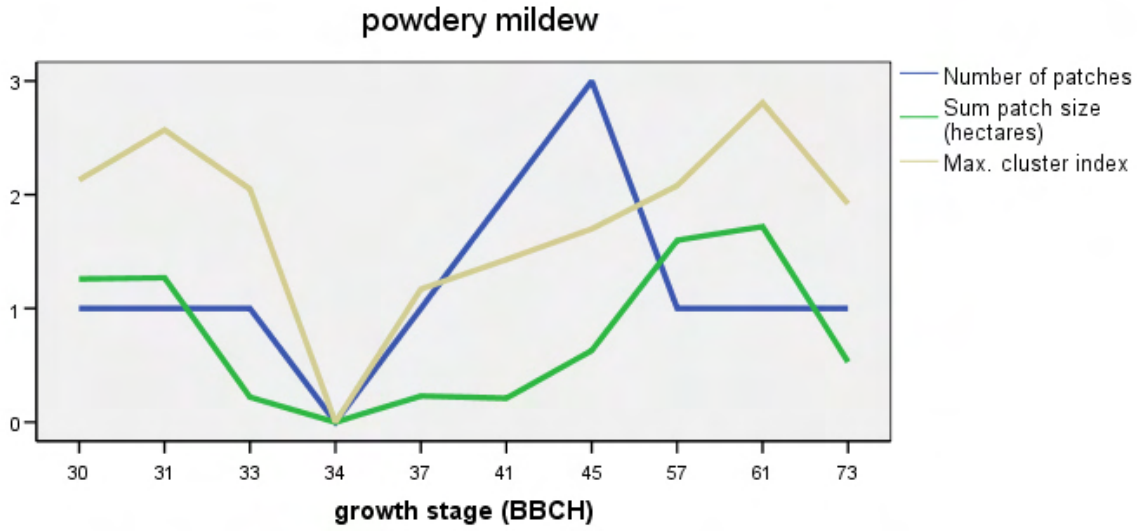

Figure 3.8: Courses of DISEASE PATCH CHARACTERISTICS FOR POWDERY MILDEW

The move of the calculated centroids of each patch was tracked, in order to extract general trajectories of disease spread. The centroids were assumed to be a representative measure for the patch position because patches exhibited a compact shape with high circularity. Only those patches were monitored, which could be found at several dates, i.e. patches that occurred only at one date were not considered and patches that merged were separately tracked before merging and after merging. The general move of powdery mildew patch centroids showed a direction that was diagonal to the seeding row (drilling direction), which corresponds to the spatial

distribution of the mean cluster index that is displayed in figure 3.4. In contrast, leaf rust patch centroids moved nearly parallel to the seeding rows with a deviation of only 0.7°.

3.4 Discussion and conclusion

Plant diseases develop dynamically in space and time. These systems have – depending on their spatiotemporal characteristics – different impacts on the host and yield. In this analysis, these diseases caused a reduced yield of 2.2 t ha^{-1} in fungicide-untreated plot 3. In plot 2, disease severity, in particular leaf rust severity, could be reduced by only one fungicide treatment per season, which caused higher yields. Thus, by reducing the number of fungicide treatments to one per season, severe infections could be avoided in this case. The progress of the epidemics implies that the effectiveness of treatments could be improved by an optimal timing of disease control actions.

For powdery mildew and leaf rust in wheat, general differences were found in their spatial as well as in their temporal dimension. At BBCH 45, the first leaf rust patch was identified by SADIE. This patch was strongly developed and spatially stable, which caused high mean cluster indices at this location. The late occurrence of leaf rust - in comparison to powdery mildew - was already observed by *Everts et al. (2001)* and they determined that leaf rust had a relatively greater impact on yield quality. In contrast, powdery mildew patches that occurred early in the season were spatially more dynamic. During the observation period, some developed patches disappeared and some new patches grew at different locations. Even though powdery mildew severity rates up to 10% were observed at BBCH 34, no patch was existent. In addition, the movement of powdery mildew patches was more dynamic than those of leaf rust. While the dominant spread direction of powdery mildew was diagonal to the seeding row, leaf rust patches moved nearly parallel.

The higher spatial dynamics of powdery mildew was strongly associated with their high temporal dynamics. In some areas powdery mildew infected wheat recovered from infections and disease patches disappeared. The temporal dynamics of powdery mildew was much higher than those of leaf rust. Higher maximal disease

severity rates of 70% infected leaf area were observed for leaf rust. However, the overall impact of powdery mildew on the hosts (but not necessarily on the yield), with maximal 30% infected leaf area, might be higher because of the longer period in which the disease could affect the plant. Powdery mildew infections were observed early in the season. In contrast, first slight leaf rust infections could not be found until BBCH 34 and severe infection not until BBCH 61. The temporal progress of leaf rust infection showed a nearly exponential trend in plot 3. The temporal progress of powdery mildew was more fluctuating and no general trend could be observed.

A categorization and description of temporal disease curves allow for a discrimination of both diseases via classification of their courses with relevant statistical parameters that were assessed by a feature selection procedure. Thus, in order to describe, distinguish, model or manage epidemics, their temporal dimension, particularly the date of occurrence, is more important than their spatial dimension. In addition, a derivation of disease trends might be important for optical disease detection systems that are often able to detect diseases without being able to discriminate different pathogens. Nevertheless, the spatial dimension plays an important role for potential spatially adjusted disease control in field.

Different spatiotemporal characteristics of the diseases cause different impacts on the wheat plants. Particularly leaf rust infections affected the wheat canopy structure as pathogens accelerates the withering of leaves. Increasing leaf rust severity (figure 3.5c) corresponded to decreasing fraction of vegetation cover (figure 3.2b). At the last observation date, this process was additionally intensified by natural maturation of the wheat.

At higher growth stages (from BBCH 57), epidemic progresses of each disease in plot 3 indicate that the diseases influence one another (particularly the opposite trends of disease severity (figures 3.5c, 3.5f), percentage number of infections at sample points (figure 3.6) and patch characteristics (figure 3.7 and 3.8)). Severe leaf rust infections suppressed powdery mildew infections. However, this could also result from changing abiotic factors, which are favourable for one and unfavourable for the other pathogen.

In this case, the most critical period for both epidemics was between BBCH 41 and 45, when both diseases increased in spatial and temporal dimension. In this period the optimal time for a fungicide application was situated for powdery mildew and leaf rust. However, even a single fungicide application in plot 2 at BBCH 34 avoided severe leaf rust infections, which could already be demonstrated by *Everts et al. (2001)*. Due to the fact that powdery mildew occurred early in the season, specific powdery mildew control at BBCH 30 could have reduced their spread. Hence, in this case, an early disease control for powdery mildew at BBCH 30 and a specific fungicide application for leaf rust between BBCH 41 and 45 would probably had been optimal disease management dates, which means a reduction of fungicide applications and a more precisely, pathogen-dependent disease control. Site-specific management of powdery mildew is however more complicated due to their higher spatiotemporal dynamic.

Chapter 4

Multi- and hyperspectral imaging of leaf rust infected wheat plants

4.1 Introduction

As already mentioned in the introduction, site-specific control of fungal pathogens requires an accurate sensor-based detection of the location and spatial variability of pathogens. Several recent studies have therefore focused on detecting crop stress caused by pathogenic fungi by near-range sensors. For this purpose, several sensor systems have been used to develop in-field-detection systems or to test possible applications of remote sensing. Cognitions obtained by near-range sensor systems can also be valuable for transferability to a larger scale like remote sensing, i.e. up-scaling processes.

West et al. (2003) created a hypothetical, optimal disease detection system and provided an overview concerning the sensor-based detection of stress. *Moshou et al. (2004, 2006)* discriminated healthy, nutrient stressed and yellow rust (stripe rust) infected wheat by using a spectrograph. They developed disease detection algorithms, based on band filtering, data normalisation and neural networks. *Lorenzen & Jensen (1989)* differentiated between healthy and powdery mildew infected barley leaves using a spectroradiometer. *Sasaki et al. (1998)* analysed spectral reflectance measurements of infected cucumber plants on leaf scale.

The objective of this analysis was to evaluate the potential of different sensor systems for multitemporal monitoring of leaf rust (*Puccinia recondita*) infected wheat crops, with the aim of early detection of infected stands. It focused on the direct comparison of sensor systems with different spectral resolutions. A comparison between a hyperspectral (120 spectral bands) and a multispectral (3 spectral bands) imaging system points out the benefits and limitations of each approach.

4.2 Methodology

In greenhouse, wheat was seeded in three boxes with a dimension of one square meter. All wheat plants were treated with specific fungicides to avoid infections of other undesirable pathogens. The stand of box 1 was inoculated with leaf rust at growth stage BBCH 33. Reflectance data of the wheat canopy were collected between growth stage BBCH 33 and 56 with different sensors. Hyperspectral imaging data were acquired on four dates, from 2 days before stand 1 was inoculated with leaf rust (BBCH 33) to 17 days after inoculation (BBCH 41). Sampling of multispectral imaging, in total four dates, began 10 days after inoculation (BBCH 35) until 41 days after inoculation (BBCH 56). Reflectance data of the different dates were always collected on the same time of the day. A constant illumination source was used to illuminate the boxes. Every external light was eliminated, to avoid interfering illumination conditions.

Both imaging systems were placed in a nadir position 175 cm above the soil surface of the boxes (figure 4.1).

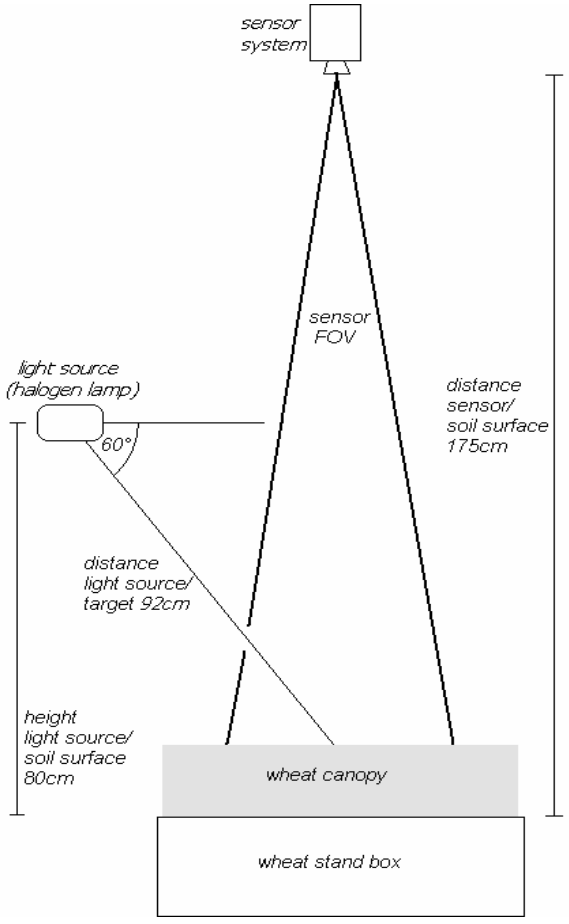

Figure 4.1: EXPERIMENTAL SET-UP showing sensor/illumination geometry

The light source was placed in a distance of 80 cm above ground with an incidence angle of 60 degrees. The distance between light source and target was 92 cm. For the hyperspectral images, a spectralon (Spectralon, Labsphere, North Sutton, NH), with a reflection rate of 50%, was placed in one corner of the FOV for subsequent conversion to reflectance values.

Hyperspectral data were acquired by the SOC-700 (Surface Optics, Corp., San Diego, CA, USA) that is described in chapter 1.7. A sample RGB-image of a wheat stand acquired by the SOC-700 is shown in Figure 4.2a.
The first pre-processing step for hyperspectral data was a linear correction by eliminating the instrument noise using dark images. Afterwards, reflectance was calculated. The pre-processing was accomplished by the program HSAnalysis 2.0 (Surface Optics, Corp., San Diego, CA, USA), all further processing using the ENVI 4.0 software (Research Systems Inc., Boulder, CO, USA).
A minimum noise fraction transformation (MNF) was applied to a subset of the data. This subset, which was the basis for all further processing-steps, excluded the area of the spectralon. The MNF transformation ordered the data in terms of image quality, due to a segregation of noise (*Green et al. 1988*). MNF transformations consist of two principal component transformations (PCA). The first transformation estimates the noise covariance matrix and rescales the noise. The second transformation is a common PCA, whereby new bands get produced. Bands with higher order of data quality contain the majority of information. The data space of these bands is associated with large eigenvalues. Higher order bands still contain a portion of signal, but noise becomes predominant. Thus, results of MNF-transformation show negligible information contents from band 16 to 120 (eigenvalues near zero). For further processing the first 15 MNF bands with large eigenvalues (<1.5 assumed to be negligible) and the compressed information were used.
Multispectral data were acquired using the MS3100 camera (Redlake DuncanTech, San Diego, CA, USA) that is described in chapter 1.7. A sample of a false-colour image of a wheat stand acquired by the MS3100 is shown in Figure 4.2b (bands: R: NIR, G: green, B: red). By pre-processing of multispectral data a minimum noise fraction transformation was applied as well. All 3 MNF transformed bands were used

for further processing of the data. The multispectral pre-processing was carried out using the ENVI 4.0 software.

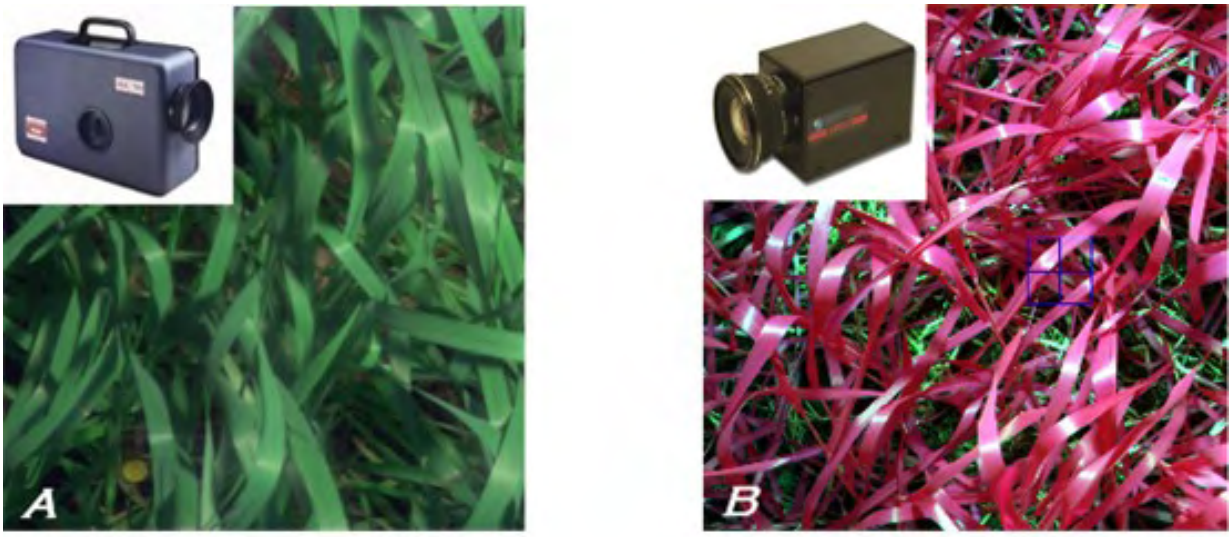

Figure 4.2: SOC-700 HYPERSPECTRAL IMAGING SYSTEM (*A*) and MS3100 MULTISPECTRAL IMAGING SYSTEM (*B*) with image examples of wheat stand #1 at BBCH 33 (*A*: center wavelengths: R: 701 nm (band 70), G: 581 nm (band 41), B: 490 nm (band 19); *B*: R: NIR, G: Red, B: Green)

4.2.1 Hyperspectral leaf rust detection

The mixture tuned matched filtering algorithm (MTMF), a specific SMA, requires a MNF transformed image and endmember spectrum. A SMA assumes that each pixel spectrum is a combination of endmembers (*Adams et al. 1986*). The output of a SMA consists of fraction images containing a subpixel-estimation of the abundance for each endmember. The requirement for a SMA is a spectral library containing all spectral signatures of each endmember which appear in the pixel spectrum. The MTMF differs from SMA that only one endmember must be known. It is a 'partial' unmixing, in which the known signature gets matched. Similar to the SMA, the result is an MF-fraction image representing estimated relative degree of match to the reference spectrum (*Boardman 1998, Williams & Hunt 2002*). In addition, the MTMF provides an infeasibility image which estimates the possibility that a pixel, in spite of its high MF-fraction values, has characteristics of unknown endmembers (false positives). Thus, low infeasibility values and high fraction values indicate a good match of the endmember.

The endmembers ‘leaf rust infected wheat’ and ‘wheat senescent’ were extracted from image-pixels with apparent characteristics.
In this case, the creation of the spectral library might be a source of error, due to the lack of diffuse light in the wheat stands. The artificial light produced a strong gradient of illumination, causing areas of specular reflectance and deep shade. Thus, spectral signatures of an endmember vary between well illuminated and shaded leaf areas and might differ from averaged spectra in the library. Data acquired under natural or artificial diffuse light may provide a more accurate basis to extract typical spectral endmembers.

4.2.2 Multispectral leaf rust detection

Similar to the hyperspectral processing steps, a spectral library containing the endmembers ‘leaf rust infected wheat’ and ‘wheat senescent’ was created. For multispectral data, the mentioned uncertainties caused by the artificial light producing highly intensive reflection areas on leaves (specular reflectance), could recognised for this data too. Multispectral signatures of pathogen infected leaves showed slight different characteristics to hyperspectral signatures. In comparison to healthy leaves, lower green reflection values were observed in hyperspectral and multispectral signatures. But in contrast to hyperspectral signatures, multispectral leaf rust infected wheat signatures showed increased red reflection.

4.3 Results

4.3.1 Hyperspectral analysis

A sample scatterplot of the MTMF result for the endmember ‘leaf rust infected wheat’ of day 17 after inoculation (BBCH 41) is given in Figure 4.3. Best MTMF-match shows high MF-fraction values and low infeasibility values. Pixels associated with high MF-fractions and high infeasibility values were identified as false positives (red circle). For these pixels the MTMF-estimation identified similar spectral characteristics of strongly infected leaf areas and senescent leaves. Thus, these false positives were pixels, which probably got mismatched by MTMF. The endmember ‘senescent wheat’ was accounted for as well by the MTMF. A threshold

(1.0) for the MF-fraction of the endmember ‘senescent wheat’ was used, eliminating pixels, which appeared as false positives in the MF-fraction band ‘leaf rust infected wheat’. ‘Leaf rust infected wheat’ showed a clear separation line along the MF-fraction value of 1.3 (black line in figure 4.3). This criterion was used as an adequate separation threshold for the class ‘leaf rust infected wheat’.

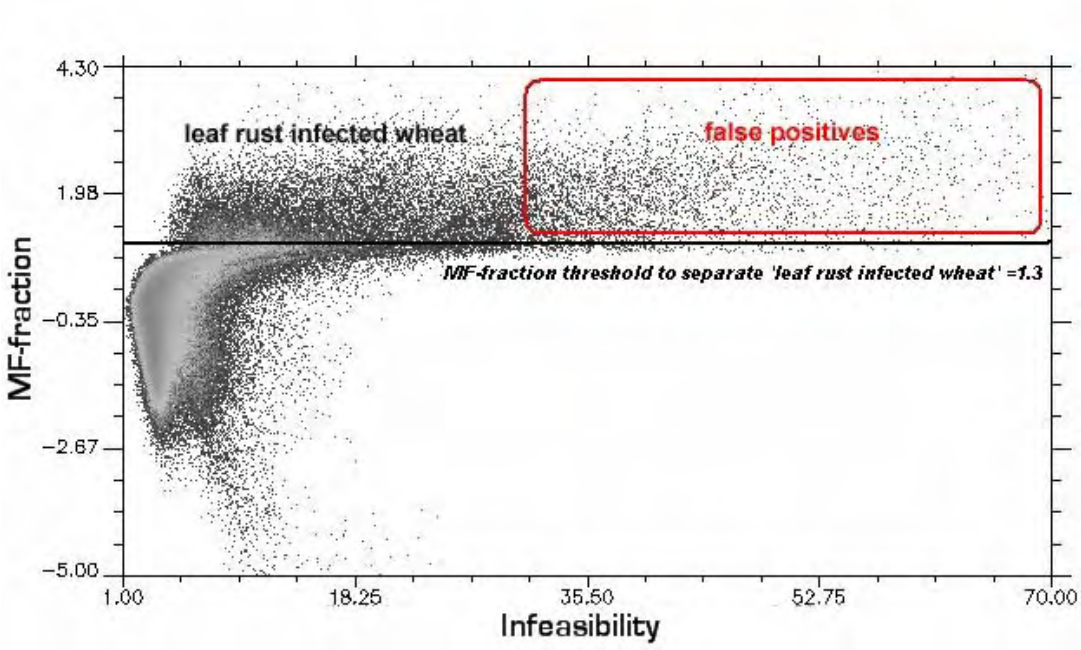

Figure 4.3: HYPERSPECTRAL MTMF-RESULT SCATTERPLOT SHOWING MF-FRACTIONS AND INFEASIBILITY VALUES FOR ENDMEMBER ‘LEAF RUST INFECTED WHEAT’ (day 17 after inoculation, BBCH 41). Conspicuous is a clear separation line along the MF-fraction value about 1.3 (notified by the black line). The red circle indicates false positives

A decision tree was created to classify all pixels showing leaf rust infections in each image automatically (figure 4.4). The first step was to mask all non soil pixels by an unsupervised ISO-data classification. ISO-data classification calculates class means in data space and cluster pixels via a minimum distance operator. Each pixel was classified to the nearest class. In our case, class 1 corresponded to soil pixels. Afterwards, only vegetation pixels of the MTMF-estimation were taken into account. The second decision classified all senescent wheat pixels using the MF-fraction threshold of 1.0 in the MTMF-fraction band ‘senescent wheat’. Thus, remaining pixels corresponded to healthy and infected wheat pixels. The last decision separated these classes by using the MF-fraction threshold of 1.3 in the ‘leaf rust infected wheat’ band, which is shown in the scatterplot.

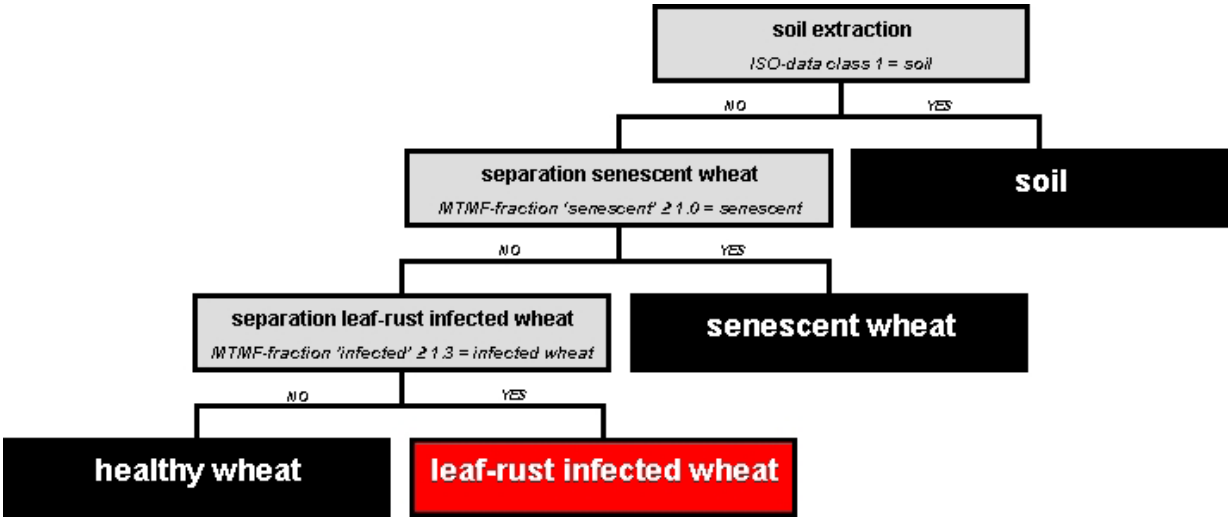

Figure 4.4: DECISION TREE FOR HYPERSPECTRAL CLASSIFICATION of leaf rust infected wheat pixels

Figure 4.5 displays the classification results of infected leaf areas of leaf rust inoculated stand 1. Figure 4.5a shows the classified image 2 days before inoculation (BBCH 33). Purple colour represents leaf rust infected pixels; black colour represents 'wheat healthy', 'wheat senescent' and 'soil'. Obviously, some leaf areas were classified as 'leaf rust infected', which might be a mismatch by MTMF. However, the presence of unknown stress factors that show similar spectral characteristics as the leaf rust infection is possible. 5 days after inoculation (figure 4.5b, BBCH 34) an increased number of pixels showing leaf rust infections were classified, even though only few infected spots were visible. On day 11 after inoculation (BBCH 35) a clear leaf rust infection was visible on some leaves and on day 17 after inoculation (BBCH 41) these infection areas widened and the stand showed strong symptoms. This corresponded to an increasing trend of classified pixels in Figure 4.5a to d, whereas the classifications of the control stands 2 and 3 indicated almost healthy plants.

There was no clear explanation for the presence of clustered false positives in figure 4.5a, c and d.

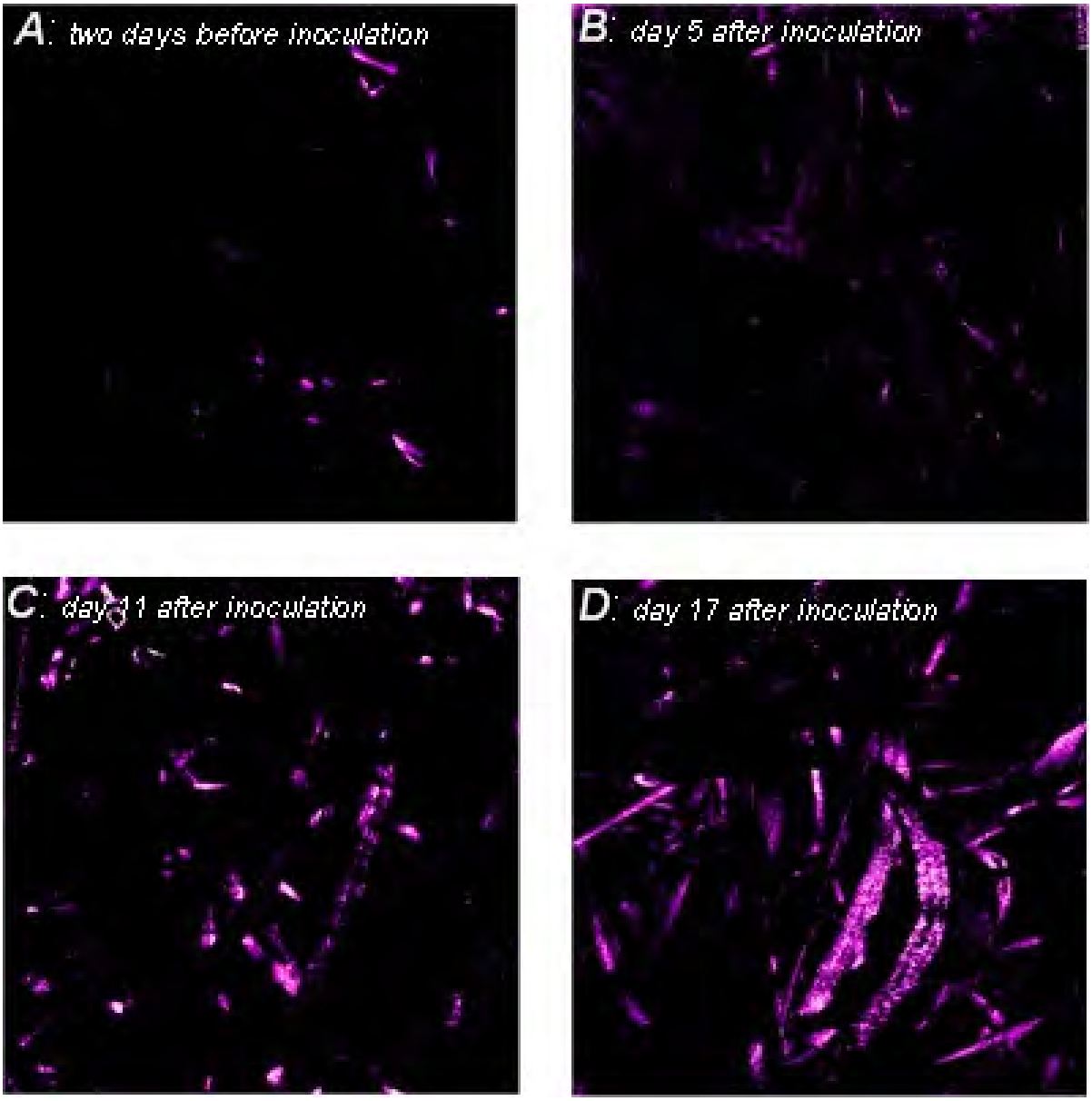

Figure 4.5: HYPERSPECTRAL MTMF-ESTIMATED LEAF RUST INFECTIONS of stand #1 of all 4 dates (A to D). For display purposes the class 'leaf rust infected wheat' has been exchanged with original MF-fraction values and classified by a colour table (purple). Black pixels correspond to soil, healthy and senescent wheat pixels. The brighter the pixels, the higher the MF-fraction values

The fractions of infected leaf area (healthy-, infected- and senescent wheat pixels without soil) were calculated for each stand to have a normalised indicator of percentage infected leaf area (figure 4.6). 2 days before inoculation, all stands were similar classified by the MTMF-algorithm with values between 0.48% and 0.73% of infected leaf area of the vegetation fraction. 5 days after inoculation an increased amount of pixels showing leaf rust infections was observed for stand 1. As infection

developed, 5% infected leaf area was detected at day 11 after inoculation and 10% at day 17 after inoculation. The amount of as 'leaf rust infected' classified pixels of the control plants always remained under a value of 1.5% (maximum value of stand #2, 17 days after inoculation) during all dates.

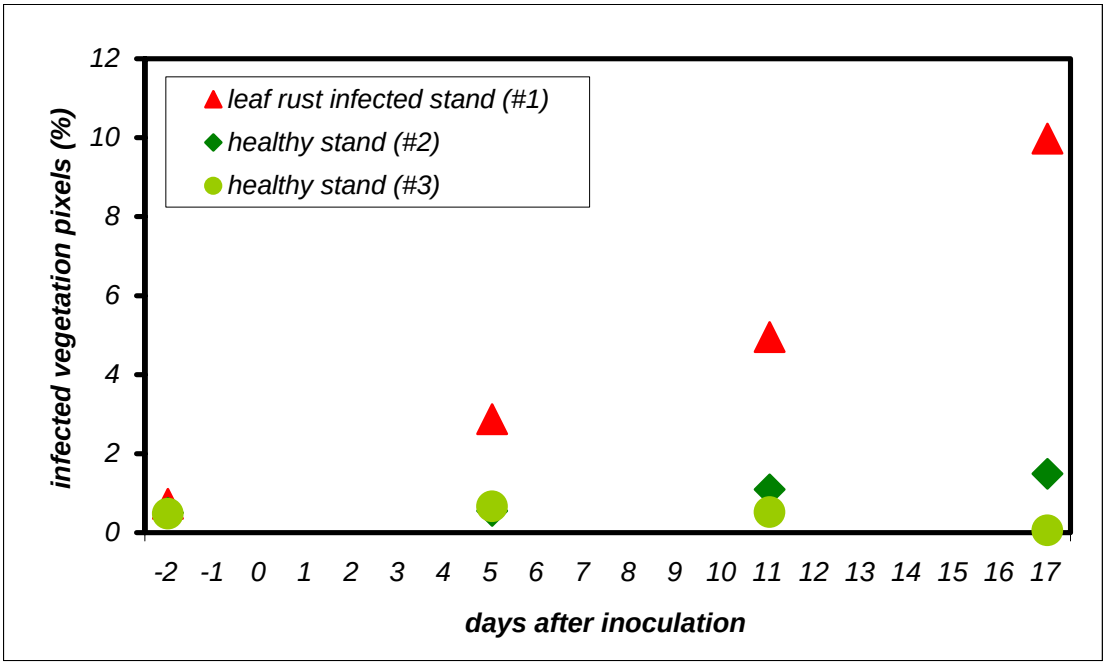

Figure 4.6: PERCENTAGE FRACTION OF INFECTED LEAF AREA of the total vegetation fraction for the hyperspectral classification result

4.3.2 Multispectral analysis

Multispectral MTMF-estimations of pathogen infected wheat pixels showed similar characteristics as hyperspectral results in the 2-band scatterplot of MF-fraction and infeasibility band of endmember 'leaf rust infected wheat' (figure 4.7). The endmember 'leaf rust infected wheat' appeared above a MF-fraction value about 1.3. This level was used as separation threshold (black line in figure 4.7). False positives had infeasibility values greater than 12.0 and were eliminated. In contrast to the hyperspectral MTMF results, where only senescent wheat pixels represented these false positives, 'over-illuminated' leaf areas caused accuracy problems for multispectral data (figure 4.8b).

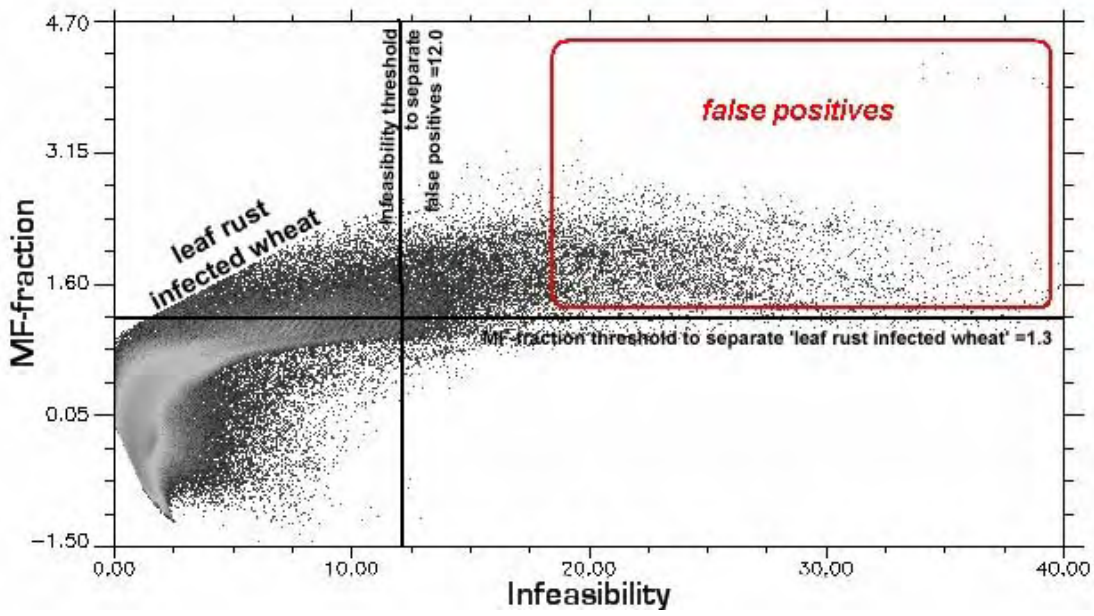

Figure 4.7: MULTISPECTRAL MTMF-RESULTS SCATTERPLOT SHOWING MF-FRACTIONS AND INFEASIBILITY VALUES FOR ENDMEMBER 'LEAF RUST INFECTED WHEAT' (day 11 after inoculation, BBCH 41). Similar to the hyperspectral MTMF-scatterplot a clear separation line along the MF-fraction value about 1.3 (notified by the horizontal black line) is conspicuous. The red circle indicates false positives. Vertical black line represents the infeasibility threshold to eliminate false positives (=12.0)

The decision tree used for hyperspectral classification of leaf rust infected pixels was changed in one respect: a term was added in the last decision node to eliminate false positives. In addition to the MF-fraction threshold of 1.3, only pixels with infeasibility values less than 12.0 were classified as 'leaf rust infected wheat'.

Figure 4.8 shows two examples of the classification result of leaf rust infected stand #1, 11 and 27 days after inoculation. 11 days after inoculation a satisfying result was achieved using multispectral data. All obviously infected wheat pixels with spores were classified as leaf rust infected. Only few pathogen stressed leaf areas without spores could be detected. In contrast, classification result of day 27 after inoculation provided poor accuracy, due to problems caused by sensor-orientated leaf areas with specular reflectance. Only pixels with highest brightness could be eliminated. At this date the spectral signatures of leaf rust infected pixels and well illuminated healthy leaf areas showed similar characteristics.

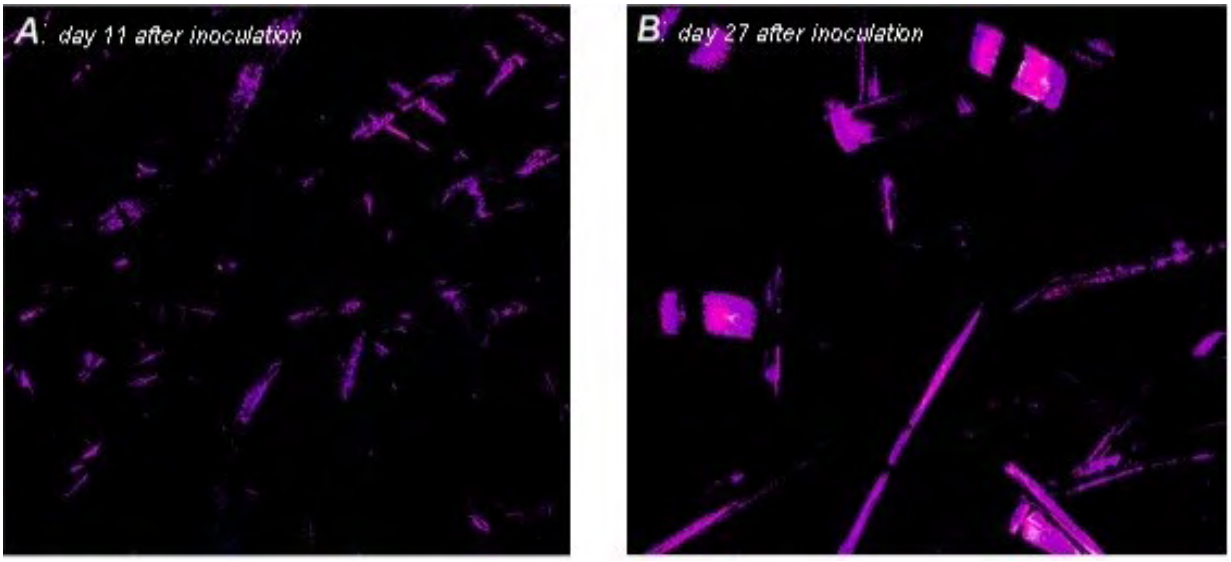

Figure 4.8: MULTISPECTRAL MTMF-ESTIMATED LEAF RUST INFECTIONS of stand #1, 11 (A) and 27 (B) days after inoculation by decision tree classification. For display purposes the class 'leaf rust infected wheat' has been exchanged with original MF-fraction values and classified by a colour table (purple). Black pixels correspond to soil, healthy and senescent wheat pixels. The brighter the pixels, the higher the MF-fraction value

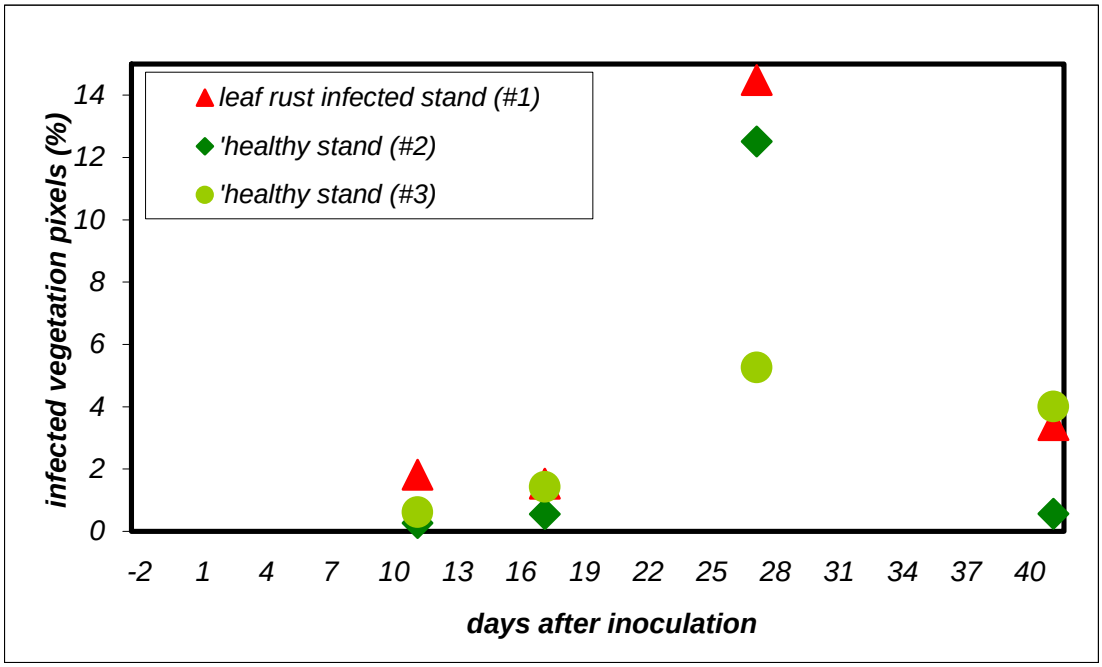

Figure 4.9: FRACTION OF INFECTED LEAF AREA of the total vegetation fraction for the multispectral classification results

The fraction of infected leaf area was derived from multispectral classification results as well (figure 4.9). For the first acquisition date of multispectral data (10 days after inoculation), infected leaf area of stand 1 was 1.82%. Control stands showed values of 0.27% and 0.62% respectively. 17 days after inoculation, the amount of infected pixels of the inoculated stand (1.53%) was only 0.1% higher than control stand #3 (1.43%). 27 days after inoculation a strongly increased amount of classified infected pixels of all stands were detected, which resulted from accuracy problems caused by specular reflectance. At the last observation date, infected leaf area as classified dropped under the value of control stand #3.

4.4 Discussion and conclusion

This chapter explored the potential of near-range acquired hyperspectral and multispectral imaging data for the detection of leaf rust infected wheat plants. The hyperspectral remote sensing system achieved satisfactory results. However, a detailed accuracy assessment was not possible due to the lack of information about the actual condition of the wheat plants (at initial infection stages it is not possible to determine spots where an infection occurs). No proper discrimination of infected and healthy wheat stands was possible with the multispectral 3-band system. However, given a substantially improved illumination condition, disease detection might be possible using multispectral imaging data.

Depending on the spatial resolution of the system, the sensor should be placed about 2 m above ground, to cover a representative area and to make a detection of small initial infection spots possible. Image area should be protected from direct sunlight.
MTMF-algorithm proofed as a suitable image analysis method to detect leaf rust infections. On the one hand, to achieve higher classification accuracies, a multitemporal spectral library is desirable, i.e. a library for each growth stage, to account for typical changes in spectral characteristics of wheat during growth. On the other hand, to reduce computation rate, particularly with regard to a creation of online-stress detectors, spectral libraries of each growth stage should contain only few spectra showing averaged characteristics of ‘healthy wheat’, ‘senescent wheat’, and ‘leaf rust infected wheat’.

The results of this analysis suggest that a hyperspectral imaging system such as the SOC-700 and hyperspectral data analyses are suitable tools for detecting crop stress caused by leaf rust, particularly with regard to early detection, which is required for an effective site-specific fungicide application. On day 5 after inoculation, more stressed leaf areas could be detected by hyperspectral data than were visible at this time. Even though, this is a very promising result, at this early infection stage a reliable validation of these results was impossible, due to the lack of information about the real condition of the wheat leaves, because there is no system available that directly measures the stress status of leaves. For discrimination of infected and healthy stands the infected leaf area derived from classification results was a suitable indicator. To make a binary decision whether a fungicide application is needed, a threshold determination of this parameter is useful. Minimum threshold value must be greater than the maximum value of control stands (in this case 1.5%).

Classification accuracy could be enhanced by improved illumination conditions. A strong illumination gradient (shaded and over-illuminated leaf areas) was the main reason of misclassifications of both data types. Multispectral imaging data show higher sensitivity to these external factors than hyperspectral data.

Chapter 5

Multitemporal wheat disease detection by multispectral remote sensing

5.1 Introduction

In contrast to - or in synergy with near-range sensor systems such as presented in chapter 4, remote sensing sensors, which provide information about entire fields, may be an appropriate tool to monitor the heterogeneity of crop vigour and could be useful to reduce fungicide application by aiding decisions on the location, timing, and dose of spray application (*West et al. 2003*). However, site-specific or timely adjusted fungicide treatments require sensor-based detection of the spatial variability of fungal infections at early infection stages.

Some studies have shown high potential for disease mapping with airborne or satellite remote sensing systems. *Apan et al. (2004)* discriminated sugarcane crops severely infected by orange rust diseases from non-infected crops by the use of several hyperspectral indices. A successful citrus pest stress detection using a linear spectral unmixing method for multispectral and hyperspectral airborne data was achieved by *Du et al. (2004)*. *Jacobi and Kühbauch (2005)* distinguished between infected and non-infected wheat plots using the NDVI.

In this chapter, a multitemporal remote sensing-based analysis of the spatiotemporal occurrence of wheat diseases is described, which was carried out in order to: i) point out the potential of multispectral data with high spatial resolution for multitemporal monitoring of fungal wheat infections; ii) investigate the earliest detection date of fungal infected wheat areas with these data; iii) find out about suitable data processing methods that constitute important requirements of precision agriculture applications; and, iv) ascertain the suitability of spatially high-resolution multispectral data for the derivation of site-specific fungicide application maps in respect to the spatial identification of diseases. This study focussed on the most common pathogens in cereals in Central Europe, powdery mildew and leaf rust.

5.2 Methodology

The investigated wheat field of this analysis is located at the experimental farm of the University of Bonn as described in chapter 1.6. Remote sensing data were acquired by QuickBird on 22 April 2005 (BBCH 31) and on 20 June 2005 (BBCH 65). Additional airborne hyperspectral HyMap data were acquired on 28 May 2005 (BBCH 45). Ground truth data as described in chapter 1.7 was used to validate the results. Due to the minimization of other stress variables by adequate treatments and soil analyses, it could be assumed that existent crop stress was predominantly caused by fungal infection.

5.2.1 Pre-processing

An accurate pre-processing of remote sensing data, including a precise radiometric and geometric data correction, constitutes one of the most important requirements for Precision Agriculture applications. A site-specific treatment of agrochemicals based on remote sensing-derived application maps can only be effective if the exact location of field heterogeneities is reproducible in data. In addition, to avoid uncertainties in data quality caused by inconsistent pre-processing-parameters in multitemporal analyses, a comparison of data sets and, if necessary, an inter-correction of data is essential. A creation of a master data set is therefore considered useful. Such master data set can constitute the basis for subsequent geometric inter-corrections as well as for validation of atmospheric corrections; and if necessary for radiometric normalization (e.g. via pseudo-invariant features) of multitemporal data. The reduction of the influence of atmospheric effects in the measured remote sensing signal is a fundamental but difficult pre-processing step. Thus, in-situ spectroradiometer measurements are essential to control the quality of the atmospheric correction, especially for multitemporal Precision Agriculture applications.

The atmospheric correction of both QuickBird images was done by the use of the software ATCOR3 for Erdas Imagine (GEOSYSTEMS GmbH, Germering, Germany). HyVista Corp. and the German Aerospace Center (DLR) carried out the pre-processing of the HyMap data. The validation of the atmospheric corrections was performed against in-situ measurements obtained with the ASD FieldSpec Pro spectroradiometer.

In addition to the repeated collection of reflectance spectra in the field, to ground truth remotely sensed data, 9 uniformly distributed white markings (0.5 m^2 each) were installed in the plot, the exact positions of which were measured by DGPS. These markings were identified in the QuickBird images and used as ground control points (GCP) for the geometric image correction using the ENVI 4.2 software (Research Systems Inc., Boulder, CO, USA). This image was used as a master data set for subsequent image-to-image corrections of the HyMap and QuickBird images.

To extend the QuickBird data set with a third scene, the HyMap image of 28 May 2005 was spectrally resampled to obtain a multispectral image with spectral characteristics similar to those of QuickBird. An in-house developed IDL-program 'BaSim' facilitates any user-predefined multispectral band simulation with regard to the band-specific relative spectral response (RSR) function. Thereby, the 126 HyMap reflectance values of each pixel were thereby multiplied by the 126 wavelength corresponding RSR-values of each QuickBird band. The sum of these products was divided by the sum of the 126 band-specific RSR-values. For a multispectral sensor simulation, *each band (b)* was simulated according to the following equation (12):

$$R_{sim_b} = \frac{\sum_{i=1}^{n} R_i * rsr_{i,b}}{\sum_{i=1}^{n} rsr_{i,b}} \qquad 1 \le n \le 126 \tag{12}$$

where,

$R\text{sim}_b$ is the simulated pixel reflectance value of the simulated band b, R_i is the pixel reflectance value of the HyMap band and $rsr_{i,b}$ is the relative spectral response value of the simulating band at each HyMap corresponding wavelength.

The results are simulated QuickBird bands that provide spectral information similar to those of the original sensor. Slight differences from original data caused by different sun/sensor/target geometry still exist. The performance of this simulation method and their validation was analysed in greater detail in a separate study, which is described in a special chapter in the appendix. The code of the developed IDL-program for simulation is given as well.

5.2.2 Classification

Lorenzen and Jensen (1989) revealed that differences in reflectance between powdery mildew-infected plants and healthy plants first occur in the visible region of the spectrum. In contrast, only very small differences in the NIR occurred in their study, indicating that infections cannot be detected with NIR imagery until the canopy structure is affected by the infection. This is only the case in late powdery mildew infection stages, when the optimal time for fungicide treatment has past (*Lorenzen & Jensen 1989*). Therefore, VIS/NIR-vegetation indices have limited potential for early detection of pathogen infections. *Apan et al. (2004)* as well as *Jacobi & Kühbauch (2005)* confirm this assumption, as they only detected crop infections with the sole use of vegetation indices at severe infection stages. Hence, an analysis of all available data bands is probably more suitable for early detection of crop diseases than the sole use of vegetation indices. For instance, *Lelong et al. (1998)* and *Du et al. (2004)* demonstrated the potential of SMA of hyperspectral data for stress detection that allows a quantification of disease severity at subpixel level.

The potential of a SMA method for stress detection was therefore tested for multispectral data that is described in this chapter. To use multiple classification parameters for the detection of infected wheat areas, a decision tree using both SMA results and vegetation index information was built. While thresholds, used by decision tree classifiers, which are optimally defined for each individual date gain higher classification rates, a classifier that performs well for various scenes is preferable. The requirements of an automated classification system for precision agriculture applications have already been described by *Shaw and Kelley (2005)*. To create such a classifier, all thresholds used in a decision tree must be invariant against data acquisition dates (e.g. growth stage). Therefore, the use of vegetation indices for a decision tree classifier is critical, because their values change in time. In order to nevertheless make use of these indices, another parameter was created: the deviation of the NDVI from the mean NDVI of the plot. The mean NDVI of the plot was calculated by using a region of interest that was congruent to the plot area. Each pixel NDVI-value of the plot was then subtracted from the mean NDVI. Negative values indicate NDVI-values above the mean and positive ones, NDVI-values below the mean. This parameter has a more constant range over time (range-normalization by the use of the mean NDVI) than the NDVI and does not change the spatial

distribution of the original NDVI characteristics. In our case, this parameter was found to be suitable for the definition of thresholds suitable for all three data collection dates.

In addition, all bands were used for the classification by applying a SMA method, particularly the mixture tuned matched filtering algorithm (MTMF), which is described in chapter 4.2.1. MTMF results are suitable for the definition of decision tree thresholds as two scaled parameters (MF-fraction and infeasibility) are adaptable to indicate a class.

A spectral library was created for each date including the endmembers ‘infected wheat’ and ‘healthy wheat’, by extracting this information from image-pixels. Five ground truth sample points, showing apparent characteristics for each endmember were therefore chosen in the image. For the endmember ‘infected wheat’, only sample points with total disease severity above 20% (percentage of infected leaf area) were selected, in order to achieve a representative spectral signature of this endmember. The four adjacent pixels around the five sample points were considered and averaged (20 pixels for each endmember per image) for the spectral library.

A decision tree was built to classify the data into four classes (Figure 5.1). For the definition of thresholds used in the decision tree, the data from each collection date were empirically investigated by the use of the ‘n-dimensional visualizer’ in ENVI. The facts that the MTMF results have scaled values (giving the relative degree of match to the reference spectrum) and that the NDVI parameter used is temporally more robust than the original NDVI, allow for the averaging of thresholds from different dates. Although the use of optimal decision tree thresholds for each date would probably result in higher classification rates, the use of a decision tree that is suitable for various dates is preferable in multitemporal analyses. Thus, the defined thresholds of all three dates of each decision were averaged. These mean thresholds, which are shown in Figure 5.1, were used in the decision tree to classify the data. The first class represented wheat that is severely infected by pathogens or areas with low vegetation cover. Several studies revealed that the NDVI is an adequate indicator for LAI and biomass (*Huete et al. 1999*). To separate severely infected crop areas or areas with low amount of biomass/LAI, the mentioned NDVI parameter was used. The separation of healthy wheat areas and the classification of the residual pixels in different disease severity classes were achieved by the use of

the MTMF results of the endmember ‘healthy wheat’ and ‘infected wheat’. The results are images with four classes of disease severity. In order to obtain smooth areas by removing single separated pixels, a majority analysis with a 5x5 kernel was applied to the classification result.

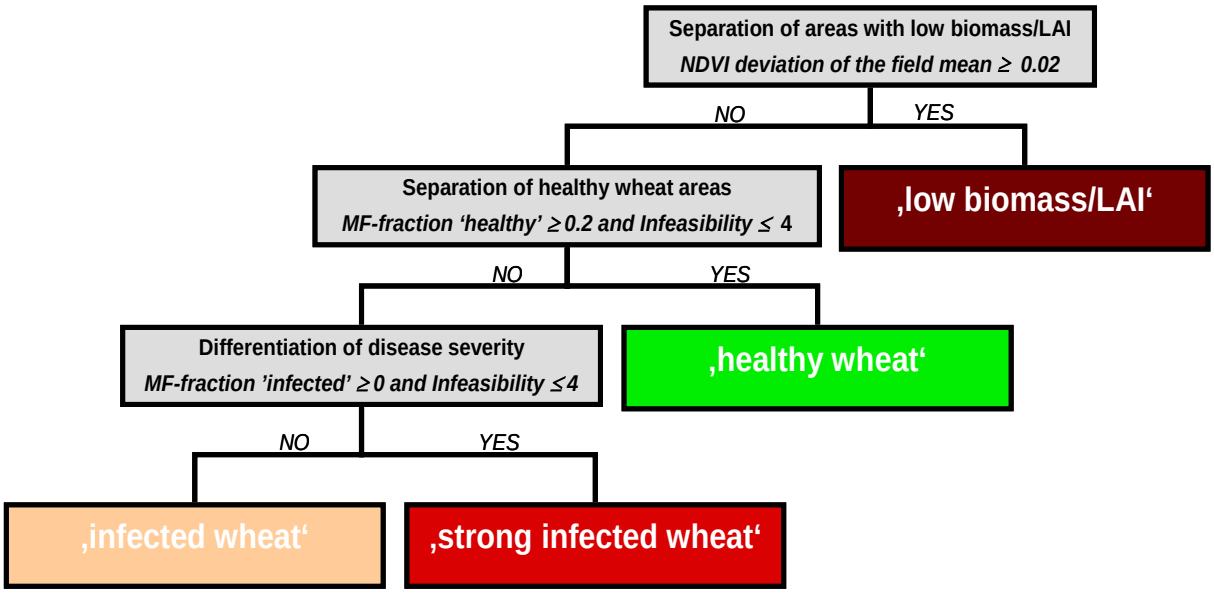

Figure 5.1: DECISION TREE for QuickBird data classification of fungal disease severity of wheat

5.3 Results

An example of the MTMF result of 20 June 2005 is shown in figure 5.2. The matched filtering fraction image of the endmember ‘wheat healthy’ that was calculated with QuickBird data allowed a clear discrimination of healthy and less healthy crops. Brighter pixels indicate areas with healthy wheat crops, darker ones indicate areas dominated by other unknown endmembers (in this case: soil and infected crop areas). Obvious are the lanes of the tractor that are dominated by soil/less biomass.

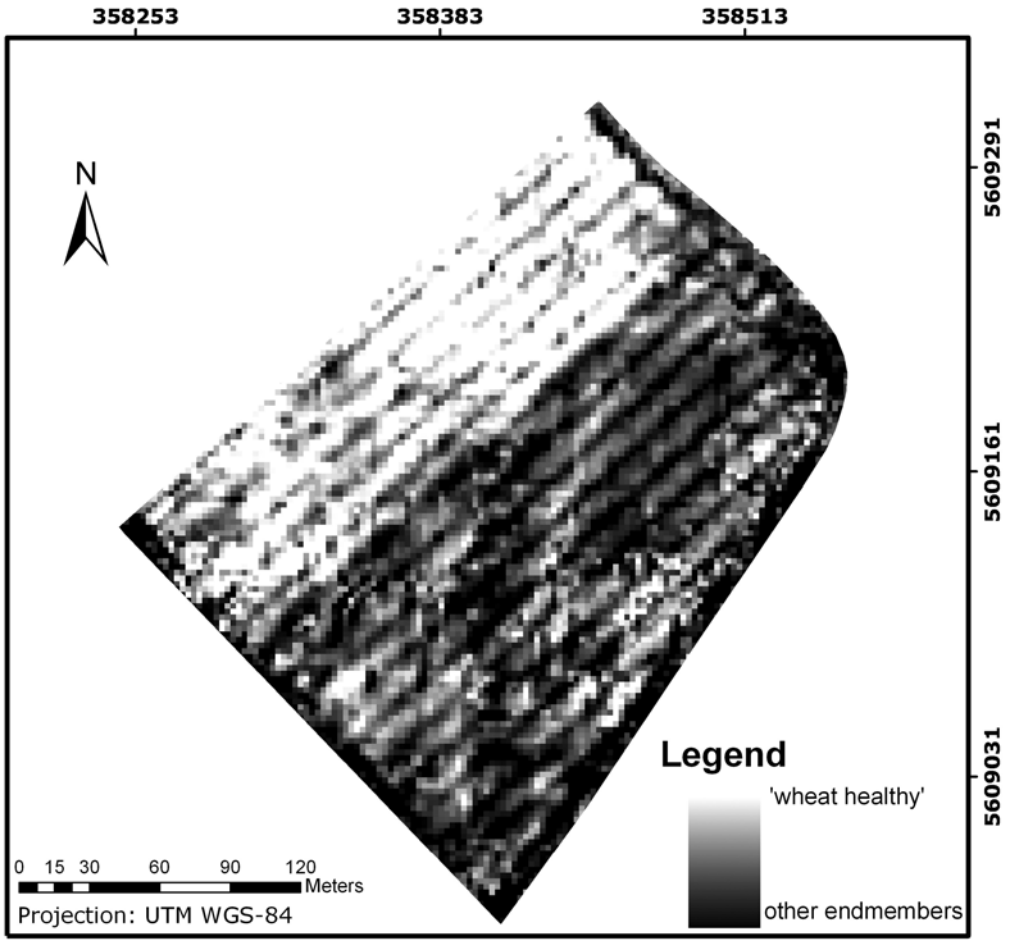

Figure 5.2: MATCHED FILTERING (MF)-FRACTION IMAGE of the endmember 'wheat healthy' of 20 June 2005

Figure 5.3 depicts the classification of the QuickBird image from 22 April 2005, with 4 classes of wheat disease severity. At this time, no fungicide treatment had yet been applied and fungal infections of the wheat crop were detected for relative small areas spread over the entire plot. In-field observations revealed only slight powdery mildew infections with a percentage of infected leaf area between 0-18%. A few plants with higher rates up to 40% were observed. No leaf rust infection was observed in the field at this early growth stage. However, aside from the dominant class, 'healthy wheat', image classification revealed large infected areas, which indicates an overestimation of disease severity by image classification for this date.

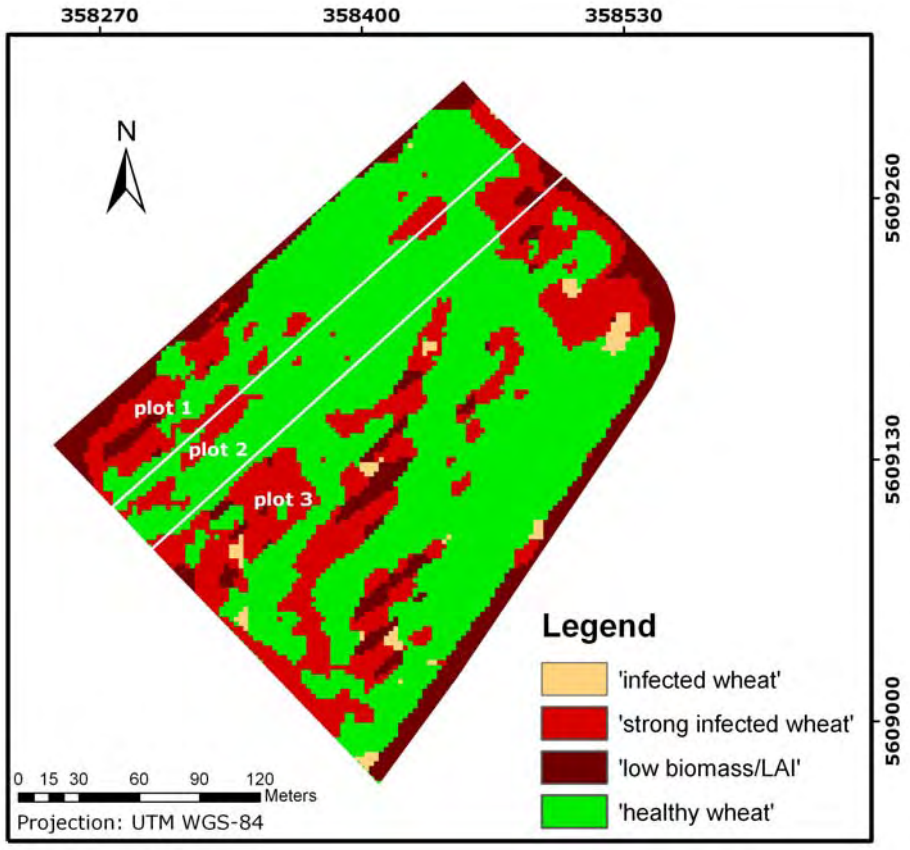

Figure 5.3: IMAGE CLASSIFICATION RESULT OF 22 APRIL 2005 with 4 classes of different wheat disease severity. The three sub areas of different fungicide treatments are displayed as well

Seventeen days after the first fungicide treatment, data classification from 28 May 2005 (Figure 5.4) revealed increased disease severity with predominant areas of the class ‘infected wheat’ and ‘strongly infected wheat’, even in some parts of the fungicide treated plot 1. Obviously, infected crop areas that had already been detected on 22 April 2005, further expanded by 28 May 2005. On this date, ground observations showed only slight leaf rust and stronger powdery mildew infections of crops, with total severity for both pathogens up to 53% infected leaf area in some areas.

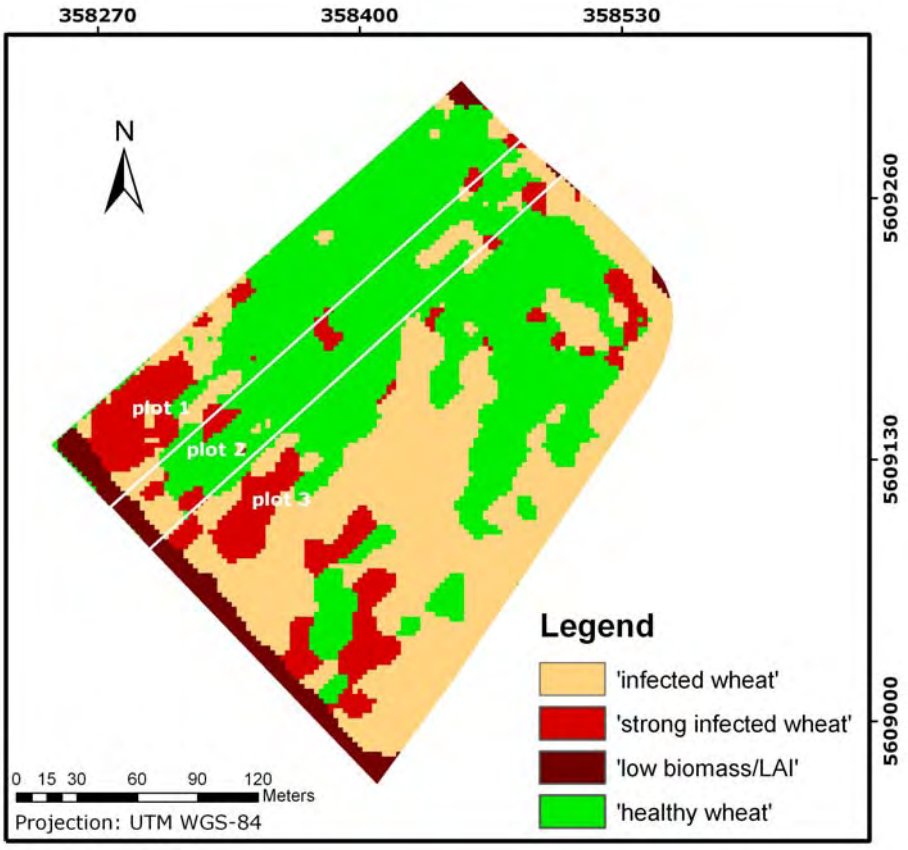

Figure 5.4: IMAGE CLASSIFICATION RESULT OF 28 MAY 2005 with 4 classes of different wheat disease severity. The three sub areas of different fungicide treatments are displayed as well

The classification result of 20 June 2005 (figure 5.5) displayed a strong crop infection in plot 3 and mostly healthy crop areas in plot 1 (treated twice with fungicides) as well as in plot 2 (treated once with fungicides). This indicates the success of the fungicide applications. The clear discrimination between fungicide-untreated and treated plots, i.e. infected and non-infected plots, was observed in the field in almost the same manner. On this date, powdery mildew showed infection rates up to 15% infected leaf area, whereas leaf rust infection was strongly predominant, with infection rates up to 70% infected leaf area.

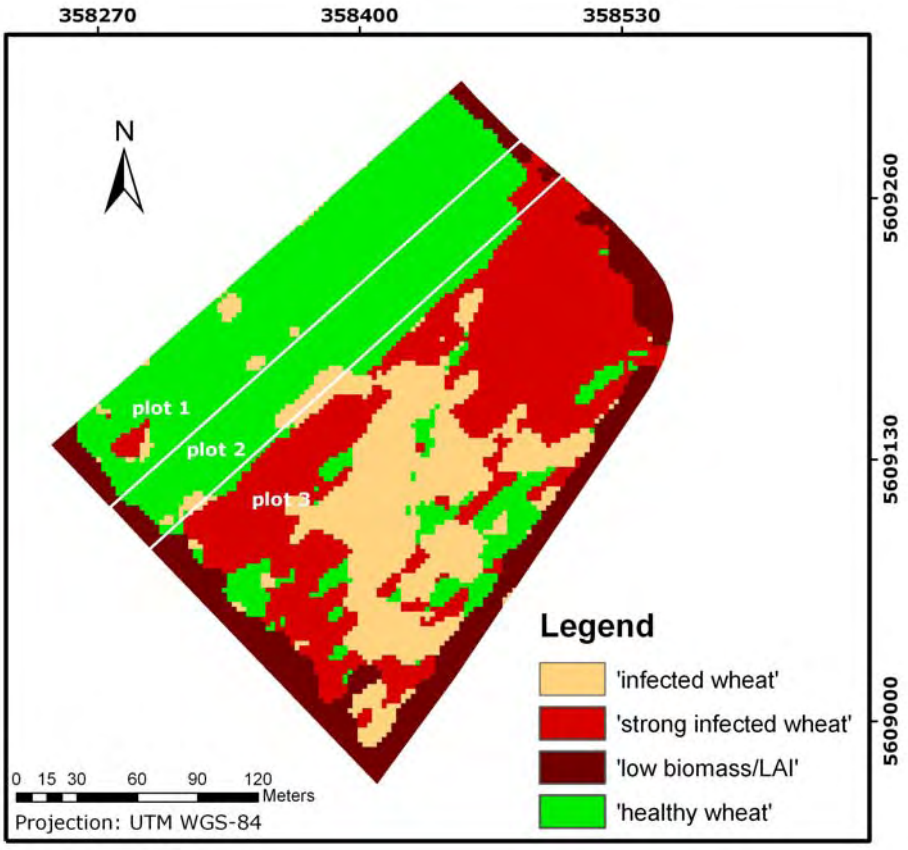

Figure 5.5: IMAGE CLASSIFICATION RESULT OF 20 JUNE 2005 with 4 classes of different wheat disease severity. The three sub areas of different fungicide treatments are displayed as well

The optimal date for fungicide applications in respect of their effectiveness is a crucial and restrictive factor because fungicide applications are limited to crop growth and infection stages, and depend on crop resistance and other external factors such as meteorological parameters (*Moschini & Pérez 1999, West et al. 2003*). However, to support sensor-based detection of the occurrence of infection for the generation of fungicide application maps, only a binary decision for each pixel is required, whether crops are infected or not. Thus, the classes ‘low biomass/LAI’, ‘infected wheat’ and ‘strongly infected wheat’ were combined to obtain images indicating areas of healthy and infected wheat. To assess the accuracy of the classification, the remaining 44 ground truth sample points were used (10 sample points were used for each date as training samples to build the spectral library). To discriminate ground truth sample points affected by pathogens from those without infection, an in-field observed total disease severity threshold of 10% (percentage of infected leaf area) was employed.

This threshold was determined because crops with estimated total infection rates below 10% affected leaf area showed negligible symptoms, which were only detected through intensive inspection. Ground truth sample points were thus classified in two classes as well, in order to compare them with remote sensing classification results.

The classification accuracy is displayed in Table 5.1. For the first data collection date, an overall classification accuracy of only 56.8% was achieved. In particular, the 37.5% of sample points wrongly classified as 'infected' was unsatisfactory, because actually infected crops were classified as 'healthy' and thus these crop areas would not be considered for possible fungicide treatments. Higher classification accuracy was achieved for the scene taken on 28 May 2005. The classification of this date showed an accuracy of 76.5% of correctly classified 'infected' sample points and an overall accuracy of 65.9%. Actual infected sample points were wrongly classified in 23.5% of cases. Highest classification accuracies were achieved on the 20 June 2005, when 96.2% of infected sample points were correctly classified and the overall accuracy of correct classifications was 88.6%. Only 3.8% of the actually infected sample points were classified incorrectly. Due to the subjective estimation of the disease severity in the field and the use of thresholds for data classification, these accuracies had higher or lower values than the actual accuracies.

Table 5.1: CLASSIFICATION ACCURACIES of the remote sensing imagery (relating to ground truth sample points)

classified sample points / date	04/22/2005	05/28/2005	06/20/2005
correctly classified 'healthy' sample points	55.6 %	59.3 %	77.8 %
correctly classified ,infected' sample points	62.5 %	76.5 %	96.2 %
wrongly classified 'healthy' sample points	44.4 %	40.7 %	22.2 %
wrongly classified ,infected' sample points	37.5 %	23.5 %	3.8 %
overall accuracy (correctly classified)	56.8 %	65.9 %	88.6 %

5.4 Discussion and conclusion

The results presented in this chapter demonstrate that multispectral data with high spatial resolution are suitable to detect in-field heterogeneities in wheat vigour, particularly if the crop is strongly affected by fungal infections. It was demonstrated that these data can be effectively used to control the success of fungicide treatments. Particularly at later growth stages, satisfactory classification accuracies were achieved. However, multispectral remote sensing data have a low spectral sensitivity to detect initial infection stages, particularly when only lower leaves are infected. Hence, disease detection with these data at initial infection stages of powdery mildew, which occurs at early growth stages of the plant, is critical. Since fungicides are often applied twice per growing season (according to the development of an infection), a remote sensing-based mapping of disease occurrence at later growth stages, when a second application is required, might be suitable. These data seem to be more useful for the detection of leaf rust which, in this case, occurred late in the growing season with high infection growth rates affecting the whole canopy rapidly.

Although the input of remote sensing to support application management decisions may play an important role, the effectiveness of remote sensing-based application maps have to be investigated in greater detail. *West et al. (2002)* already emphasized the potential of optical sensing and mapping to optimize fungicide applications against fungal diseases, but also mentioned that optically derived disease maps will underestimate disease patch size and latent infections will thus result in secondary infection areas. Therefore, it is useful to model disease spread, which requires knowledge of the spatiotemporal dynamics of each pathogen, in order to define buffer zones around detected patches that would improve the accuracy of disease maps. In comparison to the multispectral data used, hyperspectral remote sensing data may improve the identification rate as they have a higher spectral resolution, which is analysed in chapter 7.

Spatially high-resolution multispectral remote sensing data hold the potential for multitemporal monitoring of fungal wheat diseases, though they are only moderately suitable for early detection, due to the high misclassification rate observed in this study at early growth stages, when fungicide applications are feasible. Even though some areas of reduced crop vitality were detected at early growth stages, the

classification accuracy was too low to generate fungicide application maps. However, at later growth stages and/or higher infection rates, the use of multispectral remote sensing data for the detection of infections yielded positive results. This indicates the suitability of these data for the detection of diseases with late occurrence and/or high infection growth rates. The low temporal resolution of current spatially high-resolved sensor systems is a restrictive factor for practical implementation. The launch of future observation systems with improved repetition rates can open up a wider field of application.

Chapter 6

Identification of site-specific crop growth anomalies using simulated endmembers for spectral mixture analyses

6.1 Introduction

In chapter 5 it was demonstrated that recent sensor systems with a high spatial resolution allow for site-specific identification of stress-caused anomalies of crop vigour. In general, remote sensing methods are required that extract the desired information accurately and quickly. In chapter 5, the suitability of spectral mixture analyses (SMA) for the quantification of crop stress severity was demonstrated. Usually, to obtain spectral endmembers for reference, image pixels or spectroradiometer measurements of objects with apparent spectral characteristics are used. These methods require ground truth information, whose collection is often time and cost-intensive or in some cases even not possible. Thus, the use of endmembers that are independent from any ground truth information is preferable. There are typical spectral responses of plants to stress impact. This knowledge can be used to simulate endmembers that represent stress affected crop canopies.

In this analysis, stress-dependent changes of the reflection rates of vegetation were quantified and the potential of simulated endmembers for spectral mixture analyses was tested, in order to remotely detect several crop stresses or crop growth anomalies of cereal fields with multispectral QuickBird data that have a high spatial resolution.

6.2 Methodology

In 2002 and 2005, several field experiments concerning stress monitoring in cereals were conducted on two experimental farms of the University of Bonn. The stress factors nitrogen deficiency, fungal infection, soil condition and weed infestation were considered. Both study areas have a flat morphology that avoids complicated

interpretation of remote sensing data caused by heterogeneous topography. The field sizes vary between 2 and 9 ha. As shown in table 6.1, four different fields (plots a-d) were considered for a comparison between averaged spectral signatures of entire fields and signatures of areas that contain stressed crops. In another two fields (plots e, f), the detection method was proved, in order to identify areas of crop growth anomalies.

6.2.1 Study sites

In 2002, a field with winter wheat (plot a) that was partly treated with reduced nitrogen rates and a field plot, which in some parts was never treated with fungicides (plot b) were observed. Thus, in each field heterogeneous crop growth appeared; in the first case, due to different nitrogen treatment and in the other case, due to the appearance of powdery mildew and leaf rust. Ground truth data such as biomass, leaf nitrogen level and pathogen infestation rates were collected over the growing season.

In addition, to investigate the effect of weed infestations on the spectral signature of wheat, a field showing weed patches was investigated in 2005 (plot c). Anomalies of barley growth caused by very heterogeneous soil conditions were investigated in another field (plot d). Potential stress due to soil condition was indicated by EM38 measurements of the apparent electrical conductivity (ECa) (Geonics Limited, Ontario, Canada). The values of the EM38 measurements of the investigated field plots varied between 4 and 21 mS m^{-1} thus indicating sandy and loamy soils. The lower field capacity of the areas with sandy soils resulted in lower crop growth and thus in lower yield that was mapped by a combine-mounted yield-mapping system. These heterogeneities of crop growth were investigated in greater detail by the use of remote sensing data and their spectral signatures were compared.

Plot e, showing similar soil stress conditions, and a plot showing different fungal infection rates (plot f) were used to prove the stress detection method. A description of location, treatments and conditions of plot f can be found in chapter 1.6.

Table 6.1: OVERVIEW OF FIELD EXPERIMENTS used in this analysis

Experimental plot	*Stress type*	*use*
Plot a	Nitrogen deficiency	Training data
Plot b	Fungal infection	Training data
Plot c	Weed infestation	Training data
Plot d	Unfavourable soil condition	Training data
Plot e	Unfavourable soil condition	Classification/evaluation
Plot f	Fungal infection	Classification/evaluation

Remote Sensing data from the spatially high-resolution multispectral QuickBird sensor were acquired in June 2002 and in June 2005 for both study areas. The atmospheric corrections of the QuickBird images were done using the ATCOR3 software from Erdas Imagine (GEOSYSTEMS GmbH, Germering, Germany). The validation of the atmospheric corrections was performed against in-situ measurements obtained with a spectroradiometer. For the geometric image correction, the ENVI 4.2 software (Research Systems Inc., Boulder, CO, USA) was used.

6.2.2 Endmember simulation and data processing

A SMA allows a quantification of disease severity at subpixel level. A SMA relies on a spectral library containing all spectral signatures of each endmember, which appear in the pixel spectrum (*Adams et al. 1985*). As opposed to the classical SMA, matched filtering (MF) needs only one endmember in the spectral library. The Matched Filtering is a similar SMA method as the Mixture Tuned Matched Filtering (MTMF), but no infeasibility image is provided.

In order to generate required reference spectra synthetically, a closer examination of the effect of stress impact on plant physiology is necessary, i.e. how does stress affect the reflection of crop canopies. These effects were already investigated in previous studies, e.g. *Lorenzen & Jensen (1989)* and were also described in chapter 2. In summary, stress affected plants are predominantly characterized by a reduction of the reflection rates in the NIR spectrum and less systematically by changes in the VIS.

The fundamental idea of endmember simulation is on the one hand based on the knowledge of typical spectral responses of plants to stress that could be used to modify spectral signatures of unstressed crop areas. On the other hand, in most cases stress factors only occur in some parts of fields. These site-specific heterogeneities allow for the use of mean spectral signatures of whole fields as a basis for simulated endmembers. Thus, spectral signatures can be derived from image-pixels that are used to simulate endmembers of stressed vegetation under consideration of the knowledge of typical stress-induced changes of plants spectral characteristics. However, this simulation requires a quantification of known stress-dependent changes of the reflection rates. Therefore, the spectral signatures of crop areas affected by different stress factors such as nitrogen deficiency, fungal infection, soil condition and weed infestation, were compared to the mean spectral signature of the whole corresponding field.

6.3 Results

The remote sensing data, covering the four field experiments (plot a-d) that address these different stress factors, were analysed (table 6.1). For example, Figure 6.1 shows spectral signatures of a fungal infected wheat area and the mean spectral signature of the corresponding field as derived from QuickBird data.

In all cases, only slight changes of the reflection in the blue and green spectrum were ascertained, whereas a considerable increase of the red reflection was obvious. A reduction of the NIR reflection from 4.8% up to 21.4% was predominant. This comparison showed that different stresses cause different spectral signatures (table 6.2).

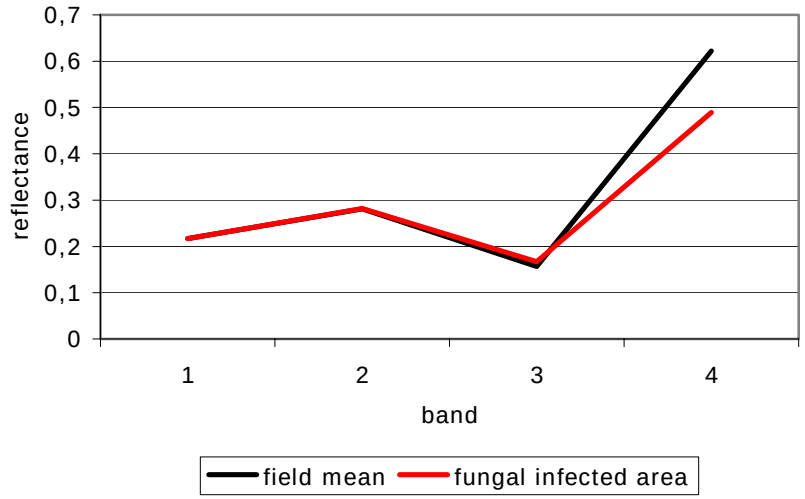

Figure 6.1: SPECTRAL SIGNATURE OF A FUNGAL INFECTED WHEAT AREA AND THE MEAN SPECTRAL SIGNATURE OF THE CORRESPONDING FIELD as derived from QuickBird images

With the use of this knowledge, the mean spectral signatures of two fields (plots e and f), (where anomalies of crop vigour caused by the stress factors soil condition and fungal infection were observed), were modified to generate endmembers for the SMA. Therefore, the observed mean difference of the reflection rates (table 6.2) were used as examples for general stress detection, i.e. the mean spectral signatures of plot e and f were reduced by 5% in the red and by 9% in the NIR band.

Table 6.2: PERCENTAGE DEVIATION (BAND-WISE) OF REFLECTANCE VALUES OF STRESS AFFECTED AREAS FROM THE CORRESPONDING FIELD MEAN for different stressors in cereals

QuickBird band	*Fungal infection*	*Nitrogen deficiency*	*unfavourable soil condition*	*Weed infestation*	*mean*
1	0.0	1.8	-0.6	4.8	1.5
2	0.4	6.3	-1.4	0.0	1.3
3	6.4	10.9	-1.1	5.0	5.3
4	-21.4	-6.3	-4.8	-4.8	-9.3

For a more precise detection of a specific stress, the specific band-wise difference values that are given in table 6.2 would be more suitable. Hence, simulated endmembers representing stress affected wheat areas were generated and used as reference (MNF transformed) for the MF, in order to identify areas with crop growth anomalies without the use of any ground truth data. Ground truth was only used to validate the results of this approach.

Figure 6.2 displays the result of the matched filtering using the simulated endmember 'stress affected barley' as well as the EM38- measured ECa (mS m^{-1}) of plot e. Brighter pixels in the MF-fraction image indicate areas with good match to the reference spectrum (in this case to the simulated endmember). A comparison between the spatial distribution of the measured ECa values (contours) and the MF result demonstrate a good agreement. ECa values less than 15 mS m^{-1} indicate areas of sandy soils, which have a reduced field capacity (*Neudecker et al. 2001*). Thus, in these areas barley growth anomalies occurred that resulted in lower yield. The proposed remote sensing-based detection method using simulated endmember achieved an appropriate identification of these stress affected crop areas.

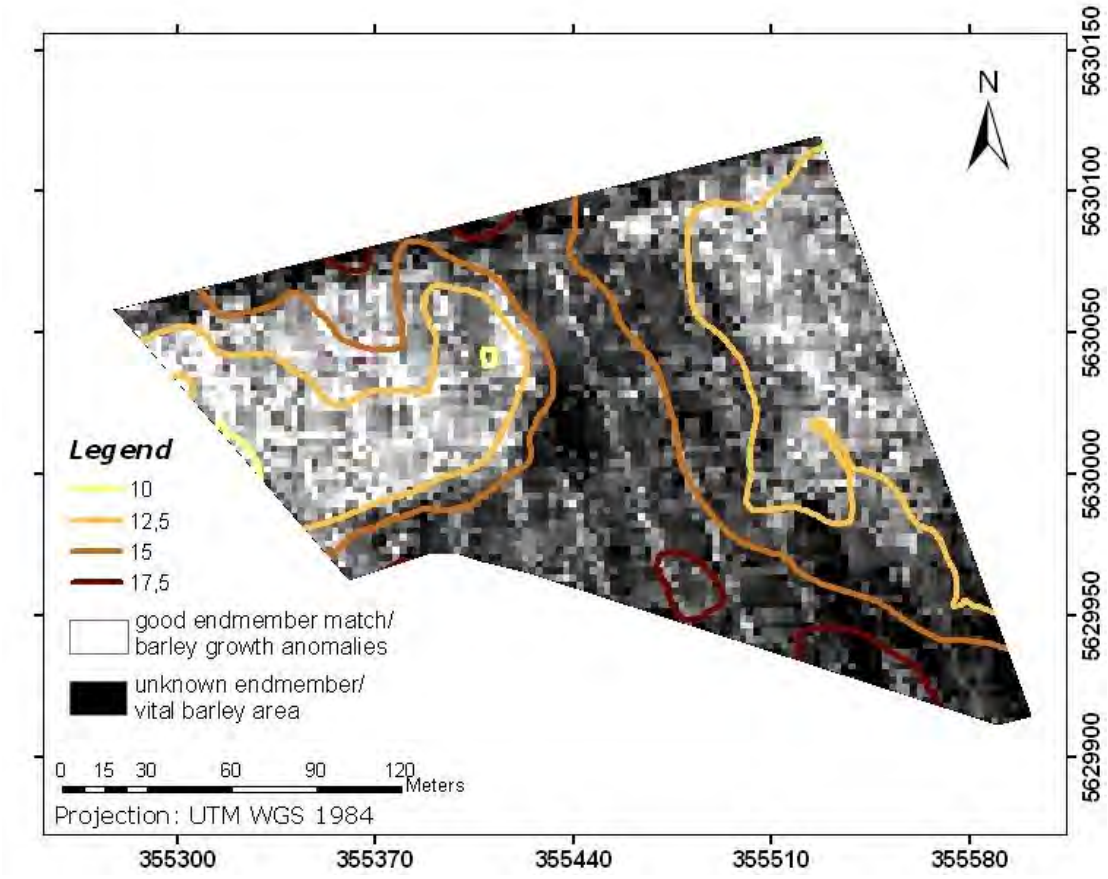

Figure 6.2: MATCHED FRACTION IMAGE OF THE SIMULATED ENDMEMBER 'STRESS AFFECTED BARLEY' with the EM38- measured apparent electrical conductivity (mS m^{-1}) of plot e

In plot f, where in some parts no fungicides were applied (plot f-3; south-eastern part), a strong fungal infection of the wheat occurred. Figure 6.3 shows the result of the matched filtering using simulated endmember (MF-fraction image) and figure 6.4 displays the interpolated disease severity map (ground truth). A visual comparison of the image and the map indicate a satisfactory agreement between stress affected and vital wheat areas. In order to validate the results, a correlation analysis between MF-results and in-field collected disease severity data (percentage of infected leaf area) was applied. Therefore, around each sample point (50 points), a buffer of 4m was applied and the mean of these parameters was calculated. The correlation between MF-fraction values and disease severity showed a positive correlation with a Pearson correlation coefficient of $r = 0.69$.

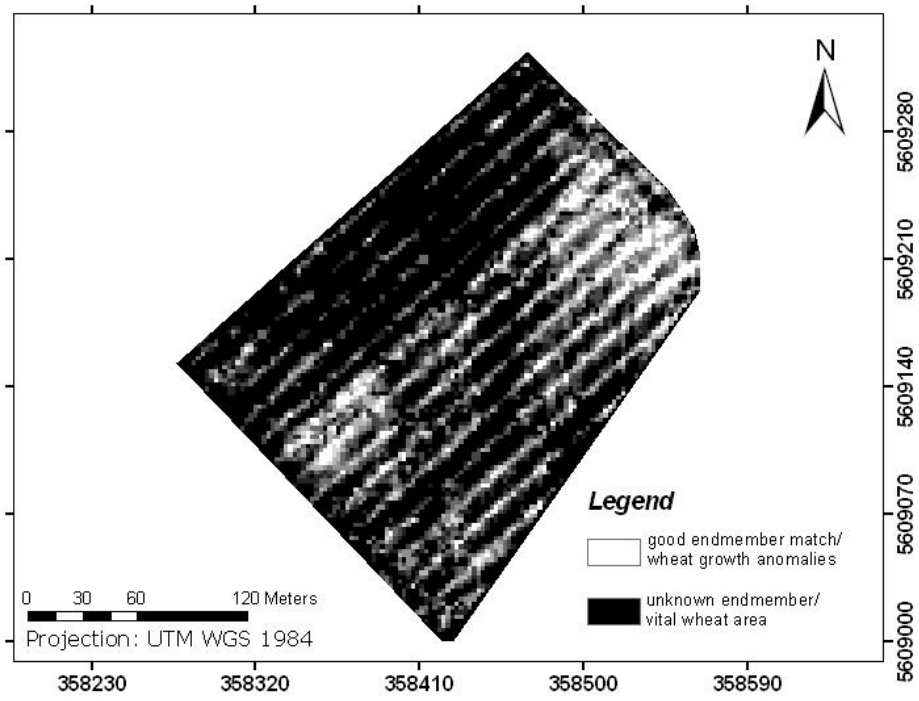

Figure 6.3: MATCHED FRACTION IMAGE OF THE ENDMEMBER 'STRESS AFFECTED WHEAT' of plot f

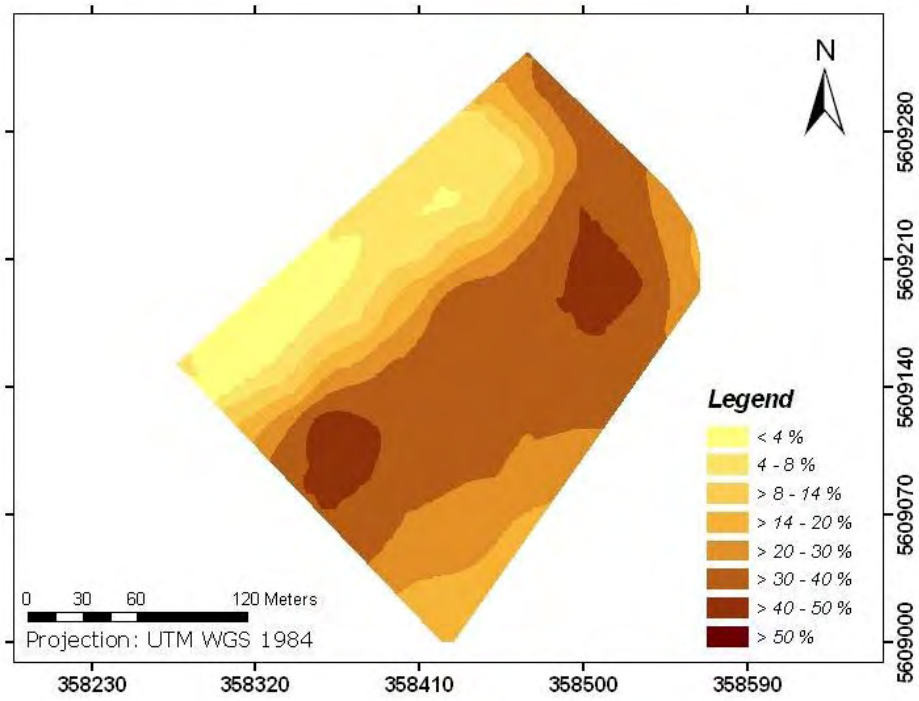

Figure 6.4: DISEASE SEVERITY MAP (interpolated infected leaf area in %) as observed in field plot f

In order to validate the benefit of this ground-truth independent SMA method, its results were compared with the NDVI that constitutes the most often used indicator of vegetation conditions. The correlation between NDVI values and disease severity for plot f showed a negative correlation of $r = -0.68$ and thus showed similar results as the presented SMA method ($r = 0.69$). However, the correlation between the NDVI values and the MF-values showed only $r = -0.46$. That means that the NDVI and the SMA are generally both suitable to detect unspecific stress areas, but do not give congruent information. Hence, a synergistic use of both methods probably achieves the best stress detection result. Besides the fact that the MF-method presented here showed a slight higher correlation coefficient (even with the applied endmember modifications of the more general mean differences), the advantage of the method is that simulated endmembers are adjustable to the stress that should be detected. In contrast, the NDVI is not modifiable. Thus, given an optimal stress-dependent modification of mean field spectral signatures - for example with the given differences showed in table 6.2 - a more specifically stress detection is possible.

6.4 Discussion and conclusion

The proposed SMA method using simulated endmembers is suitable to identify areas of site-specific crop growth anomalies. The detection accuracy could be improved by the use of optimal stress-dependent modification rates for simulated endmembers. However, in the present study, even averaged modification rates achieved satisfactory results. Observed changes of reflection rates depended on the degree of stress impact on the observation date, which in some cases (e.g. fungal infections) is a dynamic process.

The use of averaged spectral signatures of whole fields as a basis for the simulation of endmembers is on the one hand beneficial, since no ground truth is required to generate adequate endmembers. On the other hand, this could affect the result of the SMA adversely; in some cases, for instance if the field heterogeneity of crop growth is exceptionally high, extremely stress affected areas would not be identified, because the simulated endmember (based on the field mean) would not represent these areas sufficiently. In cases of homogeneous crop growth, only tractor lanes would be identified, due to lower vegetation covers.

The proposed method using simulated endmembers for SMA is a suitable tool to quantify stress impact. The knowledge-based simulated endmembers represented spectral signatures of areas with a reduced crop vigour sufficiently. These endmembers, which constitute modified mean spectral signatures of fields - under consideration of typical changes of reflection rates of stressed crops - allow for a ground truth-independent detection of areas that require adjusted management actions. This approach showed to be more effective than NDVI-analyses and can be alternatively and/or synergistically used.

Chapter 7

The potential of airborne hyperspectral and multispectral remote sensing data for the identification of powdery mildew in wheat

7.1 Introduction

Previous studies presented here primarily focussed on the temporal dimension of crop diseases and their sensor-based detection as described in chapter 1.5. In context of a detection of these phenomena, however, the temporal dimension depends on the spectral resolution of the used data because improved spectral resolutions may result in earlier detection of crop stress. In chapter 5 it was demonstrated that multispectral data is not suitable for early detection of crop diseases due to their low spectral resolution. In contrast to multispectral sensors, which record reflected radiance in broad spectral bands, hyperspectral sensors are able to collect data in various spectrally narrow and continuous bands. This allows – in addition to a differentiation of photosynthetic active and non-active material – for a more detailed analysis of the phenological stage and the condition of vegetation (*Moran et al. 1997*). By the use of hyperspectral data, recent studies even focussed on the discrimination of different stress factors in plants (*Moshou et al. 2006*). *Estep & Davis (2000)* also emphasized the advantage of hyperspectral data for agricultural applications. This final chapter constitutes an outlook on the next period of the Research Training Group, when the main focus will be the spectral dimension of remote sensing data used for crop stress detection (see figure 1.5).

The preliminary analysis was carried out, in order to (i) compare the potential of hyperspectral and multispectral remote sensing data for quantification of powdery mildew severity in wheat; (ii) to test an approach that derives appropriate endmembers from image data and (iii) to approve the suitability of modelled endmembers for a detection of disease severity by a SMA of image data.

7.2 Methodology

The investigated wheat field was the one described in chapter 1.6. Remote sensing data were acquired by the airborne hyperspectral Mapper (HyMap) on 28 May 2005 (BBCH 45). In order to compare multi- and hyperspectral data, HyMap data was resampled to the spectral characteristics of the multispectral QuickBird sensor as described in the special chapter presented in the appendix. Data characteristics of both data types thus were identical (apart the spectral characteristics), which allows for a direct comparison of the potential of each data type for early detection of powdery mildew.
Information of the disease severity collected at the 54 sample points in field were used to validate the results. On 28 May 2005, powdery mildew constituted the predominant stress, whereas only marginal leaf rust infections occurred at some sample points (figure 3.5).

7.2.1 Endmember selection

The quality of SMA results, in general, highly depends on the availability of representative endmembers (*Tompkins et al. 1997*). Endmembers used in SMA can either be derived from image pixels or from a spectral library that contains reference endmembers derived from measurements taken in field, in laboratory, from radiative transfer models or derived from other images. Several approaches for the selection of optimal/representative endmembers were developed in the past. For instance, *Bateson & Curtiss (1996)* presented a manual selection approach (a similar approach was used in the study presented in chapter 5), *Boardman et al. (1995)* developed the Pixel Purity Index (PPI). In addition, the Count-based Endmember Selection (CoB) (*Roberts et al. 2003*), the Endmember Average RMSE (EAR) (*Dennison & Roberts 2003*) and the Minimum Average Spectral Angle (MASA) (*Dennison et al. 2004*) were presented in the past. In contrast to the PPI, these approaches require knowledge about the spectrum characteristics to assign each spectrum to a certain class. The CoB indicates optimal endmembers of a spectral library that model the greatest number of spectra within a class. Endmembers are assessed by whether they meet fraction, RMSE and residual constraints when any other spectrum in the library is unmixed (*Roberts et al. 2003*). The CoB provides several quality parameters that allow for a ranking of representative endmembers. The in-CoB parameter gives the

total number of spectra modelled within the class, the out-CoB gives the total number of models outside of the class and the Count-Based Index (CoBI), developed by *Clarke et al. (2005)*, represents the ratio of in-CoB to out-CoB with the denominator multiplied by the number of spectra within a class. A high CoBI and a high in-CoB represent an excellent choice (*Roberts et al. 2007*).

The EAR calculates the average RMSE produced by a spectrum when it is used to model all other members of a class. The optimum spectrum produces the lowest average RMSE (*Roberts et al. 2007*).

The MASA calculates the average spectral angle between the reference spectrum (candidate model) and all other spectra within the same class. The best endmember is selected as the one that produces the lowest average spectral angle (*Dennison et al. 2004*).

The approaches CoB, EAR and MASA that identify optimal/representative endmembers are implemented in the software 'VIPER tools', developed at the Department of Geography of the University California Santa Barbara (www.vipertools.org). The free software package 'VIPER tools' is an ENVI add-in that provides several processing tools for hyperspectral and multispectral remote sensing data. The major components are tools for creating and managing spectral libraries, for the selection of optimal endmembers for SMA and for calculating and interpreting Multiple Endmember Spectral Mixture Analyses (MESMA). For this analysis, the 'Viper tools' were used for the creation of spectral libraries and for the selection of optimal endmembers.

A spectral library was created containing spectra of the 54 pixels where the sample points were located and disease severity data was collected in field. Metadata, in particular powdery mildew severity and the percentage fraction of vegetation cover was linked to each spectrum. Accessorily, in order to categorize the disease severity, which is required for the optimal endmember selection procedure, 4 categories were defined: 'vital wheat' (<10% disease severity), 'low infected wheat' (10 – 20%), 'mid infected wheat' (21 – 30%) and 'strong infected wheat' (>30%). Thus, 34 sample points were defined as representing 'vital wheat', 14 'low infected wheat', 3 'mid infected wheat' and 3 represented 'strong infected wheat'. Afterwards, EAR, MASA and CoB were calculated for each spectrum. Thereby, only one optimal endmember could be selected (pixel of sample point 21) for the category 'vital wheat' that showed

high CoBI- and low EAR and MASA values, whereas no representative endmember could be selected for the other categories.

7.2.2 Pure endmember derivation and SMA

Especially at early infection stages, representative endmembers of infected wheat do not occur in field due to mostly low disease severity rates. As the result of the endmember selection showed, optimal endmember could only be found for healthy wheat. Therefore, to derive pure endmember the method of a linear spectral unmixing of spectra – as described in chapter 2 – was applied to image data. A pixel spectrum of a sample point with high powdery mildew severity (30%) and similar vegetation fraction as sample point 21 was chosen (sample point 53). The selected endmember representing vital wheat was spectrally unmixed of its soil fraction (using a pure soil spectrum) and used for a spectral unmixing of the pixel spectrum at sample point 53. The results were pure endmember of healthy wheat and 100% powdery mildew infected wheat (shade fraction was not considered). These pure endmembers were used for a SMA of the hyperspectral and simulated multispectral data, whereas for the multispectral data the same pure endmember derivation procedure was applied (using the multispectral pixel spectra of the same sample points).

The Multiple Endmember Spectral Mixture Analysis (MESMA) of the ‘VIPER tools’ was not used, due to the fact that only single endmembers were used for the SMA. Therefore, the Mixture Tuned Matched Filtering (MTMF) was applied to estimate fractions of endmembers ‘healthy wheat’, ‘completely infected wheat’ and ‘soil’ in the image pixels. A regression analysis between the MF-fractions of each endmember and the in-field observed disease severity at the sample points was afterwards applied. All processing steps were carried out for hyperspectral and multispectral data.

7.3 Results

Figure 7.1 displays the three hyperspectral pure endmembers used for the SMA. Whereas the soil spectra was derived from a pixel in the HyMap image with apparent characteristics, the pure endmembers ‘healthy wheat’ and ‘completely infected wheat’ were spectrally unmixed as described in chapter 2. The modelled pure 100% powdery mildew infected wheat endmember shows typical vegetation features, but as expected a strongly decreased NIR-plateau. Considering plant’s typical physiological response to stress, a higher reflection in the red spectrum would be expected. This modelled endmember is only an approximation and shows some unexpected features. However, no real spectrum that represents 100% infected wheat exists and this endmember is helpful to estimate the disease severity by image data.

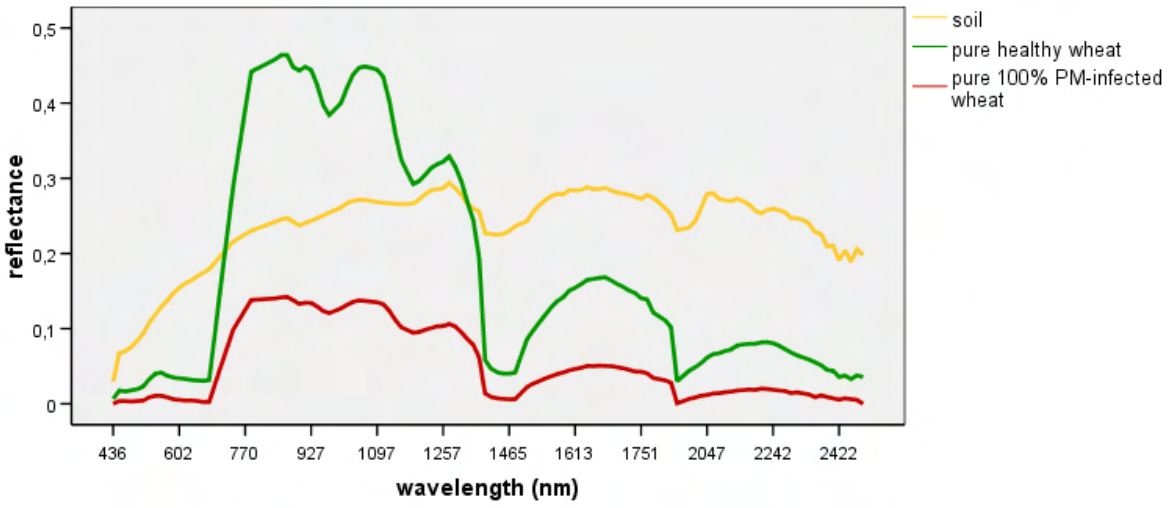

Figure 7.1: SPECTRAL SIGNATURES OF PURE ENDMEMBERS from HyMap as retrieved from image pixels and endmember modelling

The MF-fractions of each endmember in the investigated field plot are displayed in figure 7.2 as a synthetically RGB-image. Red colours indicate high fractions of infected wheat, green gives predominantly healthy wheat fractions and blue represents high soil fractions. Obvious is a large area of infected wheat in plot 3, where no fungicides were applied that corresponds to in-field observations.

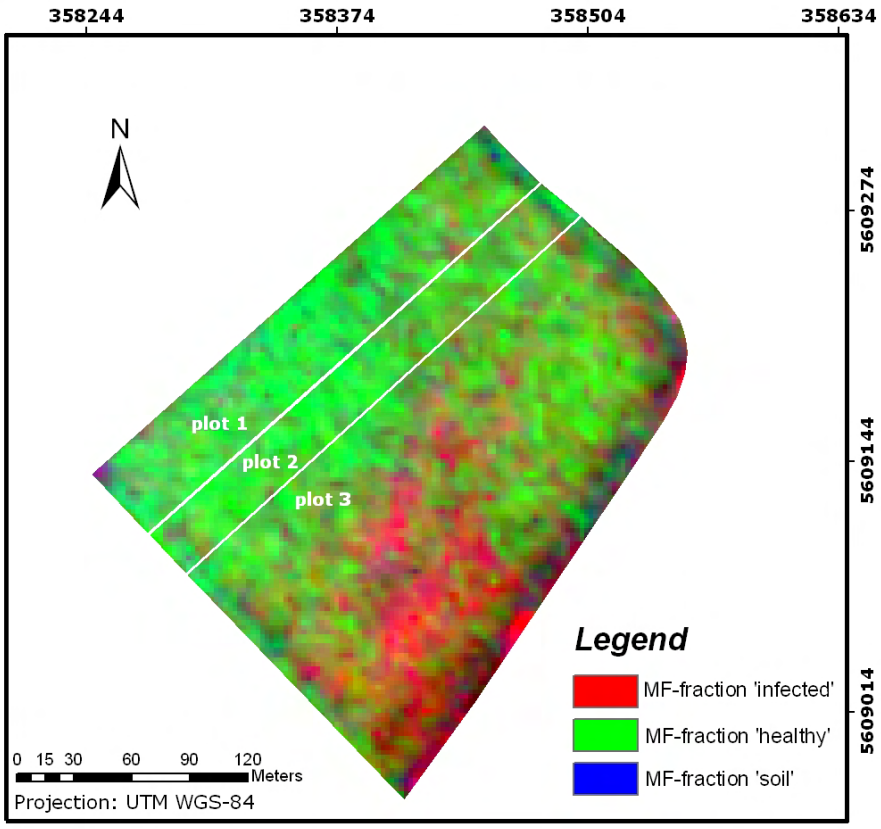

Figure 7.2: IMAGE OF THE FIELD PLOT SHOWING MF-FRACTIONS OF THE ENDMEMBERS 'pure infected wheat' (R), 'pure healthy wheat' (G) and 'soil' (B) as estimated by the MTMF

A correlation analysis between the MF-results and in-field collected powdery mildew severity data (percentage of infected leaf area) was performed to validate the results. Therefore, around each sample point (54 points) a buffer of 4m was applied in a GIS and the mean of pixels intersected by these buffer zones was calculated for each parameter.

Figure 7.3 shows the correlation between disease severity and the MF-fractions of the healthy wheat endmember as estimated by the MTMF for the hyperspectral data. A negative correlation was found with a Pearson correlation coefficient of r = -0.74 and r^2 = 0.55. A positive correlation was found for disease severity and MF-fractions of the modelled powdery mildew infected wheat endmember by r = 0.82 and r^2 = 0.67 (figure 7.4).

In contrast, only a poor correlation was found for multispectral data. The correlation between disease severity and the MF-fractions of the healthy wheat endmember showed a Pearson correlation coefficient of r = -0.15 and a r^2 = 0.02. The Pearson correlation coefficient for the relationship between powdery mildew severity and MF-fractions of the modelled multispectral powdery mildew infected wheat endmember was r = 0.2 and r^2 = 0.04.

Figure 7.3: CORRELATION OF DISEASE SEVERITY AND MF-VALUES OF THE PURE HEALTHY WHEAT ENDMEMBER as estimated by the MTMF for hyperspectral data

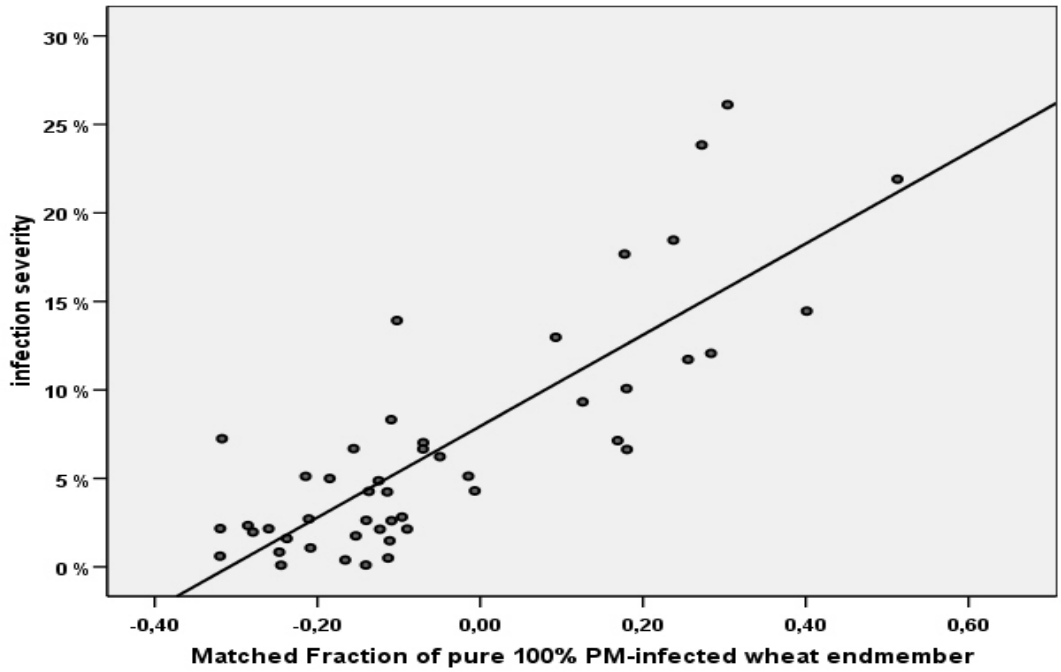

Figure 7.4: CORRELATION OF DISEASE SEVERITY AND MF-VALUES OF THE PURE 100% POWDERY MILDEW INFECTED WHEAT ENDMEMBER as estimated by the MTMF for hyperspectral data

7.4 Discussion and conclusion

This chapter comprises a comparison of multispectral and hyperspectral airborne remote sensing data for a detection of powdery mildew infections in wheat using a SMA. An approach for the selection of optimal/representative endmembers was used, which is implemented in the ENVI add-in software 'VIPER tools'. Thus, an optimal endmember representing healthy wheat could be selected from an image pixel. In addition, the endmember selection process gave information about the potential for early crop stress detection. The fact that no representative endmember for infected wheat could be found indicates that a satisfying early detection of infected wheat is actually not possible using SMA, due to the lack of required endmembers. This is particularly the case for early infection stages when only a few small areas are infected and thus only few pixel spectra of these areas could be considered as possible endmembers. That indicates that a detection of infected wheat areas is only possible via a detection of healthy wheat areas, because other areas than healthy wheat areas could be considered as stress affected. The regression analysis of MF-fractions representing healthy wheat and disease severity

as observed in field showed satisfactory results for hyperspectral data (r = -0.74), which demonstrates the potential for this kind of indirect disease detection.

The most challenging part for a direct plant disease detection using SMA is the derivation of appropriate endmembers. To provide such appropriate endmember representing infected wheat, a linear mixture model was applied to the spectra. An endmember was generated approximately representing a wheat canopy with 100% infected leaf area by unmixing the powdery mildew infected plant fraction of a mixed pixel spectrum. The regression analysis of MF-fractions of the modelled hyperspectral infected wheat endmember and in-field observed disease severity showed even more satisfactory results with a Pearson correlation coefficient of r = 0.82. Hence, using modelled endmembers representing infected wheat for SMA, a direct identification of powdery mildew severity is possible with hyperspectral data.

The results of the SMA of multispectral image data indicated that detections of powdery mildew infections are not possible at this infection stage, neither by the use of the healthy wheat endmember, nor by using the modelled completely infected wheat endmember. This was most likely caused by the unexpected observed low reflectance rates in the modelled red spectrum of the multispectral infected endmember that represented an endmember with inappropriate characteristics.

This analysis revealed a high potential for the detection of powdery mildew infections. The comparison to multispectral data clearly pointed out the advantage of hyperspectral data. Hence, even a detection of this phenomenon at early infection stages seems possible by the use of this data.

Conclusion

Summary

Precision Agriculture essentially contributes to sustainable agricultural management by taking site-specific heterogeneities of crop growth by spatially and temporally adjusted management actions into account, resulting in a declining use of cost-intensive and ecologically harmful agrochemicals. Precision Agriculture, however, requires detailed information about current crop status. Remote sensing has the potential to identify crop growth anomalies due to typical spectral responses of crops to stress factors. In contrast to spatiotemporally relative stable stress factors – such as soil conditions – highly dynamic stress phenomena require monitoring in a high temporal resolution. Only detailed analyses of the spatiotemporal processes of these phenomena provide information about appropriate temporal resolutions of stress detection systems.

Present studies focussed on the potential of multiscale remote sensing techniques for multitemporal detection of two most common and harmful wheat diseases, powdery mildew (*Blumeria graminis*) and leaf rust (*Puccinia recondita*), which cause considerable yield losses (a yield loss of up to 2.2 t ha^{-1} was observed in this analysis). Prerequisites for remote sensing-based multitemporal observations of fungal infections are, first, a profound knowledge about spectral responses of plants to fungal infections and, second, an understanding of the spatiotemporal characteristics of the phenomena.

Chapter 2 focussed on the spectral characteristics of vital and fungal infected wheat at leaf and canopy scale. Systematic differences between the spectra were found in either case. A linear mixture model was applied to canopy spectra, in order to derive a spectrum representing a wheat canopy with 100% disease severity. In a field experiment, the dynamics of powdery mildew and leaf rust were analysed in their spatial and temporal dimension by statistics and geo-statistics. Various statistical parameters were selected to describe and differentiate epidemics. Powdery mildew and leaf rust generally occurred in patches while offering different temporal characteristics. In particular for leaf rust, a more typical progress was observed.

Results indicated critical growth stages when diseases should be controlled (in this particular case, optimal disease control/detection dates were between growth stage BBCH 41 and 45 for both pathogens and additionally BBCH 30 for powdery mildew). It was demonstrated that even a single fungicide application per growing season was sufficient to successfully control leaf rust.

Further analyses (chapters 4-7) addressed sensor-based detection of fungal infected wheat in laboratory and field experiments. In the laboratory, five days after inoculation of wheat plants with *Puccinia recondita*, discrimination between infected and vital stands was achieved by the use of a hyperspectral imaging sensor, whereas satisfactory disease detection by near-range acquired multispectral image data was not possible (chapter 4).

In a field experiment, described in chapter 5, the potential of multispectral remote sensing data with high spatial resolution for multitemporal stress monitoring was assessed using images from April, May and June of the growth period in 2005. Results of spectral mixture analyses (SMA) and a parameter giving site-specific variations of a vegetation index were suitable to identify crop areas with reduced vitality caused by diseases. This data also showed high potential for monitoring the effectiveness of fungicide applications. The higher the disease severity or growth stage, the higher the classification accuracy (April: 56.8%, May: 65.9% and June: 88.6%). However, the required early stress detection was not possible with multispectral remote sensing data.

In another experiment (chapter 6), several cereal fields were monitored by in-field observations and multispectral remote sensing data, in order to assess stress-dependent changes of wheat spectral signatures. It demonstrated that stress factors generally result in typical deviations from field mean spectral signatures, regardless of the stress type (only magnitude of changes varied depending on the stress impact). An approach was developed to generate simulated endmembers without any of the ground truth information usually required for representative endmember derivation. Mean field spectral signatures were thereby modified on the basis of the plant’s known physiological responses to stress. Crop areas showing growth anomalies could thus be successfully identified and quantified.

A comparison of airborne multi- and hyperspectral data with respect to powdery mildew detection was drawn in chapter 7. A sophisticated endmember selection procedure was used, whereby only one representative endmember for healthy wheat could be derived. A linear spectral mixture model was therefore applied to a pixel spectrum with known characteristics, in order to derive an endmember representing 100% powdery mildew infected wheat. Regression analyses of matched fraction estimates of this endmember and in-field observed powdery mildew severity showed promising results for hyperspectral data ($r = 0.82$ and $r^2 = 0.67$). Due to the fact that these results were achieved using data acquired in May, even earlier detection of infections seems possible using hyperspectral data. In contrast, this approach was not suitable for multispectral data ($r = 0.2$ and $r^2 = 0.04$), because modelled spectral signatures showed less representative characteristics.

Discussion

The results of these studies indicate that sensor-based approaches have a high potential for the identification and quantification of fungal diseases and stresses in crops. Nevertheless, some sensors are more suitable than others.

Given an optimal detection date and a spatially sufficient image sampling density, near-range hyperspectral imaging sensors are the most suitable for detecting crop diseases at early stages, which is required for highly effective site-specific fungicide applications. Near-range sensors, particularly imaging sensors, have the advantage of sensing the stress symptoms in greater detail. However, multitemporal stress monitoring is in some cases critical, because even vital canopies show high spectral variability during development (chapter 2). Spectroradiometer measurements as well as multispectral imaging data can be used for a discrimination of infected and vital crop areas, but in this case, an optimal near-range stress detection sensor for multitemporal approaches represented a hyperspectral imaging sensor (chapter 4).

In contrast, spatially high-resolution satellite- or airborne sensing systems allow for identification and mapping of stressed crop areas with total field coverage. Site-specific crop growth anomalies can thus be designated and maps showing areas requiring specific management actions can be derived. Even though high disease detection accuracy for powdery mildew (*Blumeria graminis*) was achieved using hyperspectral HyMap data (chapter 7) and even earlier disease detection seems thus

to be possible, detection of initial infections is not possible. Initial infections occur on single leaves, whereas recent remote sensing systems cover 5.7m^2 per pixel (high-resolution QuickBird sensor). Studies of chapter 6 and 7 showed that multispectral remote sensing data is not suitable for discriminating different stress factors or even pathogens without in-field information, but has a high potential to identify areas of reduced crop vigour or growth anomalies. *Moran et al. (1997)* and *West et al. (2003)* draw similar conclusion.

The results of the present studies lead to the following conclusions: (i) near-range hyperspectral imaging sensors are valuable tools for the detection of initial onset of crop diseases; (ii) airborne- or satellite remote sensing data are suitable to identify general crop stress at advanced stages; (iii) hyperspectral data thereby achieves higher accuracies than multispectral data and (iv) hyperspectral data thus basically allows for early detection of stress factors.

Data processing by SMA generally allowed for a quantification of stress at subpixel level as already mentioned by *Lelong et al. (1998)* and *Du et al. (2004)*. In contrast, vegetation indices are not sensitive to the onset of stress but are useful in evaluating the consequences of stress (*Jackson et al. 1986*) and were thus synergistically used. The quality of a SMA, however, highly depends on the appropriateness of utilized endmembers, which is a limiting factor for each SMA. By the onset of a disease or in cases of sparsely infected crop areas, appropriate endmembers which sufficiently represent infected crops are difficult to derive. Endmember selection procedures showed that only endmembers of vital crops could be found (chapter 7). Identification of stressed crop areas is thus only indirectly possible via detection of vital crop areas. This problem was solved by different approaches. Successful direct estimation of disease severity was achieved for hyperspectral data by modelled endmembers representing completely infected wheat. Another endmember modelling approach for multispectral data was modified spectral signatures of the field mean (chapter 6). Promising SMA results for identifications of unspecific crop stresses could be achieved. In order to map in-field heterogeneities, this approach taking relative deviations of the field mean into consideration, was also suitable for vegetation indices that could then be used for multitemporal classifications (chapter 5). These

approaches can be used for crop stress quantification, in case no ground truth or appropriate endmembers are available.

As the context of Precision Agriculture implies, the main focus of remote sensing approaches for Precision Agriculture applications must be a maximum accuracy of data pre-processing. However, it must be noted that achieved results include some uncertainties due to common inconstancies in multitemporal remote sensing data (such as varying acquisition geometry etc.) and a variance of in-field collected disease severity data. *Parker et al. (1995)* mentioned that there is no standardized method to estimate disease severity and visual estimations thus vary.

In context of Precision Agriculture, the availability of remote sensing data at key times for management actions is a limiting factor, as the temporal resolution of spatially high-resolution data is low (frequency of coverage). In addition, clouds and the processing time required by the data provider complicate a near-real time acquisition of data (timeliness). *Jackson et al. (1986)* emphasized that the factors of timeliness and frequency of coverage must be considered when air- or satellite-borne sensors are used to provide information for farm management. Usefulness of remote sensing data for crop management declines with increasing time required for data acquisition and processing and/or decreasing temporal resolution of data. Some limitations may be reduced by the use of airborne sensor systems or by the launch of future satellite missions providing temporally high-resolution data, e.g. RapidEye. Until today, no spatially high-resolution spaceborne remote sensing system is available that provides data near-real time as required from these applications. Hence, together with their high potential for early stress detection found in this study, near-range sensors meet the requirements of Precision Agriculture more than remote sensing systems as they are highly flexible with respect to timeliness and frequency of coverage. Nevertheless, satellite/airborne remote sensing data may be used for identification of stress factors with lower spatiotemporal dynamics such as soil characteristics or for monitoring the effectiveness of pest control as demonstrated in chapter 5. Near-range detection systems and satellite/airborne remote sensing systems constitute complementary tools for Precision Agriculture applications.

Sensor systems and data processing in Precision Agriculture – no matter if near-range, airborne or satellite systems – are still cost-intensive and thus optimal sensor application dates must be chosen. These are primarily defined by the spatiotemporal dynamics of the observed phenomena itself (in this case by the spatiotemporal dynamics of powdery mildew and leaf rust as analysed in chapter 3). Optimal sensor application dates are bounded to times of disease onset and to periods when fungicide applications are the most effective. Even though for this experiment these dates could be derived for both diseases by multitemporal analyses, no general conclusions can be made, since high spatiotemporal dynamics of observed diseases were found that depend on manifold environmental factors. In order to define dates for sensor-based stress detection, decision support systems are therefore required, considering case-dependent impact factors on crop diseases. Assessments of the temporal dimension of crop stresses demonstrate that required temporal resolution of stress detection systems (as displayed in figure 1.5) is primarily dominated by individual characteristics of phenomena. Hence, complex bio-physiological systems such as fungal crop diseases dictate the requirements of technical systems used to detect them.

Outlook

Practical use of remote sensing data for farm management has yet to be realized. In recent years, no system that meets the requirements of Precision Agriculture in respect to the spatial, temporal, and spectral resolution was available. The launch of future satellite systems such as RapidEye with a high frequency of coverage/repetition rate, for instance, offers a wider scope of applications. However, their suitability and economical benefit for Precision Agriculture has to be proven.
Further studies should focus on the general efficiency of site-specific pest control. More analyses of their ecologic and economic benefits, such as the study of *Godwin et al. (2003)*, are necessary in either case. Studies of the last period of the Research Training Group 722 will focus on decision support systems for Precision Agriculture using input parameters derived by remote sensing and measurements of environmental conditions. In addition, optimal spectral resolutions of sensor data for stress detection will be determined as well as the potential of fusion techniques for near-range acquired multisensoral data.

References

ADAMS, J.B., SMITH, M.O., AND JOHNSON, P.E. (1986): Spectral mixture modelling: a new analysis of rock and soil types at the Viking Lander 1 site. *Journal of Geophysical Research*. 91(B8). 8090-8112.

AHRENS, W.H. (1994): Relative costs of a weed-activated versus conventional sprayer in northern Great Plains fallow. *Weed Technology*. 8. 50-57.

ANONYMOUS (2007): Molecular genetics of the barley powdery mildew fungus (Blumeria graminis f.sp. hordei). Risø National Laboratory, Technical University of Denmark, Biosystems Department. Internet: http://www.risoe.dk/pbk/research_uk/plr/FungalPathogens/MolecularGenetics.htm (May/2007).

APAN, A., HELD, A., PHINN, S., AND MARKLEY, J. (2004): Detecting sugarcane 'orange rust' disease using EO-1 Hyperion hyperspectral imagery. *International Journal of Remote Sensing*. 25(2). 489-498.

BAHRENBERG, G., GIESE, E. AND NIPPER, J. (1999): Statistische Methoden in der Geographie. Band 1. Univariate und bivariate Statistik. Blümel, W.D., Borcherdt, Ch., Kraas, F., Löffler, E. and Wirth, E. (eds.). Stuttgart, Leipzig, Germany.

BATESON, A. AND CURTISS, B. (1996): A method for manual endmember selection and spectral unmixing. *Remote Sensing of Environment*. 55. 229-243.

BAUER, M.E. (1985): Spectral inputs to crop identification and condition assessment. *IEEE Conference Proceedings of the International Geoscience and Remote Sensing Symposia*. 73(6). 1071-1085.

BENLLOCH, J.D. AND RODAS, R.J. (1998): Dynamic model to detect weeds in cereals under actual field conditions. *SPIE Conference Proceedings, Precision Agriculture and Biological Quality*. 3543. 302-310.

BLACKMER, T.M., SCHEPERS, J.S., AND MEYER, G.E. (1995): Remote sensing to detect nitrogen deficiency in corn. *Conference Proceedings - Site-Specific Management for Agricultural Systems*. 505-512.

BLACKSHAW, R.P. AND VERNON, R.S. (2006): Spatiotemporal stability of two beetle populations in non-farmed habitats in an agricultural landscape. *Journal of Applied Ecology*. 43(4). 680-689.

BLAKEMAN, R.H., BRYSON, R.J., AND DAMPNEY, P. (2000): Assessing crop condition in real time using high resolution satellite imagery. *Aspects of Applied Biology, Remote Sensing in Agriculture*. 60. 163-171. Editors: Bryson,R.J., Howard,W., Riding,A.E., Simmonds,L.P., Steven,M.D., Wellesbourne, UK.

BLASCO, J., BENLLOCH, J.V., AGUSTI, M., AND MOLTO, E. (1998): Machine vision for precise control of weeds. *SPIE Conference Proceedings, Precision Agriculture and Biological Quality*. 3543. 336-343.

BOARDMAN, J.W., KRUSE, F.A., AND GREEN, R.O. (1995): Mapping target signatures via partial unmixing of AVIRIS data. *Summaries of the 5th JPL Airborne Earth Science Workshop*. 95(1). 23-26. Jet Propulsion Laboratory, Pasadena, CA.

BOARDMAN, J.W. (1998): Leveraging the high dimensionality of AVIRIS data for improved sub-pixel target unmixing and rejection of false positives: mixture tuned matched filtering. *Summaries of the 7th JPL Airborne Earth Science Workshop*. 97(1). 55-56. Jet Propulsion Laboratory, Pasadena, CA.

BONGIOVANNI, R. AND LOWENBERG-DEBOER, J. (2004): Precision Agriculture and Sustainability. *Precision Agriculture*. 5. 359-387.

BRAUN, U. (1987): A monograph of the Erysiphales (powdery mildews). *Beih. Nova Hedwigia*. 89. 1-700.

BRAVO, C., MOSHOU, D., OBERTI, R., WEST, J.S., MCCARTNEY, A., BODRIA, L., AND RAMON, H. (2004): Foliar disease detection in the field using optical sensor fusion. *Agricultural Engineering International: the CIGR Journal of Scientific Research and Development*. 6. 1-14.

CAO, C., AND LAM, N.S.-N. (1997): Understanding the Scale and Resolution Effects in Remote Sensing and GIS. In: Quattrochi D.A. and Goodchild, M.F. (eds.): Scale in Remote Sensing and GIS. Boca Raton. S. 57- 72.

CARTER, G.A. (1991): Primary and secondary effects of water content on the spectral reflectance of leaves. *American Journal of Botany*. 78. 916-924.

CARVER, T.L.W., ROBERTS, P.C., THOMAS, B.J., AND LYNKAER, M.F. (2001): Inhibition of *Blumeria graminis* germination and germling development within colonies of oat mildew. *Physiological and Molecular Plant Pathology*. 58. 209-228.

CASA, R. AND JONES, H.G. (2003): Field-based multiangular remote sensing for plant stress. *Conference Proceedings of the 4th European Conference on Precision Agriculture*. 2003. 109-113. Berlin, Germany.

CLARKE, M. (2005): An assessment of hyperspectral and lidar remote sensing for the monitoring of tropical rain forest trees. *PhD Thesis*. 319pp. University of California, Santa Barbara.

CUMMINS, G.B. AND HIRATSUKA, Y. (2003): Illustrated Genera of rust fungi, Third Edition. The American Phytopathological Society, St.Paul, Minnesota.

DALAL, R.C. AND HENRY, R.J. (1986): Simultaneously determination of moisture, organic carbon and total nitrogen by near-infrared reflectance spectrophotometry. *Soil Science Society Am. J.* 50. 120-123.

DENNISON, P.E. AND ROBERTS, D.A. (2003): Endmember selection for Multiple Endmember Spectral Mixture Analysis using Endmember Average RSME. *Remote Sensing of Environment*. 87(2-3). 123-135.

DENNISON, P.E., HALLIGAN, K., AND ROBERTS, D.A. (2004): A comparison of error metrics and constraints for Multiple Endmember Spectral Mixture Analysis and Spectral Angle Mapper. *Remote Sensing of Environment*. 93. 359-367.

DU, Q., FRENCH, J.V., SKARIA, M., YANG, C., AND EVERITT, J.H. (2004): Citrus pest stress monitoring using airborne hyperspectral imagery. *IEEE Conference Proceedings of the International Geoscience and Remote Sensing Symposia*. VI. 3981-3984. Anchorage, USA.

ESTEP, L. AND DAVIS, B. (2000): Nutrient stress detection in corn using neural networks and AVIRIS hyperspectral imagery. *Summaries of the 10th JPL Airborne Earth Science Workshop*. Jet Propulsion Laboratory, Pasadena, CA.

ESTEP, L., TERRIE, G., AND DAVIS, B. (2004): Crop stress detection using AVIRIS hyperspectral imagery and artificial neural networks. *International Journal of Remote Sensing*. 25, No.22. 4999-5004.

EUROPEAN COMMISSION (2002): Agriculture in the European Union, statistical and economic information 2001. Brussels, Belgium.

EUROPEAN COMMISSION (2002): Communication from the Commission to the Council, the European Parliament, the Economic and Social Committee and the Committee of the Regions On the sixth environment action programme of the European Community' Environment 2010: Our future, Our choice' - The Sixth Environment Action Programme - Proposal for a Decision of the European Parliament and of the Council laying down the Community Environment Action Programme 2001-2010. Brussels, Belgium.

EVERTS, K.L., LEATH, S., AND FINNEY, P.L. (2001): Impact of Powdery Mildew and Leaf Rust on milling and baking quality of Soft Red Winter Wheat. *Plant Disease*. 85. 423-429.

FILLELA, I., SERRANO, L., SERRA, J., AND PENUELAS, J. (1995): Evaluating wheat nitrogen status with canopy reflectance indices and discriminant analysis. *Crop Science*. 35. 1400-1405.

FLATEN, J.A. AND PARENDO, K.A. (2001): Pendulum waves: a lesson in aliasing. *American Journal of Physics*. 69(7). 778-782.

GAMON, J.A., SERRANO, L., AND SURFUS, J.S. (1997): The Photochemical Reflectance Index: an optical indicator of photosynthetic radiation use efficiency across species, functional types and nutrient levels. *Oecologia*. 112. 492-501.

GEBHARDT, S., SCHELLBERG, J., LOCK, R., AND KÜHBAUCH, W. (2006): Identification of broad-leaved dock (*Rumex obtusifolius* L.) on grassland by means of digital image processing. *Precision Agriculture*. 7. 165-178.

GERHARDS, R., AND OEBEL, H. (2006): Practical experiences with a system for site-specific weed control in arable crops using real-time image analysis and GPS-controlled patch spraying. *Weed Research.* 46. 185-193.

GLAWE, D.A. AND GROVE, G.G. (2006): Powdery mildew diseases. An online guide to plant disease control. Oregon State University Extension. Internet: http://plant-disease.ippc.orst.edu/articles.cfm?article_id=30 (May/2007).

GODWIN, R.J., RICHARDS, T.E., WOOD, G.A., WELSH, J.P., AND KNIGHT, S.M. (2003): An economic analysis of the potential for Precision Farming in UK cereal production. *Biosystems Engineering*. 84(4). 533-545.

GREEN, A.A., BERMAN, M., SWITZER, P. AND CRAIG, M.D. (1988): A transformation for ordering multispectral data in terms of image quality with implications for noise removal. *IEEE Transactions on Geoscience and Remote Sensing*. 26(1). 65-74.

HANSEN, P.M. AND SCHJOERRING, J.K. (2003): Reflectance measurement of canopy biomass and nitrogen status in wheat crops using normalized difference vegetation indices and partial least squares regression. *Remote Sensing of Environment*. 86(4). 542-553.

HUANG, W., LIU, L., HUANG, M., WANG, J., AND WAN, H. (2004): Monitoring of wheat yellow rust with dynamic hyperspectral data. IEEE *Conference Proceedings of the International Geoscience and Remote Sensing Symposia*. Anchorage, Alaska.

HUETE, A.R., JUSTICE, C., AND VANLEEUWEN, W. (1999): Modis Vegetation Index (MOD 13). Algorithm Theoretical Basis Document. Internet: http://modis.gsfc.nasa.gov/data/atbd/atbd_mod13.pdf (May/2007).

HUNGER, B. AND JACKSON, A. (2004): Foliar fungicides and wheat production in Oklahoma. Oklahoma State University, Cooperative Extension Service. Internet: http://lubbock.tamu.edu/wheat/pdfs/osufoliarfunghandout04.pdf (May/2007).

JACKSON, R.D., IDSO, S.B., REGINATO, R.J., AND PINTER, P.J. (1981): Crop temperature as a crop water stress indicator. *Water Resource Research*. 17. 1133-1138.

JACKSON, R.D., PINTER, P.J., REGINATO, R.J., AND IDSO, S.B. (1986): Detection and evaluation of plant stresses for crop management decisions. *IEEE Transactions on Geoscience and Remote Sensing*. 24(1). 99-106.

JACOBI, J. AND KÜHBAUCH, W. (2005): Site-specific identification of fungal infection and nitrogen deficiency in wheat crop using remote sensing. *Conference Proceedings of the 5th European Conference on Precision Agriculture*. 2005. 73-80. Uppsala, Sweden.

JACOBI, J. (2005): Teilflächige Diagnose von Pilzbefall und Stickstoffmangel an Weizen mit Hilfe der optischen Fernerkundung. *PhD Thesis*. Online-Publikationen an deutschen Hochschulen, University of Bonn.

JENSEN, J.R. (2000): Remote sensing of the environment – An earth resource perspective. Upper Saddle River, NJ, USA.

JÜRGENS, C. (2000): Fernerkundungsanwendungen im Precision Farming. *Petermanns Geographische Mitteilungen.* 144. 60-69.

KANEMASU, E.T., NIBLETT, C.L., MANGES, H., LENHERT, D., AND NEWMAN, M.A. (1974): Wheat: its growth and disease severity as deduced from ERTS-1. *Remote Sensing of Environment*. 3(4). 255-260.

KLUGE, E., ENZIAN, S., AND GUTSCHE, V. (1999): Befallsatlas. Atlas der potentiellen Befallsgefährdung durch wichtige Schadorganismen im Ackerbau Deutschlands. Biologische Bundesanstalt für Land- und Forstwirtschaft.

KÜHBAUCH, W. AND HAWLITSCHKA, S. (2003): Remote sensing - a future technology in precision farming. *Conference Proceedings of the Workshop on POLinSAR - Applications of SAR Polarimetry and Polarimetric Interferometry* (ESA SP-529). Frascati, Italy.

LARSOLLE, A. AND HAMIT MUHAMMED, H. (2007): Measuring crop status using multivariate analysis of hyperspectral field relectance with application to disease severity and plant density. *Precision Agriculture*. 8. 37-47.

LELONG, C.C.D., PINET, P.C., AND POILVÉ, H. (1998): Hyperspectral Imaging and Stress Mapping in Agriculture: A Case Study on Wheat in Beauce (France). *Remote Sensing of Environment*. 66(2). 179-191.

LIPPS, P.E. (2006): Leaf rust of wheat. Fact sheet. Ohio State University Extension, Plant Pathology. Internet: http://ohioline.osu.edu/ac-fact/0006.html (May/2007).

LÖFFLER, E. (1994): Geographie und Fernerkundung. Eine Einführung in die geographische Interpretation von Luftbildern und modernen Fernerkundungsdaten. Blümel, W.D., Borcherdt, Ch., Löffler, E. and Wirth, E. (eds.). Stuttgart, Germany.

LORENZEN, B. AND JENSEN, A. (1989): Changes in leaf spectral properties induced in barley by cereal powdery mildew. *Remote Sensing of Environment*. 27. 201-209.

MACHADO, S., BYNUM, E.D., ARCHER, T.L., BORDOVSKY, J., ROSENOW, D.T., PETERSON, C., BRONSON, K., NESMITH, D.M., LASCANO, R.J., WILSON, L.T., AND SEGARRA, E. (2002): Spatial and temporal variability of sorghum grain yield: influence of soil, water, pests, and diseases relationships. *Precision Agriculture*. 3. 389-406.

MACLEAN, D.J. (1982): Axenic culture and metabolism of rust fungi. In: Scott, K.J. and Chakravorty (eds.): The rust fungi. Academic Press Inc. (London) Ltd., London, UK.

MALTHUS, T.J. AND MADEIRA, A.C. (1993): High resolution spectroradiometry: Spectral reflectance of field bean leaves infected by *Botrytis fabae* . *Remote Sensing of Environment*. 45(1). 107-116.

MARSALIS, M.A. AND GOLDBERG, N.P. (2006): Leaf, stem and stripe rust diseases of wheat. New Mexico State University, Cooperation Extension Service, College of Agriculture and Home Economics. Internet: http://cahe.nmsu.edu/pubs/_a/A-415.pdf (May/2007).

MATHIEU, R., SBIH, M., VIAU, A.A., ANCTIL, F., PARENT, L.E., AND BOISVERT, J. (2003): Relationships between Radarsat SAR data and surface moisture content of agricultural organic soils. *International Journal of Remote Sensing*. 24(24). 5265-5281.

McBRATNEY, A., WHELAN, B., ANCEV, T., AND BOUMA, J. (2005): Future direction of Precision Agriculture. *Precision Agriculture.* 6. 7-23.

MORAN, M.S., CLARKE, T.R., INOUE, Y., AND VIDAL, A. (1994): Estimating crop water deficit using the relationship between surface-air temperature and spectral vegetation index. *Remote Sensing of Environment*. 49. 246-263.

MORAN, M.S., INOUE, Y., AND BARNES, E.M. (1997): Opportunities and limitations for image-based remote sensing in precision crop management. *Remote Sensing of Environment*. 61(3). 319-346.

MOSCHINI, R.C. AND PÉREZ, B.A. (1999): Predicting wheat leaf rust severity using planting date,genetic resistance, and weather variables. *Plant Disease*. 83(4). 381-384.

MOSHOU, D., BRAVO, C., WEST, J.S., WAHLEN, S., MCCARTNEY, H.A., AND RAMON, H. (2004): Automatic detection of 'yellow rust' in wheat using reflectance measurements and neural networks. *Computers and Electronics in Agriculture*. 44. 173-188.

MOSHOU, D., BRAVO, C., WAHLEN, S., WEST, J., MCCARTNEY, A., DE BAERDEMAEKER, J., AND RAMON, H. (2006): Simultaneous identification of plant stresses and diseases in arable crops using proximal optical sensing and self-organising maps. *Precision Agriculture*. 7. 149-164.

MOUNT, M.S. AND SLESINSKI, R.S. (1971): Characteristics of primary development of powdery mildew. *Conference Proceedings of the International Symposium of Ecology of leaf surface micro-organisms*. 301-322. Academic Press, London, New York.

NELSON, S.C. AND CAMPBELL, C.L. (1993): Comparative spatial analysis of foliar epidemics on winter clover caused by viruses, fungi and a bacterium. *Phytopathology*. 83(3). 288-301.

NELSON, S.C. (1996): A simple analysis of disease foci. *Phytopathology*. 86(4). 332-339.

NEUDECKER, E., SCHMIDHALTER, U., SPERL, C., AND SELIGE, T. (2001): Site-specific soil mapping by electromagnetic induction. *Conference Proceedings of the 3rd European Conference on Precision Agriculture*. 271-276. Agro Montpellier, Montpellier, France.

NIELSEN, K.A., NICHOLSON, R.L., CARVER, T.L.W., KUNOH, H., AND OLIVER, R.P. (2000): First touch: An immediate response to surface recognition in conidia of *Blumeria graminis*. *Physiological and Molecular Plant Pathology*. 56. 63-70.

OERKE, E.-C., DEHNE, H.-W., SCHÖNBECK, F., AND WEBER, A. (1994): Crop production and crop protection – estimated losses in major food and cash crops. Elsevier Science. 808pp.

PARKER, S.K., NUTTER, F.W., AND GLEASON, M.L. (1997): Directional spread of Septoria Leaf Spot in tomato rows. *Plant Disease*. 81(3). 272-276.

PARKER, S.R., SHAW, M.W., AND ROYLE, D.J. (1995): The reliability of visual estimated disease severity on cereal leaves. *Plant Pathology*. 44(5). 856-864.

PERRY, J.N. (1995): Spatial analysis by distance indices. *Journal of Animal Ecology*. 64. 303-314.

PERRY, J.N. (1998): Measures of spatial pattern for counts. *Ecology*. 79(3). 1008-1017.

PERRY, J.N., WINDER, L., HOLLAND, J.M., AND ALSTON, R.D. (1999): Red-blue plots for detection of cluster in count data. *Ecology Letters*. 2. 106-113.

PERRY, J.N. AND DIXON, P.M. (2002): A new method to measure spatial association for ecological count data. *Ecoscience*. 9. 133-141.

PETHYBRIDGE, S.J. AND TURECHEK, W.W. (2003): Analysis of the association among three viruses infecting hop in Australia. *Plant Pathology*. 52(2). 158-167.

PETHYBRIDGE, S.J., ESKER, P., HAY, F., WILSON, C., AND NUTTER, F.W. (2005): Spatiotemporal description of epidemics caused by Phoma ligulicola in Tasmanian Pyrethrum fields. *Phytopathology*. 95(6). 648-658.

PINTER JR., P.J., HATFIELD, J.L., SCHEPERS, J.S., BARNES, E.M., MORAN, M.S., DAUGHTRY, C.S.T., AND UPCHURCH, D.R. (2003): Remote Sensing for crop management. *Photogrammetric Engineering & Remote Sensing.* 69(6). 647-664.

QUINLAN, J.R. (1993): C4.5: programs for machine learning. Morgan Kaufmann Publishers, Inc., CA, USA.

RASCHER, U., NICHOL, C.J., SMALL, C., AND HENDRICKS, L. (2007): Monitoring spatio-temporal dynamics of photosynthesis with a portable hyperspectral imaging system. A case-study to quantify photosynthetic efficiency on genetically modified *Arabidopsis thaliana* (L.) Heynh. plants and on leaves of four drought stressed tropical tree species. *Photogrammetric Engineering and Remote Sensing*. 73(1). 45-56.

ROBERTS, D.A., DENNISON, P.E., GARDNER, M., HETZEL, Y., USTIN, S.L., AND LEE, C. (2003): Evaluation of the potential of Hyperion for fire danger assessment by comparison to the Airborne Visible/Infrared Imaging Spectrometer. *IEEE Transactions on Geoscience and Remote Sensing*. 41 (6). 1297-1310.

ROBERTS, D.A., HALLIGAN, K., AND DENNISON, P.E. (2007): VIPER Tools user manual. Version 1.2. Internet: www. vipertools. org (May/2007).

ROELFS, A.P. (1972): Gradients in horizontal dispersal of cereal rust uredospores. *Phytopathology*. 62. 70-76.

SASAKI, Y., OKAMOTO, T., IMOU, K., AND TORII, T. (1998): Automatic diagnosis of plant disease- spectral reflectance of healthy and diseased leaves. Conference *Proceedings of the 3rd IFAC/CIGR Workshop on Artificial Intelligence in Agriculture*. 158-163.

SAVITZKY, A. AND GOLAY, J.M.E. (1964): Smoothing and differentiation of data by simplified least squares procedures. *Analytical Chemistry*. 36(8). 1627-1639.

SHAH, D.A., BERGSTROM, G.C., AND UENG, P.P. (2001): Foci of Stagonospora Nodorum Blotch in winter wheat before canopy development. *Phytopathology*. 91(7). 642-647.

SHAW, D. AND KELLEY, F. (2005): Evaluating Remote Sensing for determining and classifying soybean anomalies. *Precision Agriculture*. 6. 421-429.

SMITH, R.C.G., PRATHAPAR, S.A., AND SLAVICH, H.D.B.P. (1989): Use of a thermal scanner image of a water stressed crop to study soil spatial variability. *Remote Sensing of Environment*. 29(2). 111-120.

TAUBENHOUS, J.J., EZEKIEL, W.N., AND NEBLETTE, C.B. (1929): Airplane photography in the study of cotton root rot. *Phytopathology*. 19. 1025-1029.

THOMAS, C.F.G., PARKINSON, L., GRIFFITHS, G.J.K., FERNANDEZ GARCIA, A., AND MARSHALL, E.J.P. (2001): Aggregation and temporal stability of carabid beetle distributions in field and hedgerow habitats. *Journal of Applied Biology*. 38(1). 100-116.

THOMAS, M.R., COOK, R.J., AND KING, J.E. (1989): Factors affecting development of *Septoria tritici* in winter wheat and its effect on yield. *Plant Pathology*. 38. 246-257.

TIAN, L., REID, J.F., AND HUMMEL, J.W. (1999): Development of a precision sprayer for site-specific weed management. *Transactions ASAE*. 42. 893-900.

TOMPKINS, S., MUSTARD, J.F., PIETERS, C.M., AND FORSYTH, D.W. (1997): Optimization of endmembers for spectral mixture analysis. *Remote Sensing of Environment*. 59. 472-489.

TROLL, C. (1966): Luftbildforschung und landeskundliche Forschung. *Erdkundliches Wissen*. 12. Wiesbaden. Germany.

TUBAJIKA, K.M., CIVEROLO, E.L., CIOMPERLIK, M.A., LUVISI, D.A., AND HASHIM, J.M. (2004): Analysis of the spatial patterns of Pierce's disease incidence in the lower San Joaquin Valley in California. *Phytopathology*. 94. 1136-1144.

VERMA, K.S., SAXENA, R.K., HAJARE, T.N., KHARCHE, V.K., AND ANANTHA KUMARI, P. (2002): Spectral response of gram varieties under variable soil conditions. *International Journal of Remote Sensing*. 23(2). 313-324.

VOSS, K. (2005): Beitrag zur skalenabhängigen Erfassung teilschlagspezifischer Pflanzenschäden mit Methoden der Fernerkundung und Geoinformation. *PhD Thesis*. Online-Publikationen an deutschen Hochschulen, University of Bonn.

WARNER, D.J., ALLEN-WILLIAMS, L.J., WARRINGTON, W., FERGUSON, A.W., AND WILLIAMS, I.H. (2003): Mapping, characterisation, and comparison of the spatio-temporal distributions of cabbage stem flea beetle (*Psylliodes chrysocephala*), carabids, and Collembola in a crop of winter oilseed rape (*Brassica napus*). *Entomologia Experimentalis et Applicata*. 109(3). 225-234.

WATKINS, J. (2007): Leaf, stem and stripe rust diseases of wheat. University of Nebraska-Lincoln Extension, Institute of Agriculture and Natural Resources. Internet: http://www.ianrpubs.unl.edu/sendIt/g1245.html (May/2007).

WEST, J.S. AND MCCARTNEY, H.A. (2002): Optical disease detection and estimation of latent infections around disease foci for targeted pesticide application. *Aspects of Applied Biology*. 66. 463-468.

WEST, J.S., BRAVO, C., OBERTI, R., LEMAIRE, D., MOSHOU, D., AND MCCARTNEY, H.A. (2003): The potential of optical canopy measurement for targeted control of field crop diseases. *Annual Review Phytopathology*. 41. 593-614.

WILLIAMS, A.M. AND HUNT JR, E.R. (2002): Estimation of leafy spurge cover from hyperspectral imagery using mixture tuned matched filtering. *Remote Sensing of Environment*. 82. 446-456.

WINDER, L., ALEXANDER, C.J., HOLLAND, J.M., SYMONDSON, W.O.C., PERRY, J.N., AND WOOLLEY, C. (2005): Predatory activity and spatial pattern: the response of generalist carabids to their aphid prey. *Journal of Animal Ecology*. 74(3). 443-454.

WRIGHT, A.J., CARVER, T.L.W., THOMAS, B.J., FENWICK, N.I.D., KUNOH, H., AND NICHOLSON, R.L. (2000): The rapid and accurate determination of germ tube emergence site by *Blumeria graminis* conidia. *Physiological and Molecular Plant Pathology*. 57. 281-301.

WRIGHT, A.J., THOMAS, B.J., AND CARVER, T.L.W. (2002): Early adhesion of *Blumeria graminis* to plant and artificial surfaces demonstrated by centrifugation. *Physiological and Molecular Plant Pathology*. 61. 217-226.

XU, X.M. AND RIDOUT, M.S. (1998): Effects of initial epidemic conditions, sporulation rate, and spore dispersal gradient on the spatio-temporal dynamics of plant disease epidemics. *Phytopathology*. 88. 1000-1012.

XU, X.M. AND MADDEN, L.V. (2003): Considerations for the use of SADIE statistics to quantify spatial patterns. *Ecography*. 26. 821-830.

XU, X.M. AND MADDEN, L.V. (2004): Use of SADIE statistics to study spatial dynamics of plant disease epidemics. *Plant Pathology*. 53. 38-49.

YANG, X.B. AND TEBEST, D.O. (1992): Dynamic pathogen distribution and logistic increase of plant disease. *Phytopathology*. 82. 380-383.

ZADOCKS, J.C., CHANG, T.T., AND KONZAK, T.F. (1974): A decimal code for the growth stages of cereals. *Weed Research*. 14. 415-421.

Appendix

A1. Special Chapter: Inconsistencies in remote sensing data caused by sensor-specific relative spectral response functions

A1.1 Introduction

Time series analyses are powerful tools for vegetation monitoring applications. Due to low temporal resolutions of some space-borne sensors, the use of various sensors of different platforms is essential for multitemporal or temporally highly resolved vegetation monitoring. However, different sensor characteristics cause inconsistencies in remote sensing data. The acquisition geometry of the sensor, like viewing- and solar angle, atmospheric conditions, topography and spatial resolution influence the reflectance values. This study contributes to another important factor, the spectral characteristics of sensor bands. This factor influences reflectance values of monitored targets caused by different sensitivities of bands (different relative spectral response (RSR) functions). Values of vegetation indices (VI) like the most often used VI *(Bannari et al. 1995)*, the Normalized Difference Vegetation Index (NDVI) particularly vary to the according sensor. Thus, a direct comparison or a synergistic use of the NDVI of different sensor systems is critical. Several studies indicated these NDVI offsets caused by spectral band characteristics and/or all influencing factors and supposed approaches to minimize those variations *(Trishchenko et al. 2002, Steven et al. 2003, Franke & Menz 2005, Miura et al. 2006, van Leeuwen et al. 2006).*

In this analysis, a spectral simulation of 3 different multispectral sensor systems (Landsat 5TM, QuickBird and SPOT5) based on airborne hyperspectral HyMap data was performed. The simulation accuracy was evaluated with real Landsat 5TM imagery acquired on the same day. The objective of this study was to develop an accurate multispectral band simulation method in order to quantify NDVI differences between Landsat 5TM, QuickBird and SPOT5, caused by the effect of sensor-dependent RSR functions.

A1.2 Band characteristics

A spectral band of a sensor can be described by its spectral range, bandwidth, center wavelength and full width at half maximum (FWHM). In more detail, it can be characterised by its RSR function that takes into account all the features describing a band. The RSR of each band of a sensor system is characterized by the effective spectral quantum efficiency (QE) of the detector. The QE indicates the spectral sensitivity of a charge-coupled device (CCD) to incoming light at each wavelength. More precisely it gives the number of electrons produced in the detector per incoming photon (dimensionless or amps/watt). The effective spectral QE includes not only the type-dependent sensitivity of the CCD, but also losses due to the light reflecting or transmitting components of the detector (e.g. optics, mirrors, filters, coatings etc.). Variable sensor systems thus have different spectral sensitivity, which are described by their individual RSR functions.

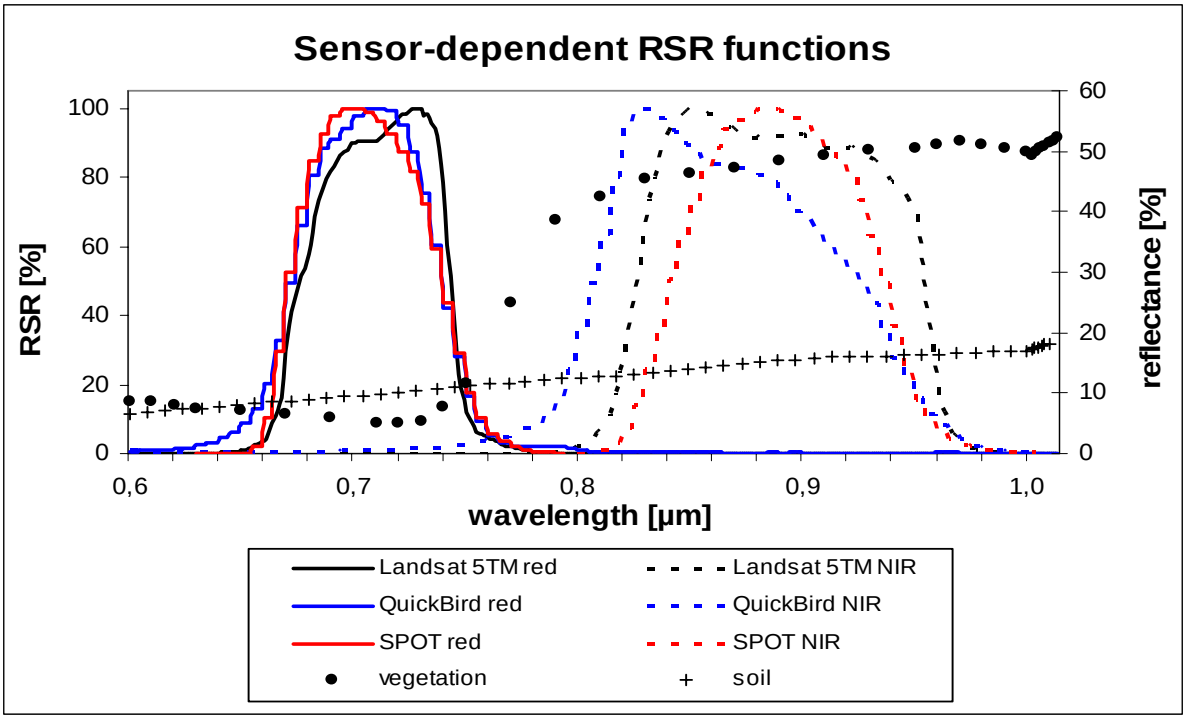

Figure A1.1: RELATIVE SPECTRAL RESPONSE FUNCTIONS of the red and near-infrared bands of Landsat 5TM, QuickBird and SPOT5 with 2 typical land cover spectra

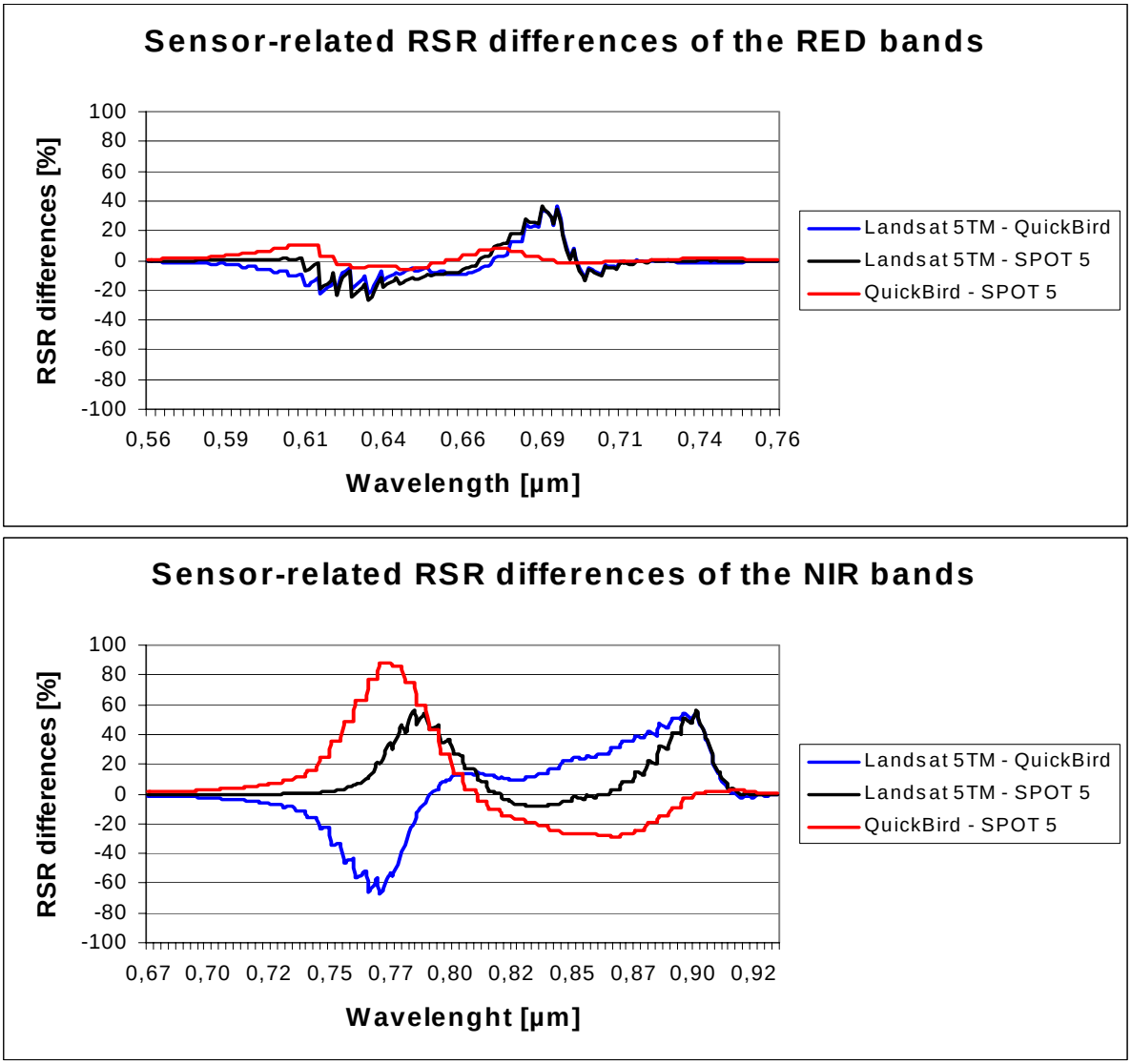

Figure A1.2a/b: SENSOR-RELATED DIFFERENCES (%) OF THE RELATIVE SPECTRAL RESPONSE FUNCTIONS of the red (a) and near-infrared (b) bands of the sensors

Figure A1.1 shows the RSR functions of the red and NIR bands of the different sensors used in this study. Two typical spectra of different land cover are plotted as reference. The band-specific RSR functions differ in shape and central wavelength location. In particular, RSR functions of the sensors vary in the NIR region. Conspicuous is that the gap between the red and NIR band of Landsat 5TM as well as of SPOT5 is wider than the gap between the QuickBird bands, where even an overlap exists. Thus, the QuickBird bands are closer to the red edge. The red bands of the 3 sensors are more similar than the NIR bands, which is more obvious in figure A1.2 that shows the RSR differences between the red (figure A1.2a) and NIR (figure

A1.2b) sensor bands. Whereas the red bands of QuickBird and SPOT5 are similar, the NIR bands of these sensors show the widest differences up to over 80% at 0.77µm. Due to the wide differences between the NIR bands, the RSR functions of these bands affect the NDVI more than those of the red bands.

A1.3 Study site and data

The test site is shown in chapter 1.6. The HyMap flight campaign took place on 28 May 2005 (12.00 am). HyVista corp. and the DLR (German Aerospace Center) carried out the geometric and atmospheric correction of the data.
The Landsat 5TM acquisition was on the same day at 10.30 am. The pre-processing of the image included an atmospheric correction with the software ATCOR 3 by the use of a digital elevation model. Spectroradiometer measurements with a FieldSpec Pro (Analytical Spectral Devices, Boulder, CO, USA), taken at the same day, were used to validate the atmospheric correction. Afterwards, the Landsat 5TM and HyMap image were co-registered with a RMS-error less than 0.5.

A1.4 Methodology

Some sensor simulation methods have tried to take the geometric and spectral differences of the sensors into account *(Kavzoglu 2004)*. Because the main objective of this special chapter is to assess spectral differences solely caused by different RSR functions, only the spectral characteristic of the sensors were simulated by constant side-parameters.
As a prerequisite for the following data simulation, the RSR values of each multispectral band were attached to the according wavelengths of the 126 hyperspectral bands. Therefore, each HyMap center wavelength was linked with the mean RSR value (in the range of FWHM of the hyperspectral band) of the simulating band.
An in-house developed IDL-program facilitates any user-predefined multispectral band simulation with regard to the band-specific RSR function. The 126 HyMap reflectance values of each pixel were thereby multiplied by the 126 wavelength corresponding RSR values of the simulating band. The sum of these products is

divided by the sum of the 126 band-specific RSR values. For a multispectral sensor simulation, each band must be simulated according to the following equation, where $R\text{sim}_b$ is the simulated pixel reflectance value of the simulated band, R_i is the pixel reflectance value of the HyMap band and $rsr_{b,i}$ is the RSR value of the simulating band at each HyMap corresponding wavelength.

$$R_{sim_b} = \frac{\sum_{i=1}^{n} R_i * rsr_{b,i}}{\sum_{i=1}^{n} rsr_{b,i}} \qquad 1 \leq n \leq 126 \qquad \text{(A1.1)}$$

The results were simulated multispectral bands that provide spectral information similar to those of the original sensor bands. Nevertheless, differences to original data caused by different spatial resolution or sun/sensor/target geometry still exist. This fact has to be considered by following validation of the simulation.

In order to assess the accuracy of the simulation method an extensive evaluation was performed by the use of an original Landsat 5TM image. Reflectance differences of the imagery were assessed as an indication of the data simulation quality. The overall differences of both data sets do not differ significantly with values between 0.08% and 1.45% reflectance (table A1.1), by a mean of 0.79%. Highest congruence between original and simulated data could be achieved in band 3, widest differences existed in band 7.

Obvious was a general underestimation of reflectance values of the simulated data. These slight statistical differences had various reasons. In comparison to the original Landsat 5TM data set, the simulation did not consider variations due to different spatial resolution or sun/sensor/target geometry. In addition, different atmospheric corrections of original and simulated data caused slight variations as well. Generally, variations in reflectance values occur due to different overpass time and off-nadir viewing. The last point is particularly critical for airborne sensors *(Schiefer et al. 2006)*. Bi-directional reflectance factor effects caused by different illumination and observation angles within the HyMap scene were negligible due to a south to north

flight direction at noon. In addition, the solar illumination geometry was similar at Landsat 5TM and HyMap overpass times (within 1.6°).

Table A1.1: BAND-WISE MEAN AND STANDARD DERIVATION OF REFLECTANCE IN % AND NDVI FOR ORIGINAL- AND SIMULATED LANDSAT 5TM of the entire scene, as well as reflectance/NDVI differences

	Simulated Landsat		**Original Landsat**		***absoluteDIFF***
	Mean	***STDEV***	***Mean***	***STDEV***	
Band 1	4.0 %	4.0 %	5.0 %	3.3 %	0.96 %
Band 2	6.9 %	5.4 %	7.7 %	4.8 %	0.80 %
Band 3	7.5 %	6.6 %	7.5 %	6.1 %	0.08 %
Band 4	34.3 %	12.4 %	34.8 %	10.2 %	0.46 %
Band 5	18.0 %	8.3 %	19.0 %	7.3 %	1.01 %
Band 7	11.0 %	8.7 %	12.4 %	8.1 %	1.45 %
NDVI	0.635	0.277	0.639	0.258	0.004

Kerekes & Landgrebe (1989) estimated the effect of these differences causing factors from 5-10% in reflectance. In the study of *Kalman & Peltzer (1993)*, a simulation of Landsat TM imagery on the basis of AVIRIS data was accomplished. The comparison showed an offset of the mean DN values from 0.4% up to 5.3% according to the band. *Teilet et al. (2003)* compared Landsat 5TM and 7ETM+ and showed a spectral band difference in the range of 2-7% depending on the band that lead to NDVI differences of 1% to 4% (mean 2.5%).

The validation of the NDVI differences between original and simulated Landsat 5TM shows a high congruence as well. Table A1.1 also shows NDVI differences of simulated and original Landsat 5TM. The differences in the NDVI values were marginal, with a difference of 0.004 (0.62%). Finally, the validation by a comparison between original and simulated Landsat 5TM imagery showed a well performance of the simulation method.

A1.5 Results

The advantage of the comparison between simulated data sets, which were simulated according equation A1.1, is that only differences of interest are included. Thus, the NDVI of the simulated images were calculated, in order to assess the NDVI differences solely caused by different sensor-dependent RSR functions. Landsat 5TM showed a mean NDVI of 0.64, QuickBird of 0.62 and SPOT5 of 0.66.

Table A1.2: Minimum, Maximum, Mean and percentage NDVI differences between simulated Landsat 5TM, QuickBird and SPOT5 simulated imagery

	Min. NDVI difference	**Max. NDVI difference**	**Mean NDVI difference**	**Difference (%)**
Landsat-QuickBird	-0.064	0.099	0.014	2.2
Landsat-SPOT	-0.126	0.157	-0.025	3.9
QuickBird-SPOT	-0.083	0.074	-0.039	6.3

Table A1.2 shows the minimum, maximum and mean NDVI differences (in %) of the simulated images. The lowest mean differences of NDVI with 2.2% occurred between Landsat 5TM and QuickBird. A mean difference of 3.9% showed the comparison of Landsat 5TM and SPOT5, whereas the widest range of differences occurred (from -0.126 up to 0.157). Widest NDVI differences showed QuickBird and SPOT5 with 6.3%, due to the widest difference in RSR functions of the NIR bands (figure A1.1).
Those NDVI differences were also obvious in the histograms of the NDVI distributions of the 3 simulated images (figure A1.3). Considering the sensor-dependent NDVI distributions, a similar shape of the histograms by a shift in range became apparent as well as the wide difference between QuickBird and SPOT5 caused by wide differences between their RSR functions in the NIR. An important fact is that the higher the NDVI value, the wider the differences, which is obvious by closer examination of both peaks. Primarily, the similar shapes of the histograms that showed a shift in range and a slight stretch indicate a systematic but non-linear NDVI offset of the different sensors.

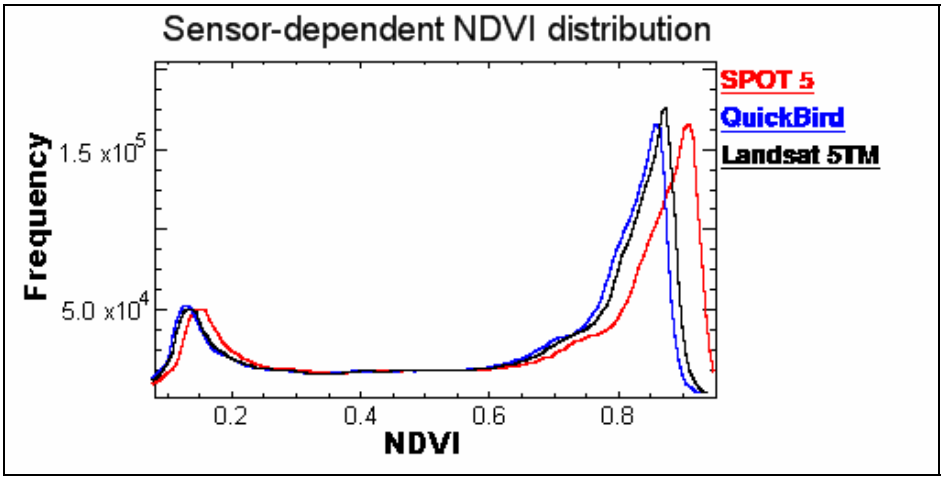

Figure A1.3: SENSOR-DEPENDENT NDVI DISTRIBUTIONS of simulated SPOT5, QuickBird and Landsat 5TM imagery

A1.6 Conclusion

In this chapter, the performance quality of a sensor simulation method that allows the simulation of multispectral data was empirically investigated. This approach uses specific RSR functions of the simulating sensors and creates bands that are spectrally similar to original multispectral data sets. The main objective of this method was an accurate modelling of spectral band features. The validation of the simulation approach showed a high congruence between original and simulated Landsat 5TM images and approved the performance quality. Thus, NDVI data sets were created that contained differences solely caused by spectral characteristics of the sensors.

The assessment of NDVI differences between Landsat 5TM, QuickBird and SPOT5 showed substantial differences between the sensor systems. Wide NDVI differences could be traced back to wide differences of the sensor-dependent RSR functions. An important factor for possible sensor-intercalibration approaches is that a systematic, but non-linear NDVI offset occurred. Therefore, an intercalibration approach using a polynomial order is suggested to adjust NDVI differences caused by varying RSR functions. A similar approach was already suggested by *Trishchenko et al. (2002)*. Due to the fact that NDVI differences caused by different RSR functions are clearly determinable against other differences causing factors, a stepwise sensor NDVI intercalibration is desirable. Thereby, the spectral characteristics of the sensors have

to be taken into account in a first step, residual factors such as different sun/sensor/target geometry, different spatial resolution etc. could be realized in a second step. Such an intercalibration is necessary for multisensoral NDVI analyses, in order to ensure comparability of results.

A1.7 References of the special chapter

BANNARI, A., MORIN, D., AND F. BONN (1995): A review of vegetation indices. *Remote Sensing Review*. 13. 95-120.

FRANKE, J. AND G. MENZ (2004): Sensor intercalibration- adjustment of MODIS-NDVI to AVHRR-NDVI data. *IEEE Conference Proceedings of the International Geoscience and Remote Sensing Symposia.* Anchorage, USA. Vol. III. 1719-1722.

KALMAN, L.S. AND G.R. PELTZER (1993): Simulation of Landsat Thematic Mapper Imagery using AVIRIS hyperspectral imagery. *Conference Proceedings of the AVIRIS Airborne Geoscience Workshop*. 97-100.

KAVZOGLU, T. (2004): Simulating Landsat ETM+ imagery using DAIS 7915 hyperspectral scanner data. *International Journal of Remote Sensing*. 20. 5049-5067.

KEREKES, J.P. AND D.A. LANDGREBE (1989): Simulation of Optical Remote Sensing Systems. *IEEE Transactions on Geoscience and Remote Sensing.* 26(6). 762-771.

MIURA, T., HUETE, A., AND H. YOSHIOKA (2006): An empirical investigation of cross-sensor relationships of NDVI and red/near-infrared reflectance using EO-1 Hyperion data. *Remote Sensing of Environment*. 100(2). 223-236.

SCHIEFER, S., HOSTERT, P. AND A. DAMM (2006): Correcting brightness gradients in hyperspectral data from urban areas. *Remote Sensing of Environment*. 101(1). 25-37.

STEVEN, M.D., MALTHUS, T.J., BARET, F., XU, H., AND M.J. CHOPPING (2003): Intercalibration of vegetation indices from different sensor systems. *Remote Sensing of Environment*. 88(4). 412-422.

TEILET, P.M., BARKER, J.L., MARKHAM, B.L., IRISH, R.R., FEDOSEJEVS, G. AND J.C. STOREY (2001): Radiometric cross-calibration of the landsat-7 ETM+ and landsat-5 TM sensors based on tandem data sets. *Remote Sensing of Environmen*. 78(1-2). 39-54.

TRISHCHENKO, A.P., CIHLAR, J., AND Z. LI (2002): Effects of spectral response function on surface reflectance and NDVI measured with moderate resolution satellite sensors. *Remote Sensing of Environment*. 81(1). 1-18.

VAN LEEUWEN, W.J.D., ORR, B.J., MARSH, S.E. AND S.M. HERRMANN (2006): Multi-sensor NDVI data continuity: Uncertainties and implications for vegetation monitoring applications. *Remote Sensing of Environment*. 100(1). 67-81.

A2. IDL-source code of the QuickBird-bands simulation program

Simulation of QuickBird's multispectral bands with hyperspectral HyMap data

```
; *Jonas Franke & Albert Moll 11/2005*
; *jonasfranke@uni-bonn.de*
;
; DO NOT SELECT A SPATIAL OR SPECTRAL SUBSET IN THE 'CHOOSE IMAGE'
; WINDOW
;
;***MAIN***
;
;declaration of variables
;HyMap band definition (information only)
;hymap_wl = fltarr(126)
;hymap_wl = [438.000, 450.000, 462.400, 478.100, 493.400, 508.500, 524.100,
;539.400, 554.900, 570.200, 585.200, 600.200, 616.300, 631.700, 646.500, 661.600,
;677.100, 692.400, 707.500, 722.900, 738.100, 753.000, 768.000, 783.100, 798.300,
;813.400, 828.500, 843.900, 859.200, 874.300, 878.200, 895.400, 911.100, 926.900,
;943.300, 959.100, 974.600, 990.400, 1006.400, 1021.700, 1037.200, 1052.700,
;1067.900, 1082.900, 1098.000, 1112.900, 1127.800, 1142.400, 1157.100,
;1171.600, 1186.000, 1200.400, 1214.800, 1229.000, 1243.100, 1257.400,
;1271.600, 1285.500, 1299.200, 1313.300, 1327.300, 1340.500, 1404.200,
;1418.800, 1433.000, 1447.100, 1460.900, 1475.200, 1489.000, 1502.600,
;1516.300, 1529.900, 1543.300, 1556.600, 1570.000, 1583.200, 1596.100,
;1609.100, 1622.200, 1635.100, 1647.800, 1660.600, 1673.200, 1685.700,
;1698.000, 1710.400, 1722.800, 1735.100, 1747.100, 1759.400, 1771.500,
;1783.400, 1795.100, 1807.000, 1951.100, 1970.300, 1989.500, 2008.500,
;2027.000, 2045.300, 2063.700, 2082.100, 2100.400, 2118.500, 2136.200,
;2153.500, 2170.800, 2187.900, 2205.800, 2224.000, 2240.800, 2258.000,
;2274.500, 2291.600, 2308.800, 2325.000, 2341.300, 2357.400, 2373.200,
;2389.200, 2405.300, 2421.500, 2437.100, 2452.600, 2467.800, 2483.000]
```

;QB band definition (center wavelengths)
QB_wl = fltarr(5)
QB_wl = [700.000,480.000,545.000,652.000,810.000]

;QB relative spectral response definition (fitted to HyMap-bands center wavelenghts)
QB_sens = fltarr(126,5)

;pan band RSR-values
QB_sens[*,0] = [0.178943, 0.216273, 0.266911, 0.345567, 0.369244, 0.417356,
0.500333, 0.615882, 0.748656, 0.861359, 0.936789, 0.970886, 0.994809, 0.980535,
0.928783, 0.886836, 0.888825, 0.889041, 0.868937, 0.871558, 0.895546, 0.923035,
0.912846, 0.881965, 0.850109, 0.861187, 0.842633, 0.842943, 0.792530, 0.749004,
0.700333, 0.645481, 0.588863, 0.502526, 0.409906, 0.317245, 0.257470, 0.209824,
0.163008, 0.122757, 0.078367, 0.037481, 0.000000, 0.000000, 0.000000, 0.000000,
0.000000, 0.000000, 0.000000, 0.000000, 0.000000, 0.000000, 0.000000, 0.000000,
0.000000, 0.000000, 0.000000, 0.000000, 0.000000, 0.000000, 0.000000, 0.000000,
0.000000, 0.000000, 0.000000, 0.000000, 0.000000, 0.000000, 0.000000, 0.000000,
0.000000, 0.000000, 0.000000, 0.000000, 0.000000, 0.000000, 0.000000, 0.000000,
0.000000, 0.000000, 0.000000, 0.000000, 0.000000, 0.000000, 0.000000, 0.000000,
0.000000, 0.000000, 0.000000, 0.000000, 0.000000, 0.000000, 0.000000, 0.000000,
0.000000, 0.000000, 0.000000, 0.000000, 0.000000, 0.000000, 0.000000, 0.000000,
0.000000, 0.000000, 0.000000, 0.000000, 0.000000, 0.000000, 0.000000, 0.000000]

;blue band RSR-values
QB_sens[*,1] = [0.216377, 0.530611, 0.757708, 0.935744, 0.969845, 0.576632,
0.168714, 0.059823, 0.019905, 0.012656, 0.010256, 0.009897, 0.007884, 0.002897,
0.002605, 0.002898, 0.009827, 0.019657, 0.007592, 0.008299, 0.002761, 0.003293,
0.003512, 0.003208, 0.003139, 0.003543, 0.004127, 0.004637, 0.005731, 0.005252,
0.005160, 0.005927, 0.009516, 0.009297, 0.004731, 0.002253, 0.001385, 0.001183,
0.001083, 0.001309, 0.001566, 0.000406, 0.000000, 0.000000, 0.000000, 0.000000,
0.000000, 0.000000, 0.000000, 0.000000, 0.000000, 0.000000, 0.000000, 0.000000,

0.000000, 0.000000, 0.000000, 0.000000, 0.000000, 0.000000, 0.000000, 0.000000,
0.000000, 0.000000, 0.000000, 0.000000, 0.000000, 0.000000, 0.000000, 0.000000,
0.000000, 0.000000, 0.000000, 0.000000, 0.000000, 0.000000, 0.000000, 0.000000,
0.000000, 0.000000, 0.000000, 0.000000, 0.000000, 0.000000, 0.000000, 0.000000,
0.000000, 0.000000, 0.000000, 0.000000, 0.000000, 0.000000, 0.000000, 0.000000,
0.000000, 0.000000, 0.000000, 0.000000, 0.000000, 0.000000, 0.000000, 0.000000,
0.000000, 0.000000, 0.000000, 0.000000, 0.000000, 0.000000, 0.000000, 0.000000,
0.000000, 0.000000, 0.000000, 0.000000, 0.000000, 0.000000, 0.000000, 0.000000,
0.000000, 0.000000, 0.000000, 0.000000, 0.000000, 0.000000, 0.000000, 0.000000]

;green band RSR-values
QB_sens[*,2] = [0.004626, 0.013833, 0.026761, 0.160995, 0.421598, 0.752954,
0.874378, 0.975975, 0.981433, 0.976526, 0.781324, 0.332658, 0.094533, 0.030157,
0.026362, 0.015515, 0.012683, 0.005689, 0.003259, 0.007146, 0.004020, 0.002606,
0.003096, 0.004055, 0.003811, 0.003095, 0.003212, 0.004403, 0.007924, 0.009122,
0.008300, 0.007566, 0.008025, 0.006690, 0.003565, 0.001726, 0.001182, 0.000925,
0.000850, 0.001118, 0.000987, 0.000287, 0.000000, 0.000000, 0.000000, 0.000000,
0.000000, 0.000000, 0.000000, 0.000000, 0.000000, 0.000000, 0.000000, 0.000000,
0.000000, 0.000000, 0.000000, 0.000000, 0.000000, 0.000000, 0.000000, 0.000000,
0.000000, 0.000000, 0.000000, 0.000000, 0.000000, 0.000000, 0.000000, 0.000000,
0.000000, 0.000000, 0.000000, 0.000000, 0.000000, 0.000000, 0.000000, 0.000000,
0.000000, 0.000000, 0.000000, 0.000000, 0.000000, 0.000000, 0.000000, 0.000000,
0.000000, 0.000000, 0.000000, 0.000000, 0.000000, 0.000000, 0.000000, 0.000000,
0.000000, 0.000000, 0.000000, 0.000000, 0.000000, 0.000000, 0.000000, 0.000000,
0.000000, 0.000000, 0.000000, 0.000000, 0.000000, 0.000000, 0.000000, 0.000000]

;red band RSR-values
QB_sens[*,3] = [0.002445, 0.002991, 0.002901, 0.002469, 0.002713, 0.003507,
0.005277, 0.006611, 0.008994, 0.014446, 0.034541, 0.092791, 0.343687, 0.783802,
0.944286, 0.996026, 0.859333, 0.367390, 0.059699, 0.020918, 0.018618, 0.007060,
0.004401, 0.005915, 0.004573, 0.002537, 0.002489, 0.002520, 0.002483, 0.002294,
0.002053, 0.002004, 0.002679, 0.001734, 0.001017, 0.000786, 0.000692, 0.000631,

0.000694, 0.000846, 0.000817, 0.000277, 0.000000, 0.000000, 0.000000, 0.000000,
0.000000, 0.000000, 0.000000, 0.000000, 0.000000, 0.000000, 0.000000, 0.000000,
0.000000, 0.000000, 0.000000, 0.000000, 0.000000, 0.000000, 0.000000, 0.000000,
0.000000, 0.000000, 0.000000, 0.000000, 0.000000, 0.000000, 0.000000, 0.000000,
0.000000, 0.000000, 0.000000, 0.000000, 0.000000, 0.000000, 0.000000, 0.000000,
0.000000, 0.000000, 0.000000, 0.000000, 0.000000, 0.000000, 0.000000, 0.000000,
0.000000, 0.000000, 0.000000, 0.000000, 0.000000, 0.000000, 0.000000, 0.000000,
0.000000, 0.000000, 0.000000, 0.000000, 0.000000, 0.000000, 0.000000, 0.000000,
0.000000, 0.000000, 0.000000, 0.000000, 0.000000, 0.000000, 0.000000, 0.000000,
0.000000, 0.000000, 0.000000, 0.000000, 0.000000, 0.000000, 0.000000, 0.000000]

;NIR band RSR-values
QB_sens[*,4] = [0.003589, 0.004741, 0.004541, 0.005346, 0.003276, 0.002659,
0.003743, 0.009325, 0.005859, 0.007307, 0.004878, 0.003657, 0.004433, 0.006184,
0.008625, 0.012140, 0.014500, 0.022586, 0.041335, 0.074445, 0.174780, 0.496183,
0.915085, 0.967438, 0.874058, 0.832026, 0.803899, 0.710577, 0.609807, 0.511680,
0.394341, 0.219116, 0.089248, 0.024957, 0.007388, 0.003615, 0.002250, 0.001860,
0.001691, 0.002069, 0.001779, 0.000667, 0.000000, 0.000000, 0.000000, 0.000000,
0.000000, 0.000000, 0.000000, 0.000000, 0.000000, 0.000000, 0.000000, 0.000000,
0.000000, 0.000000, 0.000000, 0.000000, 0.000000, 0.000000, 0.000000, 0.000000,
0.000000, 0.000000, 0.000000, 0.000000, 0.000000, 0.000000, 0.000000, 0.000000,
0.000000, 0.000000, 0.000000, 0.000000, 0.000000, 0.000000, 0.000000, 0.000000,
0.000000, 0.000000, 0.000000, 0.000000, 0.000000, 0.000000, 0.000000, 0.000000,
0.000000, 0.000000, 0.000000, 0.000000, 0.000000, 0.000000, 0.000000, 0.000000,
0.000000, 0.000000, 0.000000, 0.000000, 0.000000, 0.000000, 0.000000, 0.000000,
0.000000, 0.000000, 0.000000, 0.000000, 0.000000, 0.000000, 0.000000, 0.000000,
0.000000, 0.000000, 0.000000, 0.000000, 0.000000, 0.000000, 0.000000, 0.000000]

QB_sens[*,0] = QB_sens[*,0]/26.322581 ; devided by sum of relative spectral response of pan band
QB_sens[*,1] = QB_sens[*,1]/4.412846   ; devided by sum of relative spectral response of blue band

```
QB_sens[*,2] = QB_sens[*,2]/6.584972    ; devided by sum of relative spectral
response of green band
QB_sens[*,3] = QB_sens[*,3]/4.621948    ; devided by sum of relative spectral
response of red band
QB_sens[*,4] = QB_sens[*,4]/7.887684    ; devided by sum of relative spectral
response of NIR band
;---------------------------------------------------------------------------
;image selection

envi_select, title='Choose image', $
            fid=fid, dims=dims,pos=pos
   if (fid eq -1) then return

input_array_xsize = dims[2]-dims[1]+1
input_array_ysize = dims[4]-dims[3]+1
input_array_bands = n_elements(pos)
if (input_array_bands) ne 126 then return
;---------------------------------------------------------------------------
spec_bands_quickbird = 5;
;---------------------------------------------------------------------------
; tiling to enable processing of whole scene

tile_id=envi_init_tile(fid,pos, num_tiles=num_tiles, ys=dims[3], ye=dims[4],
interleave=1)

TLB = WIDGET_AUTO_BASE(title='Ausgabe quickbird')
P = widget_outf(TLB, uvalue='Dateiname', /auto)
result = auto_wid_mng(TLB)
if (result.accept eq 0) then begin
return
endif

openw, unit, result.Dateiname , /get_lun
```

```
im_sz_str=string(num_tiles)
envi_report_init, ['Lines to be processed:   ', $
im_sz_str], title='Status', base=zuweiser, /interupt
for tile_index=0L,num_tiles-1 do begin

   tile_data = envi_get_tile(tile_id, tile_index , ys=ys, ye=ye)
   ;-------------------------------------------------------------------------
   ;Matrix multiplication
   ;result is a 5 band QuickBird-simulated image (same image dimensions as input)
   ;equation: (pixel value (R) * relative spectral response QB)/sum of rel. spectral
   ;response QB (each band)

   output_data=QB_sens##tile_data
   writeu, unit, output_data
   envi_report_stat, zuweiser, tile_index, num_tiles-1 , CANCEL = Abbruch
   if Abbruch eq 1 then begin
     envi_report_init, base=zuweiser, /finish
     return
   endif

endfor

envi_report_init, base=zuweiser, /finish
envi_tile_done, tile_id
;-------------------------------------------------------------------------
;Ausgabe

free_lun, unit
map=envi_get_map_info(fid=fid)
envi_setup_head ,fname=result.Dateiname, ns=input_array_xsize, $
       nl=input_array_ysize, nb=spec_bands_quickbird $
      ,data_type=4, interleave=1, map_info=map, /write ;

end
```